Properties of III-Nitride-Based Polariton and Spin Polariton Diode Lasers

by

Aniruddha Bhattacharya

A dissertation submitted in partial fulfillment
of the requirements for the degree of
Doctor of Philosophy
(Electrical Engineering)
in the University of Michigan
2018

Doctoral Committee:

Professor Pallab K. Bhattacharya, Chair
Assistant Professor Parag B. Deotare
Professor Zetian Mi
Professor Jamie D. Phillips
Associate Professor Vanessa Sih

Aniruddha Bhattacharya

anirudb@umich.edu

ORCID iD: 0000-0002-7727-0514

ACKNOWLEDGEMENTS

I would like to thank my dissertation supervisor, Professor Pallab Bhattacharya for providing me an opportunity to work in his research group. I would like to thank my advisor and the other members of the dissertation committee, Professor Parag B. Deotare, Professor Zetian Mi, Professor Jamie D. Phillips, and Professor Vanessa Sih, for their careful consideration of the present dissertation and for all the recommendations made. I would also like to thank my fellow research group members, Dr. Thomas Frost, Prof. Zunaid Baten, Dr. Arnab Hazari, Anthony Aiello and Ayush Pandey, with whom I have collaborated during my graduate research career. Thomas and Zunaid epitaxially grew and processed, respectively, the samples described in this dissertation. Theoretical work done by our collaborators, Professor Alexey Kavokin and Drs. Ivan Iorsh and Evgeny Sedov are also gratefully acknowledged. I am also very grateful for the extremely high quality of the teaching, which I have benefitted from, in the all of the classes I have taken in the Departments of Physics, and Electrical Engineering and Computer Science, at the University of Michigan. Professors Pallab Bhattacharya and Duncan Steel were particularly inspiring.

I am grateful for all the help provided by Brian Armstrong, Nadine Wang, Matthew Oonk, and Sandrine Martin from the Robert H. Lurie Nanofabrication Facility (LNF). I would also like to thank Lisa Vogel, Jennifer Miskell, Elissa Trumbull, Deb Swartz, Karen Liska, Anne Rhodes, Steven Pejuan, Kristen Thornton, and Jose-Antonio

Rubio, for their excellent administrative support throughout my graduate school career. I would also like to thank the Materials Research Science and Engineering Centers (MRSEC) program of the National Science Foundation (NSF), the Horace H. Rackham School of Graduate Studies of the University of Michigan, and the Department of Electrical Engineering and Computer Science (EECS) of the University of Michigan for funding my research and my graduate studies. This work would not have been possible without their support. Finally, I would like to thank my friends and family for all of their support.

TABLE OF CONTENTS

CHAPTER

VI. Spin-Injection-Induced Gain Anisotropy in a Polariton Diode Laser……………………………………..………………….…………….....105

VII. Non-Linear Photocurrent Response to Bosonic Final State Stimulation in Microcavity Diodes ……………………………………………………..119

LIST OF FIGURES

Figure

ABSTRACT

The cavity electrodynamic regime of strong coupling of emitter-photon interactions in a semiconductor microcavity gives rise to new light-matter entangled quasiparticles, also known as exciton-polaritons. The non-linear nature of the energy-momentum dispersions of these composite bosons has been suitably engineered and efficiently utilized to demonstrate inversionless coherent emission, or polariton lasing in submicron-scale optical cavities. Previous theoretical as well as experimental work on Gallium Arsenide and Cadmium Telluride-based systems operated at cryogenic temperatures, have shown the central importance of the nature of the output polarization of the emitted light originating from the radiative decomposition of these polaritons. Room-temperature operation of these lasers necessitates the use of wide-band gap semiconductors such as Gallium Nitride, because of their large free excitonic binding energies and oscillator strengths, which consequently lead to stronger and more robust exciton-photon strong coupling. Thus, the steady state output polarization characteristics of Gallium Nitride-based microcavity polariton lasers operated with unpolarized electrical injection, have been examined at room temperature. The output is essentially unpolarized below the nonlinear threshold injection current and is linearly polarized above it with a maximum degree of polarization of ∼ 22%.

Besides other advantages, a spin-polarized laser offers inherent control of the output circular polarization. Electrical spin injection in a bulk Gallium Nitride-based microcavity polariton diode laser enables the realization of an electrically modulated low-energy circularly-polarized coherent light source. Successful electrical spin injection in bulk Gallium Nitride, which is the active layer of the polariton diode laser, has been independently confirmed from room-temperature four-terminal Hanlè spin precession measurements made on Gallium Nitride-based spin valves, and observation of hysteretic circular polarization in III-nitride-based light-emitting diodes. The optical selection rules governing the operation of the latter have also been elucidated. Electrical injection of spin polarized electrons is accomplished in all the above-mentioned devices via a n-type Cobalt Iron alloy/Magnesium Oxide spin injector contact. The output polarization characteristics of this polariton diode laser have been examined at room temperature. A degree of output circular (linear) polarization of ~ 25 (33) % is recorded under remanent magnetization. The helicity as well as the degree of the steady-state circular polarization is deterministically governed by the magnetizing field used to magnetize the ferromagnetic contacts. The variation of output circular and linear polarization with spin-polarized injection current has been analyzed employing two distinct spin-dependent rate equation models, and there is good agreement between measured and calculated data in both cases.

The present work also theoretically explores other optoelectronic properties of these spin polariton lasers. Optical effects arising from spin-induced gain anisotropy such as threshold reduction and emission intensity enhancement have been theoretically predicted for these diode lasers. An electrical excitation mechanism has also been formulated, which can potentially magnify the degree of a deterministic circular polarization of the output emission by an order of magnitude, compared to the injected electron spin polarization. The dissertation concludes with the discussion of the observation of a non-linear enhancement in the excitation-dependent photocurrent characteristics of the microcavity diodes with a threshold, which is consistent with the polariton lasing threshold. This is explained in the framework of an Auger-like process of excitonic dissociation into its constituent electron-hole pairs, which can be stimulated by the occupation of the polariton lasing states and the observed effect is therefore a unique manifestation of the bosonic final-state stimulation effect in polariton lasers.

Chapter I

Introduction

1.1 Strong Coupling and Polariton Lasing

One of the central driving forces in research on semiconductor lasers, has been the design and implementation of highly energy-efficient light-emitting devices, which can generate coherent output at rather modest values of injected current densities. The threshold current density is probably the single most important figure of merit of a laser, both from a fundamental physical as well as a technological perspective. The threshold current density heralds the onset of a highly nonlinear and essentially discontinuous second-order phase transition, whence the light output transitions from an essentially incoherent to a coherent nature. The coherent nature is reflected in the spectral, spatial as well as the temporal characteristics of the output emission. Threshold in a conventional semiconductor cavity mode-mediated photon laser is accomplished when the nonlinear optical gain, originating from net stimulated emission, overwhelms the resonator losses, such as the cavity losses and losses due to leakage from the mirror facets.

With regards to conventional semiconductor laser diodes, the last 60 years have witnessed a dramatic reduction in the threshold current densities from several tens of kA/cm^2 pulsed injection to several tens of A/cm^2 of continuous-wave drive in GaAs-based devices. Similar trends have also been observed in materials systems, such as CdTe-based, InP-based and III-nitride-based systems. This has been brought about by a complex interplay of progress towards lower-dimensional quantum confined heterostructures and miniaturization of the device active regions. The submicron-scale dimensions of the cavities mean new non-classical phenomena can now be clearly observed and studied. For example, the increase in the spontaneous emission rate in a cavity (the Purcell effect) and a large spontaneous emission coupling to the lasing mode (β-factor ~ > 0.1) are regularly observed in these short cavity length devices [1]. These effects have a predominant effect on the output emission and performance characteristics of these lasers. In contrast, there is an even more exciting cavity electrodynamic regime also known as the strong-coupling regime, wherein the elementary excitations of the system themselves complete change their character from being uncoupled cavity photons and semiconductor excitons to being light-matter admixed quasiparticles also known as semiconductor microcavity excitons-polaritons [2]. This regime, as discussed below, can be efficiently harnessed to generate inversionless low-threshold coherent emission also known as polariton lasing.

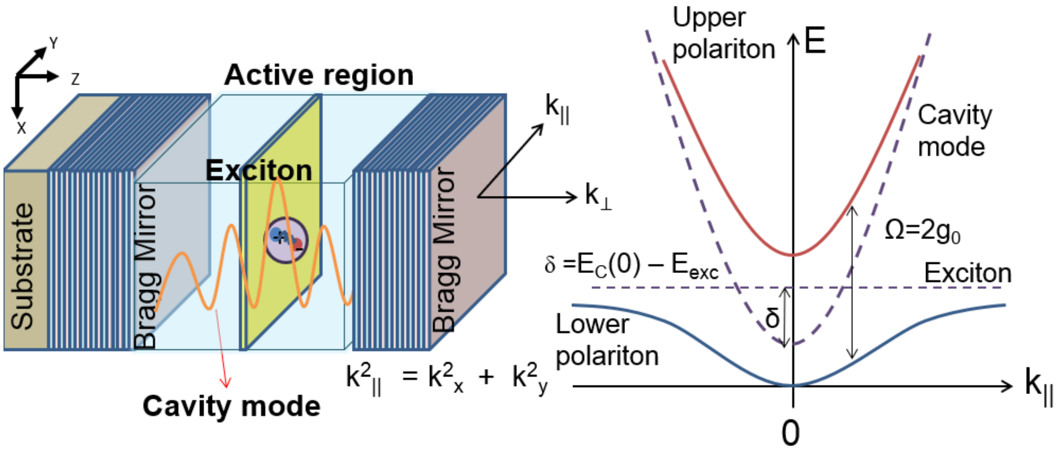

(a) (b)

Figure 1.1 (a) Schematic representation of the microcavity showing the uncoupled cavity photon and excitonic resonances, (b) dispersion relations for the polaritons in a strongly coupled microcavity and those of the bare photon and exciton from which the polaritons are derived. (Courtesy of Professor Pallab Bhattacharya, Invited Talk entitled "Strong Coupling Phenomena, Polariton Lasers and Room Temperature Bose-Einstein Condensation" at UC Davis, December 3, 2013)

When an emitter, for example a free exciton, is placed in a resonant cavity as shown in Fig. 1.1, then in the strong coupling regime there is a coherent, reversible and periodic exchange of energy between the emitter and the cavity in the form of Rabi oscillations with a frequency larger than both the emitter and cavity photon decay rate. Cavity mode and exciton can strongly couple when they have similar values of energies at the same value of the in-plane wave vector $k_{||}$. Under conditions of strong coupling, a strong collective dipole-dipole interaction between the intra-cavity photon field and the polarization field of the free exciton lifts the cavity photon-exciton degeneracy and gives rise to two light-matter entangled energy eigenstates, called exciton-polaritons, separated by a characteristic Ω_{VRS} (the so-called "Vacuum Rabi splitting energy") or exchange energy. This was first experimentally observed in 1992 in a GaAs-based microcavity as shown in Fig. 1.2 [3]. Upon suitable excitation (electrical or optical), exciton-polaritons are created which undergo polariton-phonon, polariton-electron and polariton-polariton scattering. The polaritons become more photon-like, as they scatter downhill the dispersion curve, and some are lost from the system by leakage of their photonic components. Eventually, a degenerate and macroscopic coherent population of polaritons quickly builds up at $k_{||} \sim 0$ by stimulated polariton-polariton scattering, which is a phase coherent process and is the relevant gain mechanism in this coherent light source [4, 5]. Polariton-polariton scattering is stimulated to $k_{||} \sim 0$ states, when the polariton occupation per mode centered at $k_{||} \sim 0$ exceeds unity. A simplified picture of these processes is shown in Fig. 1.3. The coherent polariton condensate (state) generates coherent light by spontaneous radiative recombination. This inversionless process of coherent emission is termed polariton lasing. Thus, for coherent polariton emission, a macroscopically populated quantum state of exciton polaritons must be created at the bottom of the lower-polariton branch ($k_{||} \sim 0$). This single quantum mode is sometimes referred to as a highly non-equilibrium polariton condensate and its formation is generally kinetically rather being thermodynamically driven [6, 7].

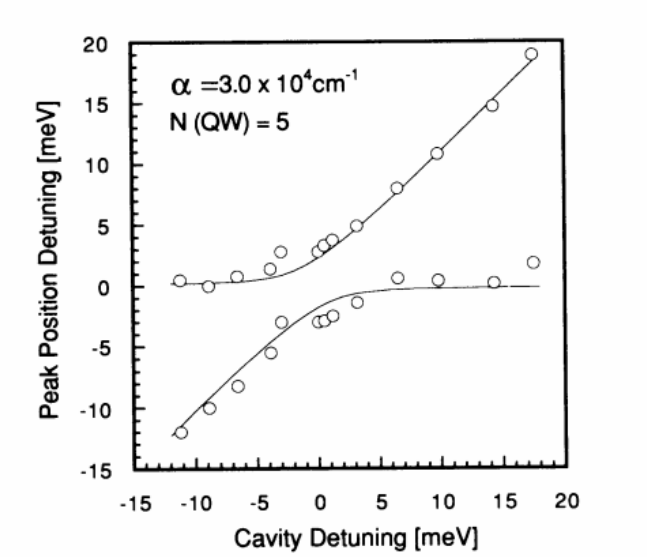

Figure 1.2 The first experimental demonstration of strong coupling in a solid-state system. The data points show the reflectivity peak positions as a function of cavity detuning for a five-quantum-well sample at T=5 K. The theoretical fit is obtained through a standard multiple-interference analysis of the DBR-Fabry-Perot-quantum-well structure. (Weisbuch et. al., Phys. Rev. Lett. **69**, 3314 (1992))

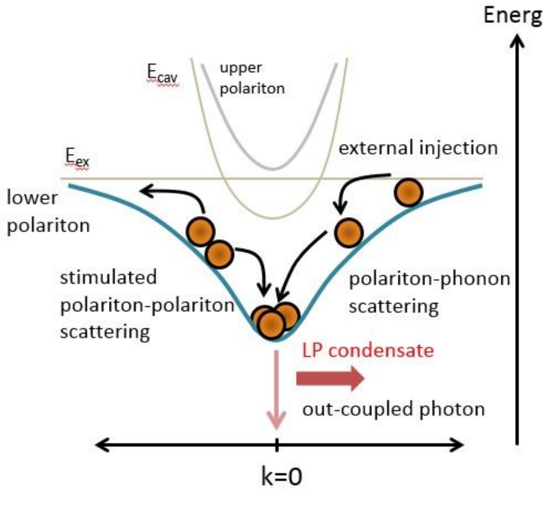

Figure 1.3 Schematic representation of the various fundamental underlying processes involved in the process of polariton lasing. (Courtesy of Professor Pallab Bhattacharya, Invited Talk entitled “Strong Coupling Phenomena, Polariton Lasers and Room Temperature Bose-Einstein Condensation” at UC Davis, December 3, 2013)

1.2 A Historical Overview of Polariton Lasers

Ataç İmamoğlu in 1996 first theoretically conceived of a scheme for accomplishing inversionless coherent emission in a solid-state system by efficiency utilizing non-equilibrium condensation effects involving composite bosons. He first thought of bare free excitons as viable candidates for condensation. A so-called exciton boser or laser, i.e., a device that generates a coherent population of non-equilibrium excitons was proposed [8]. A semiconductor microcavity exciton-polariton laser, operating on similar principles, was proposed by İmamoğlu and co-workers later in the same year [9]. The latter was considered to be a more suitable platform for condensation because of the lower effective masses of polaritons as compared to those of excitons by virtue of the former's photonic component. The polariton laser was conceptualized based on the then already known and experimentally demonstrated concepts of true thermodynamic phase transitions such as Bose-Einstein condensation. The former's highly non-equilibrium character, more akin to photon lasers, is contrasted to the equilibrium nature of conventional BECs in Fig. 1.4.

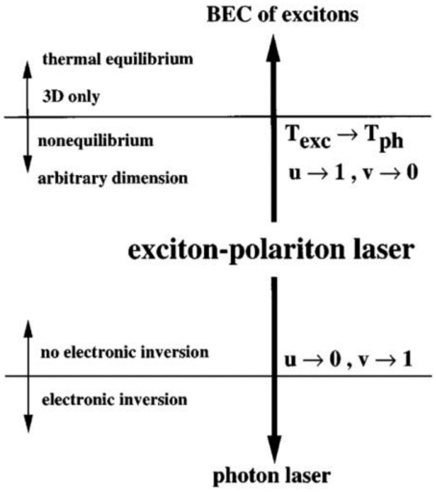

Figure 1.4. The first theoretical conceptualization of the polariton laser. The diagram compares the exciton polariton laser to the more familiar concepts of Bose-Einstein condensate of excitons and photon lasers. u and v determine the exciton and photon character of the polariton, respectively. (İmamoğlu et. al., Phys. Rev. A **53**, 4250 (1996))

The first widely accepted experimental demonstration of a polariton laser was accomplished by L. S. Dang and co-workers at the Université J. Fourier in Grenoble, France in 1998 [10]. Nonlinear polariton emission was observed in a multiple CdTe/Cd$_{0.80}$Mn$_{0.20}$Te quantum-well-based microcavity at 4.2 K, as shown in Fig. 1.5. This was followed by multiple reports of polariton lasing in GaAs-based systems at cryogenic temperatures, at the beginning of the new millennium from around the group by multiple research groups based at the United States [4, 5], England [11] and France [12]. The next major advancement was the demonstration of room temperature polariton lasing in a bulk GaN-based microcavity [13]. A low-threshold (~ 1 mW of incident pump power) coherent emission, 1 order of magnitude smaller than in previously reported nitride-based VCSELs, was observed under pulsed nonresonant excitation.

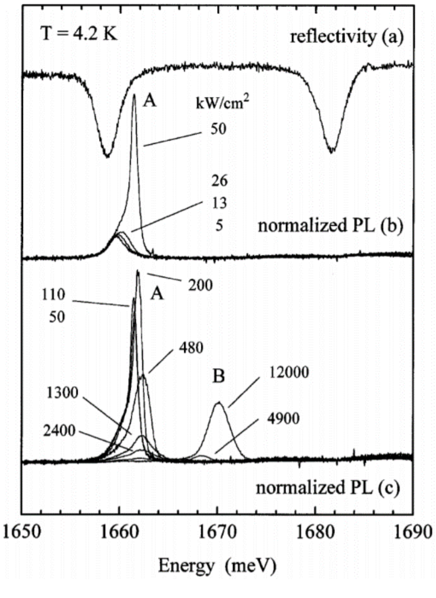

Figure 1.5. The first demonstration of the polariton laser, from optical measurements made at 4.2 K and for zero detuning. (a) Reflectivity spectrum showing the lower and upper polaritons. (b) PL spectra for a range of excitation densities. The excitation is at 1.8 eV. All spectra are normalized to the corresponding excitation densities. The A line is stimulated PL associated with the lower polariton state in the strong exciton-photon coupling regime. (c) Same as in (b). The B line corresponds to the stimulated emission of electron-hole plasma in the weak coupling regime. (Le Si Dang et. al., Phys. Rev. Lett. **81**, 3920 (1998))

The next major milestone was the demonstration of electrical injection in a polariton laser and was accomplished independently by two research groups spearheaded by Pallab Bhattacharya at the University of Michigan at Ann Arbor [14] and Sven Höfling at the Universität Würzburg in Germany [15]. Both research groups observed coherent emission from a surface-emitting GaAs-based microcavity after applying a strong magnetic field (~ 5 - 7 T) in the Faraday geometry. The demonstration of electrically pumped polariton lasing was certainly transformative and is widely considered a milestone in optoelectronics. In particular, the University of Michigan group achieved this result by a judicious symbiosis of modulation doping of the wells, to accelerate the polariton-electron scattering, and an applied magnetic field in the Faraday geometry to increase the exciton-polariton saturation density. These measures helped to accomplish lasing in a GaAs-based system, which was notorious for its problems with thermalization and relaxation of the injected polaritons. The experiments were performed at 30 K with an applied field of 7 T.

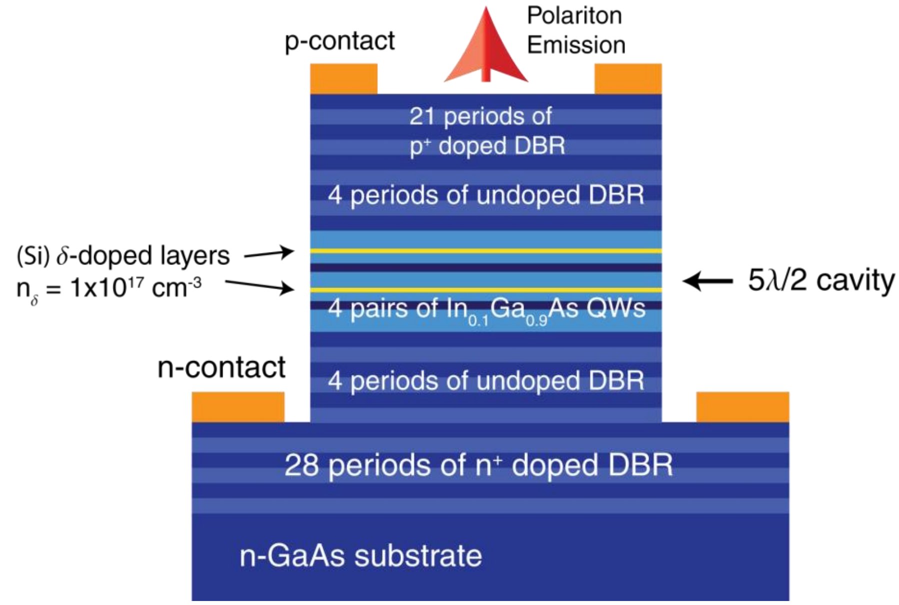

Figure 1.6. The first demonstration of an electrically injected polariton laser. Schematic of the *p*-*i*-*n* multiquantum well (MQW) modulation doped microcavity diode used to achieve lasing. (Bhattacharya et. al., Phys. Rev. Lett. **110**, 206403 (2013))

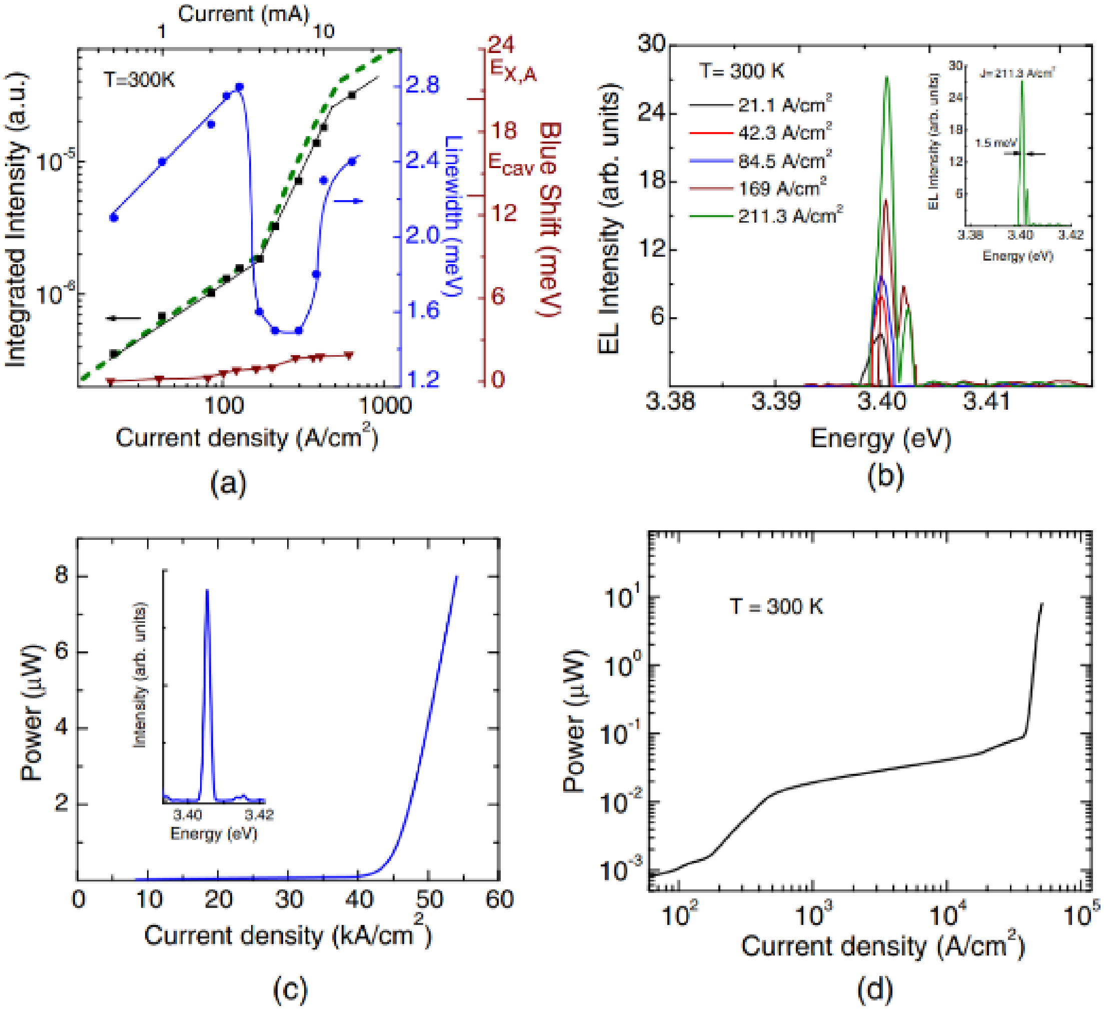

Figure 1.7. The first demonstration of a room temperature electrically injected polariton laser showing polariton and photon lasing characteristics at normal detection angle. (a) Integrated EL intensity, LP emission linewidth, and blueshift of peak emission as a function of injected current density, (b) EL spectra measured at various injection levels. Inset shows the spectra above threshold (5 mA), (c) light-current characteristics of photon lasing observed in the same device at higher injection levels. Inset shows EL spectra measured above photon lasing threshold (1.04 A), (d) two threshold lasing behavior with the nonlinearities due to polariton and photon lasing. (Bhattacharya et. al., Phys. Rev. Lett. **112**, 236802 (2014); Featured in *Physics* and selected as Editors' Suggestion)

Real world practical use of polariton lasers as solid-state optoelectronic devices, which can potentially compete with and even displace conventional semiconductor laser diodes, necessitates room temperature operation with electrical injection. The next major progress was made again at the University of Michigan, where Bhattacharya and co-workers demonstrated a room-temperature GaN-based electrically injected polariton laser [16]. The breakthrough was achieved by replacing the surface-emitting geometry, which had been a defining feature of semiconductor microcavities wherein strong coupling was observed, by the edge-emitting geometry characteristic of in-plane Fabry-Pèrot lasers. The nonlinear threshold for polariton lasing was ~ 169 A/cm^2 in the light-current characteristics, accompanied by a collapse of the emission linewidth to a mere 1 meV, and small blueshift of the emission peak (~ 2 meV). Measurements of angle-resolved luminescence, polariton condensation and occupation in momentum space, and output spatial coherence and outputpolarization also supported the observations of polariton lasing. Most importantly, a second threshold, due to conventional photon lasing, was observed at an injection of ~ 44 kA/cm^2 in the same diode (Fig. 1.7 (d)), unambiguously confirming the different nature of origin of the lower threshold as being due to polariton lasing in the strong coupling regime.

1.3 Nature of Output Polarization of Polariton Lasers: Motivation for the Present Work

The main goal of the work presented in this dissertation was the successful demonstration of an electrically injected spin-polarized coherent light source emitting in the ultra-violet region of the spectrum based on the strong-coupling effect in semiconductor microcavities. The output of a microcavity coherent light source is usually linearly polarized in the emitter-cavity photon strong coupling regime. Linear polarization can be observed in the steady state output above the polariton lasing threshold only by pinning along a preferred crystallographic axis. This has been observed in polariton lasers both pumped electrically [17] (Fig. 1.8) and optically [18] (Fig. 1.9). Further, both electrically pumped and optically excited circularly polarized polariton lasers have been demonstrated. For example, the steady-state output circular polarization, observed in GaAs-based electrically injected polariton lasers operated with a high magnetic field in the Faraday geometry, originates from the Zeeman splitting induced by the magnetic field and subsequent LP condensation in the less energetic of the two circularly- polarized LP ground states [14].

On the other hand, it is possible to obtain a controlled and variable circularly polarized output by electrically injecting spin polarized carriers with a suitable ferromagnetic contact or a diluted magnetic semiconductor acting as a spin injector, as demonstrated with conventional photon lasers designed as vertical cavity surface-emitting lasers [19] and light-emitting diodes [20]. This has not yet been demonstrated in polariton lasers operated with electrical spin injection, which motivated the present work. However, since the present dissertation is mainly concerned with GaN-based polariton lasers, the feasibility of electron spin injection and transport has to be first examined in n-type bulk GaN. Bulk n-type GaN functions both as the n-type contact as well as the active layer of the polariton devices.

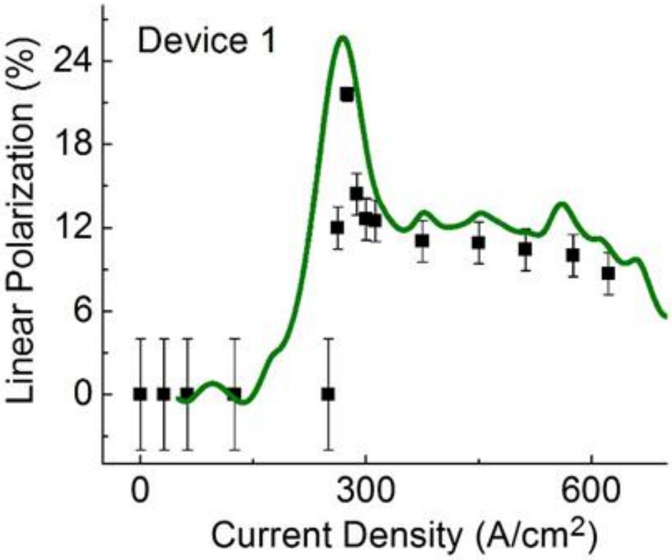

Figure 1.8. Measured degree of linear polarization as a function of the injected current density for a GaN-based polariton diode laser. The solid line shows a theoretical analysis of the measured data.

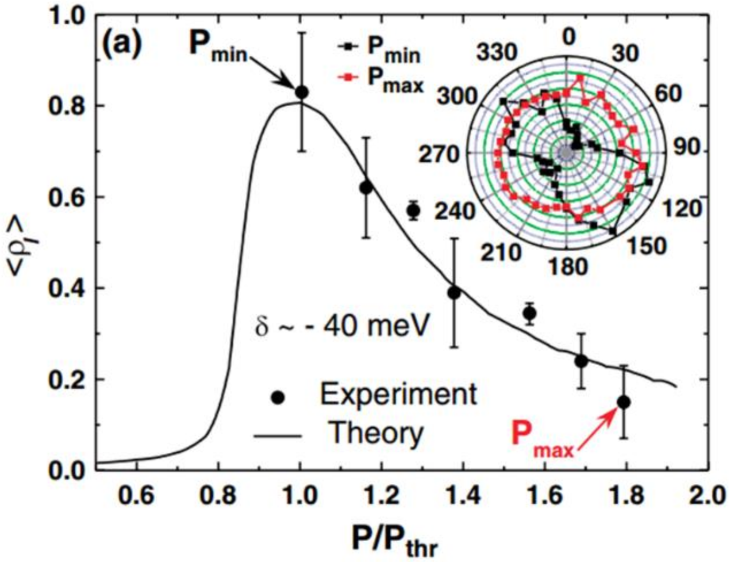

Figure 1.9. Experimental pump power dependence of the linear polarization degree above threshold (black dots) and corresponding theoretical calculation (black line) for an optically triggered GaN polariton laser. Inset: Polar intensity plot showing polarization pinning at P_{min} = P_{thr} and depinning of polarization above threshold at P_{max}. (Levrat et. al., Phys. Rev. Lett. **104**, 166402)

1.4 GaN-Based Spintronics and its Applications

The III-nitride family of wide bandgap semiconductors, such as GaN and their alloys (InGaN, AlGaN, InAlN), are important for diverse applications ranging from solid-state lighting, ultra-violet and deep ultra-violet coherent light sources and photodetectors and high-power, high-voltage and high-frequency electronics [21, 22]. GaN is also suitable for room temperature spintronic applications owing to its intrinsically weak spin-orbit coupling (SOC) [23-25]. Figure 1.10 shows the band structure of bulk GaN near the Γ point. The SOC parameter, which is roughly the average of the valence band splittings, for GaN is ~ 20 meV. This is rather small compared to the same value for GaAs, where it is ~ 341 meV. Thus, apparently GaN should be better suited than, for example GaAs, for spintronics, because smaller values of SOC should lead to smaller D'yakonov-Perel (DP) spin scattering rates. Values of electron spin relaxation lifetimes in bulk n-doped wurtzite GaN, ranging from 35 to 50 ps, have been reported from room temperature time-resolved Kerr-rotation and time-resolved Faraday rotation spectroscopy measurements [25, 26]. Spin diffusion parameters in relatively defect-free single wurtzite GaN nanowires (NWs) have also been determined from four-terminal Hanle spin precession measurements [27], which yielded a maximum spin lifetime ~ 100 ps and a spin diffusion length of ~ 260 nm at room temperature for samples having an unintentional background n-type doping concentration of ~ 1×10^{17} cm^{-3}. Works on GaN-based spin-optronic devices are relatively scarce. Chapter IV of this dissertation will examine bulk GaN-based spintronic devices, such as non-local spin valves, spin-polarized light-emitting diodes and spin polariton lasers. From the four-terminal non-local measurements made on bulk n-type GaN, as discussed in Chapter IV, an electron spin relaxation length of ~ 176 nm, and an electron spin injection efficiency of ~ 8 % at the interface of the spin contact and GaN contact layer, are obtained. These rather low values are at least partially due to relatively large densities of defects and dislocations in GaN grown on lattice-mismatched substrates such as sapphire. The CoFe/MgO ferromagnetic tunnel contact has been adopted as the solid-state electron spin injector in the spintronic devices, since it has shown the highest electron spin injection efficiencies at room temperature in other III-V semiconductors such as GaAs [28]. The observation of spin precession signals and successful transduction of spin angular momentum to output circular polarization in spin-LEDs, shows that electron spin injection in polariton laser diodes is possible.

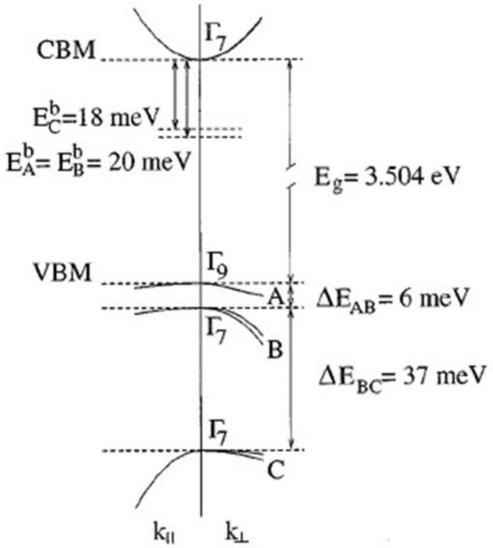

Figure 1.10 A relatively simple representation of the band structure of wurtzite GaN near the Γ point. The numerical values are obtained from measurements at cryogenic temperatures. (G. D. Chen, et al. Appl. Phys. Lett. **68**, 2784 (1996))

1.5 Spin-Polarized Coherent Light Sources

The ability to modulate the output polarization state of lasers to switch between mutually orthogonal polarization states [29] would be useful for a host of applications including coherent detection systems, optical communications with enhanced bandwidth, secure communication and cryptography, optical switching and study of biochemically active chiro-optical molecules, which include certain proteins and vitamins. The output polarization of semiconductor lasers is mainly determined by the polarization properties of the active (gain) region and optical cavity (mirrors). Vertical cavity surface emitting lasers (VCSELs), in general, have been known to have very poor polarization selectivity, stability and control. Polarization control in lasers may be obtained with injection and recombination of spin polarized carriers and the output polarization is related to the spin polarization of carriers in accordance with the relevant selection rules for the conservation of the total angular momentum in the gain medium [30].

Radiative recombination of spin-up and spin-down electrons yields two coherently-coupled lasing modes, producing left and right-circularly polarized light, respectively. The axis of quantization along which the relevant components of the total angular momenta are measured is usually coincident with the direction of cavity emission. In a conventional non-magnetic laser, these two modes are pumped equally, producing two equal and in-phase circularly polarized modes which coherently superimpose to form linearly polarized light. For 100% spin polarization of the injection current, a pure circularly polarized output is theoretically estimated, while for spin injection less than 100 %, the circularly polarized light is superimposed on the linearly polarized output giving rise to elliptically polarized coherent radiation. Because of spin-induced gain anisotropy in the device active region, the overall laser threshold, which corresponds to the threshold of the preferred polarization mode, should also reduce by a factor of 2.

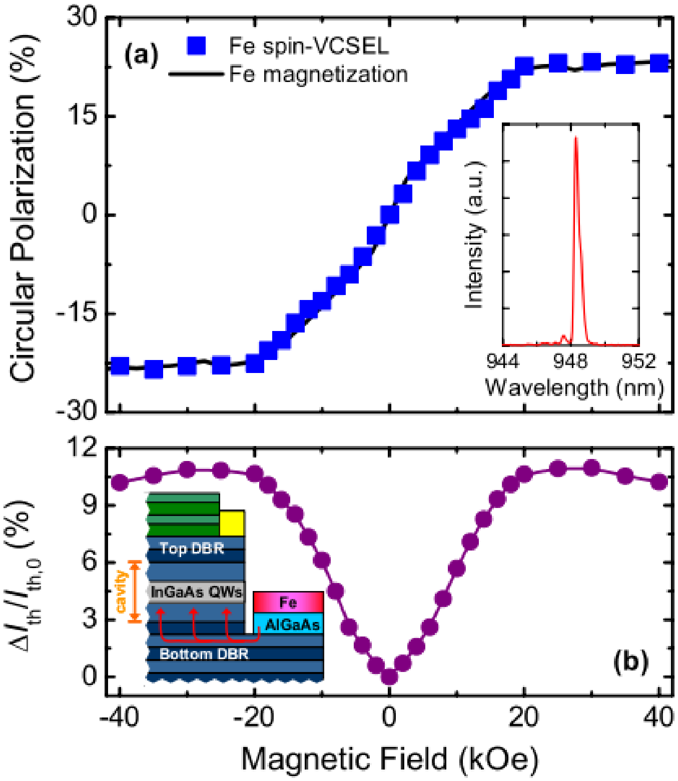

Figure 1.11 (a) Degree of circular polarization and (b) threshold current reduction versus magnetic field for a 15 μm diameter spin-polarized VCSEL measured at 50 K. The normalized out-of-plane magnetization curve for a 10 nm Fe layer is shown for comparison. Top inset shows the electroluminescence spectrum, exhibiting a full-width at half maximum of 0.36 nm at 50 K. Bottom inset depicts the Fe spin-polarized VCSEL design. (Holub et al., Phys. Rev. Lett. **98**, 146603 (2007))

The first demonstration of an optically pumped spin-polarized vertical-cavity surface-emitting-laser (spin-VCSEL) was made by Rudolph et al. [31]. The laser active region consisted of pseudomorphic InGaAs/GaAs quantum wells. The devices were operated at 6 K and both polarized light output and threshold reduction were demonstrated. Subsequently, an optically triggered room temperature spin-VCSEL with GaAs/AlGaAs quantum wells has also been demonstrated [32]. The first electrically injected spin-VCSEL, with InGaAs/GaAs quantum well gain medium, was demonstrated recently by Holub et al. [19]. The lasers were operated at 50 K and a maximum threshold current reduction of 11% and output degree of circular polarization of 23% were observed, as shown in Fig. 1.11. Spin injection of electrons were accomplished with a Fe/AlGaAs Schottky tunnel diode. In electrically pumped spin polarized light sources, a non-equilibrium spin population is injected from a magnetic contact to the forward biased active region of a diode consisting of non-magnetic semiconductors. High temperature operation of InAs/GaAs self-organized QD VCSELs have been shown up to a temperature of 230 K [33]. Previous demonstrations of optically and electrically excited spin lasers have remained limited to GaAs-based systems. Polariton lasers operated with optical spin injection (circularly polarized pump) have also been demonstrated at cryogenic temperatures [5]. As shown in Fig. 1.12, there is a non-linear increase in the output circular polarization above threshold. This dissertation reports the first example of polariton laser operation with electrical spin injection.

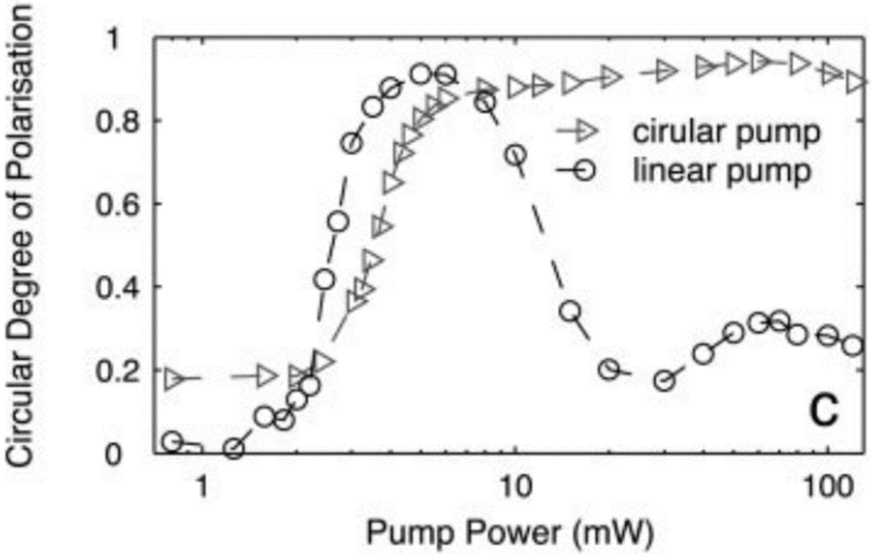

Figure 1.12. Excitation dependence of the output circular polarization of an optically triggered GaAs-based polariton laser. Data correspond to independent measurements made with linear as well as circular pump (H. Deng et al. Proc. Natl. Acad. Sci. **100**, 15318 (2003))

The present dissertation discusses the demonstration of room temperature operation of spin-polarized coherent light sources in the form of spin polariton diode lasers. These polariton lasers also have an edge-emitting geometry and thus do not require the presence of an ambient magnetic field.

1.6 Overview of the Dissertation

The present dissertation is concerned with the elucidation of the output optoelectronic and spin-optronic characteristics of GaN-based microcavity polariton laser diodes operated with and without spin-polarized electrical injection. A microcavity polariton laser diode designed in the form of a conventional in-plane Fabry-Perot semiconductor laser diode, enables room-temperature operation of electrically injected GaN-based double heterostructures. This is because of the feasibility of efficient current injection orthogonal to the axis of cavity resonance, thus enabling a relatively low series resistance pathway for the injected electrons. A spin polariton laser diode, driven by spin-polarized electrical excitation, emits controlled circularly polarized light. The value and direction of magnetizing field used to magnetize the contacts prior to operation, directly control the helicity and magnitude of the degree of circular polarization of the emitted light, above the laser threshold. It also have been theoretically shown how this value of the degree of the circular polarization can be made almost unity, with the present device configuration. However, successful operation of these spintronic polariton lasers is contingent on successful injection of spin-polarized electrons. Thus, the present dissertation also contains work on the study of spin injectors directly deposited on bulk n-type GaN, which acts as the cathode-type contact layer of the device heterostructures. Successful electrical spin injection in bulk GaN, which is also the active layer of the polariton diode laser, has been independently confirmed from room-temperature four-terminal Hanlè spin precession measurements made on GaN-based spin valves, and observation of hysteretic circular polarization in edge-emitting III-nitride light-emitting diodes. All experiments reported in this thesis have been carried out at room temperature.

The first two chapters of the dissertation introduces the basic concepts of strong coupling and polariton lasing characteristics in semiconductors, in general, with special emphasis on the nature of the output polarization characteristics of these lasers. The nature of polariton lasing and its salient differences from conventional photon lasing is also discussed. Chapter III concentrates on an experimental and theoretical analysis of the steady-state output linear polarization characteristics of GaN-based polariton lasers operated with conventional electrical injection. Measurements of sub-threshold angle-resolved electroluminescence spectra have been carried out to ascertain the strong-coupling regime of operation of these devices. Polariton lasing has been verified from measurements of output-light characteristics, zero-angle spectral characteristics and from the redistribution of the polaritons in the momentum ($k_{||}$) space, as a function of injection. The steady state output polarization characteristics of GaN-based microcavity polariton lasers operated with electrical injection at room temperature, was also reported. The output is essentially unpolarized below the non-linear threshold injection current and is linearly polarized above it with a maximum degree of polarization of ~ 22 %. The results have been analyzed theoretically and the calculated results are in agreement with the measured data. The linear polarization resolved output light-current characteristics have also been measured, wherein a distinct lowering of the non-linear threshold is observed in one device. This is interpreted in terms of spatially inhomogeneous lifting of degeneracy and polarization splitting in the microcavity.

Chapter IV studies the feasibility of electron spin injection in bulk n-type GaN. Measurements of electron spin injection, coherent transport and detection were made at room temperature by purely non-local electrical measurements. The measurements of diffusive electronic spin transport characteristics in epitaxial bulk wurtzite GaN lateral spin valve at room temperature, are reported at room temperature. Hanlè spin precession and non-local spin accumulation (magnetoresistance) measurements have also been performed with the spin valves fabricated with FeCo/MgO spin contacts. Electron spin relaxation length and spin-flip lifetime of 176 nm and 37 ps, respectively, are derived from analysis of results obtained from four-terminal Hanle spin precession measurements at 300 K. To further ascertain the feasibility of transduction of injected electron spin polarization to output circular polarization, a spin-polarized light-emitting diode was designed and processed. Room temperature circularly polarized electroluminescence is observed from these bulk GaN-based double-heterostructure edge-emitting light emitting diodes operated with continuous-wave spin-polarized electrical injection. After the discussion of the above-mentioned demonstration of appreciable spintronic and spin-optronic effects in GaN, the following chapter then details the study of the room-temperature operation of a spin polariton diode laser. The focus of chapter V is the demonstration of the room temperature operation of a spin-polarized polariton laser diode. The principal advantage of a spin-polarized laser, over conventional lasers, is that the former offers inherent control of the output circular polarization. Thus, the output polarization characteristics of a bulk GaN-based microcavity polariton diode laser were investigated at room temperature with electrical injection of spin polarized electrons via a FeCo/MgO spin injector. Polariton laser operation with a spin polarized current is characterized by a threshold of ~ 69 A/cm^2 in the light-current characteristics, a significant reduction of the electroluminescence linewidth and blueshift of the emission peak. A degree of output circular polarization of ~ 25 % is recorded under remanent magnetization. A second threshold, due to conventional photon lasing, is observed at an injection of ~ 7.2 kA/cm^2. The variation of output circular and linear polarization with spin-polarized injection current has been analyzed with the carrier and exciton rate equations and the Gross-Pitaevskii equations for the condensate and there is good agreement between measured and calculated data.

Chapter VI details further theoretical analysis of the spin polariton diode laser discussed in the previous chapter. Optical effects arising from spin-induced gain anisotropy such as threshold reduction and emission intensity enhancement, hitherto unobserved in electrically injected polariton lasers, are theoretically predicted for a bulk GaN-based exciton-polariton diode laser operated with electrical injection of spin-polarized electrons. These phenomena are deduced from a simplified spin-dependent rate equation model. An electrical excitation scheme, which can amplify the degree of a deterministic circular polarization of the output emission by an order of magnitude, compared to the injected electron spin polarization, above threshold, is also discussed. The spin-dependent rate equation model discussed in the present chapter, is different from that presented in the previous chapter. In this chapter, directly the absolute occupation numbers or particle concentrations have been used in the equations rather than employing the coupled stochastic differential equations of the previous chapter. An advantage of the same is the fact that no additive white Gaussian noise term has to be explicitly added to the equations, resulting in a smooth evolution of the calculated polariton occupation numbers with injection. This enables the observation of any small changes in the polariton laser thresholds with differences in the injected electron spin polarization, which could have been potentially masked if the theoretical approach of the previous chapter, had been employed.

Chapter VII reports on the optical excitation-dependent output photocurrent characteristics of GaN-based polariton diode lasers operated under reverse-bias at room temperature. The photocurrent demonstrates a non-linear enhancement at an incident optical power of ~ 1.6 mW, which is approximately equivalent to the value of polariton lasing threshold observed when the diodes are operated under forward bias conditions. This is explained in the framework of an Auger-like (non-radiative) process of excitonic dissociation into its constituent electron-hole pairs, which can be stimulated by the occupation of the polariton lasing states and the observed effect is therefore a unique manifestation of the bosonic final state stimulation in polariton lasers. A model based on the coupled kinetic equations for the free carriers, the excitonic reservoir and the polariton lasing state shows the same overall trend as observed in the experimental data, is being devised presently at the time of composition of this dissertation.

Finally, chapter VIII summarizes the entire dissertation and discusses three future projects which can originate from the work contained in this thesis.

Chapter II

Principles of Operation of Polariton Lasers

2.1 Introduction

The fundamental physics governing the operation and the various output characteristics of polariton lasers and non-equilibrium condensates is extremely rich, varied and highly multi-faceted. In semiconductors, the interaction of light and matter as mediated by the induced transition electric dipole moment, is often quite strong for excitonic states. In a solid-state optical cavity, a coherent and reversible exciton–photon interaction can give rise to two new bands of two-dimensional dressed states, called polaritons, which have characteristics inherited from their two constituents. These include, besides others, having a short lifetime, which is essentially determined by the cavity photon lifetime, and experiencing mutual attractions and repulsions, as mainly governed by the values of their excitonic non-linear parameters. The character of these short-lived radiative species is highly dependent on the immediate environment of the solid-state system in which it is created, making it particularly vulnerable to many-body dephasing and decoherence effects, as influenced by crystalline disorder and lattice imperfections. Most importantly these alter the output emission properties. For polariton lasers, all physical information about the system, in principle as well as in practice, is derived from the experimental study of the photons originating from the polaritons tunneling through the imperfect mirrors, out of the cavity. This makes a complete and all-encompassing theoretical investigation of these classes of condensed-matter systems quite complicated and deviations from standard models, usually devised for atomic systems, rather severe. This aspect will be discussed later in this chapter, in the context of rate-equation-based modeling of the light and polarization output characteristics, above the threshold.

The origin of spontaneous macroscopic quantum coherence in these lasers, which are inextricably coupled to several baths, individually describing excitation and irreversible loss, was first rigorously examined by Szymańska et al. [34]. This was approximately one decade after the proposal of the polariton laser [8]. The polariton laser, as well as other similar proposed mathematical constructs, such as an exciton boser [9], are all essentially based on efficiently utilizing the phenomenon of bosonic final-state stimulation of composite bosons [11]. Final-state stimulation, which is a characteristic defining feature of bosonic fields and particles, describes the process of non-linear enhancement of physical processes such as radiation, scattering or tunneling which would potentially magnify the population of bosonic species, which are the verge of undergoing this stimulation process. A necessary precursor to the activation of such a process, is that the overall population (or, more precisely, the appropriate bosonic occupation number) of a certain mode should exceed unity [35]. For example, for elementary excitations, such as exciton-polaritons, whose relaxation and thermalization rates are controlled by the shapes of their dispersion relations, final-state stimulation takes place when the overall occupation per mode centered at the mode (usually the zero-momentum state) exceeds unity. This is reflected in the experimental data shown in Fig. 2.1. This is a consequence of the finiteness as well as the two-dimensional nature of their density of states. As long as the bosonic character can be maintained (not too high a value for the excitation), and sufficient accumulation of these quasi-particles can be accomplished over a range of modes centered at the lowest-momentum state (via a balance between injection and irreversible losses), there should be resultant optical gain in the system.

The afore-mentioned gain arises from the macroscopic occupation of the ground-state mode. This is identical to, however quite dissimilar from true Bose-Einstein condensation, which is a second-order thermodynamic phase transition process. Throughout this dissertation, by polariton lasing or polariton condensation, a completely different kind of kinetically driven process is implied. More importantly, the present system, unlike atomic Bose-Einstein condensates, has the characteristic property of being an intrinsically non-equilibrium system. Because of the finite lifetime of polaritons, the condensate has to be continuously replenished by external excitation, and its final steady-state results from a dynamical balance of pumping and losses. The latter aspect will be discussed later in the context of the threshold condition of the strongly coupled microcavity. The polariton laser has several characteristics which are similar

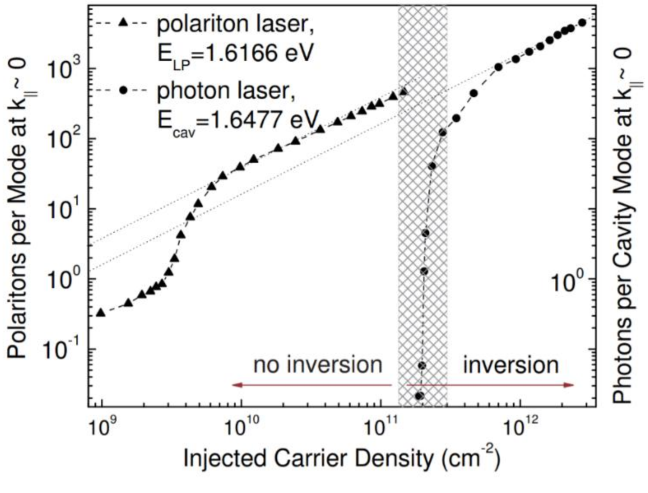

Figure 2.1. Number of lower polaritons and cavity photons per mode as a function of the injected carrier density for the polariton laser and photon laser regimes of operation, respectively. The gray zone marks the population inversion densities from band edge to 15 meV above the band edge. (H. Deng et al. Proc. Natl. Acad. Sci. **100**, 15318 (2003))

and even identical to a photon laser. However, the most important difference originates from the appreciable nonlinearities inherent in the interactions of polaritons with themselves, which are absent for uncoupled microcavity photons. The predominantly repulsive self-interaction of polaritons with other polaritons is essential for lasing in strongly coupled microcavities. Thus, this chapter commences with a discussion of the essential similarities and dissimilarities between photon and polariton lasers. This is followed by a discussion of the physics behind the nature of the output polarization of the polariton lasers, which will be more fully examined, experimentally as well as theoretically, in Chapters III, V and VI. This is particularly important in the context of the major theme of the present dissertation, which discusses polariton devices which are designed to achieve emission coherent light with well controlled polarization states. Finally, a short discussion on the rationale involved behind the construction of rate-equation-based models for polariton lasers is given.

2.2 Differences between Polariton and Photon Lasing

Polariton and photon lasers, fundamentally differ in the basic mechanisms by which net non-linear optical gains are generated in their respective active regions. The former depends on a phase-coherent stimulated scattering process whereas, the latter derives its non-linear coherent properties from having a net optical gain, originating from stimulated emission [5]. A net optical gain is only possible in a cavity, when there is net stimulated emission, which is greater than the medium absorption and spontaneous radiative recombination rates, and this is possible only above a certain value of the injected carrier density called the transparency carrier density. Further beyond transparency, this nonlinear gain has to surmount all the resonator and mirror losses to initiate and maintain photon lasing.

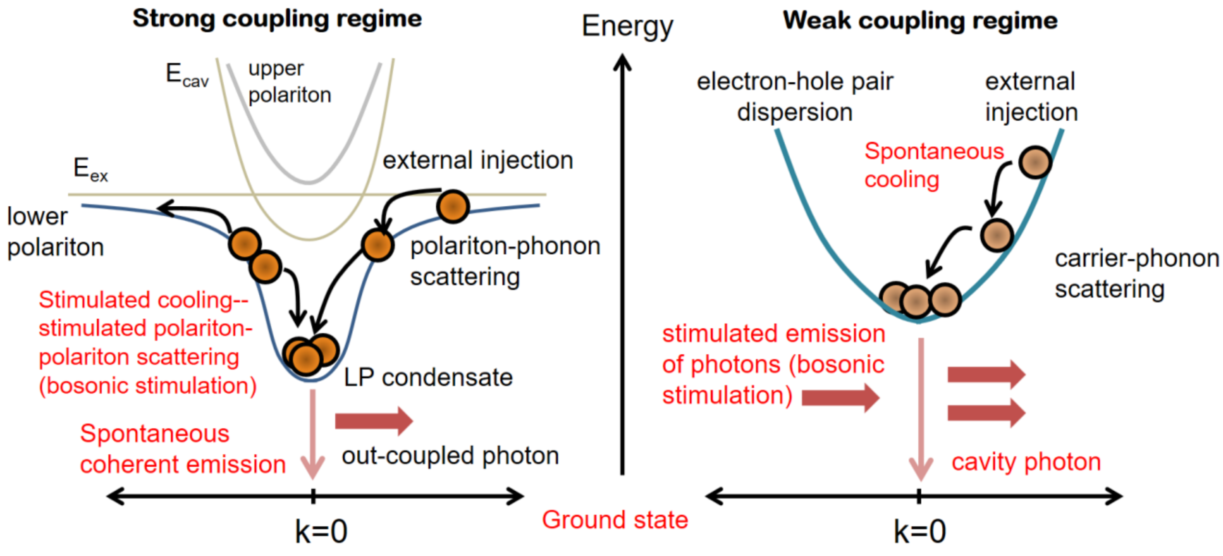

Figure 2.2. Schematic representation of the various fundamental underlying processes involved in the process of polariton lasing. (Courtesy of Professor Pallab Bhattacharya, Invited Talk entitled "Strong Coupling Phenomena, Polariton Lasers and Room Temperature Bose-Einstein Condensation" at UC Davis, December 3, 2013)

In contrast, in a polariton laser, the mechanism of final-state stimulation and the process of emission are fundamentally decoupled, which is the reason why no resultant fermionic carrier population inversion is not required. Further, the physical phenomena of intra-cavity absorption and re-absorption of light is already incorporated in the polariton quasiparticle picture [36]. This is because the polariton is the quantization of the energy which is coherently and reversibly exchanged between the emitter and the intra-cavity photon field. Thus, there is no necessity for absorption to be balanced by stimulated emission, which is one of the requirements for the accomplishment of threshold in photon laser. In polariton lasers, a macroscopic and coherent state of exciton-polaritons is generated by a dynamic condensation process, which involves polariton-phonon, polariton-carrier and polariton-polariton scattering, and finally stimulated polariton-polariton scattering. The latter is a phase-coherent process and is the relevant gain mechanism. The coherent exciton-polariton states, forming a degenerate condensate, generate coherent light by spontaneous radiative recombination. Unlike conventional lasers, polariton lasers emit coherent and monochromatic light by spontaneous radiative recombination, and not by stimulated emission.

Experimentally, polariton lasers show output emission properties which are quite similar to those of conventional photon lasers. In both cases, beyond some value of threshold, there is a significant nonlinear increase in the light output. Further, the light output also becomes spectrally, spatially and temporally coherent, and generally linearly polarized, in both cases. However, there are minor differences in the observed output characteristics. Usually, there is a blueshift of the peak emission energy originating from polariton-polariton repulsions, reflecting the particulate nature of the luminescent species involved. This, generally, does not take place in case of photon lasers unless the excitation density is very high, in which case band-filling effects might possibly become important. In polariton lasers, one also observes linewidth broadening

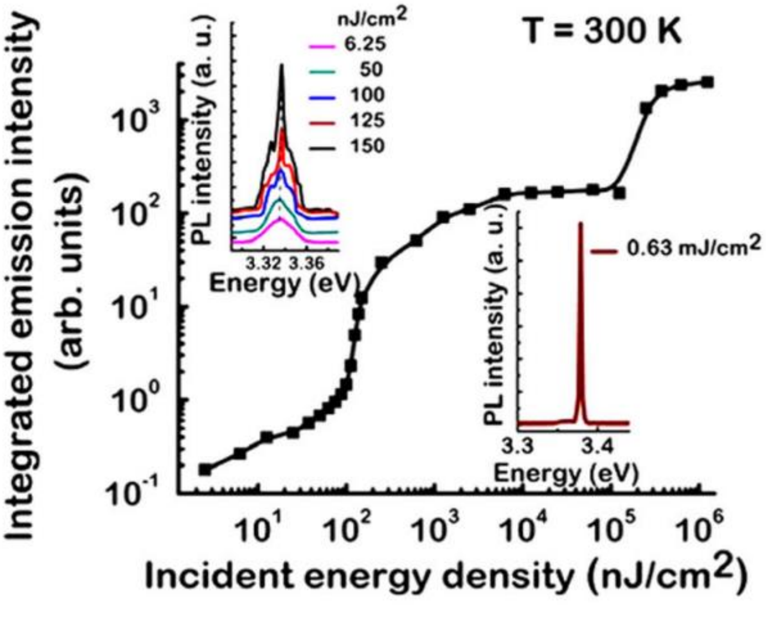

Figure 2.3. Variation of the emission intensity with excitation energy density at 300 K clearly showing the two thresholds for polariton and photon lasing. The insets show the corresponding emission spectra in the two lasing regimes. (A. Das et al. Phys. Rev. Lett. **107**, 066405 (2011))

slightly beyond the threshold. This also originates from the decohering nature of the polariton-polariton interaction process [37, 38]. All these experimentally observed differences are shown in Chapters III and V, in the context of the discussion of the output characteristics of polariton lasers.

However, the definitive distinguishing difference between a polariton laser and a photon laser, lies in the actual values of their respective thresholds, at which nonlinearities are observed in the output characteristics. Polariton lasing occurs when the net phase-coherent stimulated scattering rate to the ground state exceeds the polariton decay rate [39]. The polariton lifetime usually depends on the cavity photon lifetime and thus the quality factor of the cavity. The threshold condition, for polariton lasing, thus does not require transparency in the cavity, and can thus accomplished at very small values of excitation, as opposed to photon lasing in the same structure. The integrated emission intensity over the entire range of excitation power density, in a single GaN nanowire strongly coupled to a large-area dielectric microcavity is shown in Fig. 2.3. The two distinct thresholds, 3 orders of magnitude apart in excitation density, clearly demonstrating the very different natures of the origins of the nonlinear emissions [40].

This section concludes with a short discussion of the relative merits and demerits of polariton and photon lasers. There are two major advantages of polariton lasers over conventional semiconductor cavity mode-mediated photon lasers. Firstly, the lasing threshold current density is usually two to three orders of magnitude lower than that for conventional photon lasing in the same structure and thus they are more energy efficient. Further, the spectral coherence of the polariton laser is extremely good and the linewidth is not limited by the Schawlow-Townes limit as is the case for normal semiconductor lasers. Polariton lasers have demonstrated emission linewidths as narrow as ~ 10 μeV [41], which may be considered as ultranarrow as far as semiconductor coherent sources are concerned. In contrast, polariton lasers require high quality cavities, wherein strong coupling effects can be sustained and rather stringent design criteria with regards to exciton-photon coupling, detuning and their respective linewidths. Further operation in GaAs-based devices, the natural choice for its extremely advanced epitaxial and processing technologies, is hindered by relaxation bottleneck issues, and limited to low temperatures by virtue of rather modest excitonic binding energies and polariton splittings. The optical output power values (~ 1.8 mW in the best GaAs-based devices [11]) are also smaller than the values obtained for photon lasers.

2.3 The Origin of Polarization Beyond Threshold

The above-threshold light output of polariton lasers is usually linearly polarized. This characteristic is generally, only revealed in steady-state measurements. In contrast, the emission from a strongly coupled semiconductor microcavity is essentially unpolarized below the polariton laser threshold. This behavior has been experimentally observed for CdTe-based [42], GaAs-based [38] and GaN-based [18] polariton lasers. The measured excitation-dependent data showing the afore-mentioned trend, for a CdTe-based and GaAs-based polariton laser, are shown in Fig. 2.4 and Fig. 2.5, respectively. The goal of this section is to provide a simple explanation for this behavior. Microcavity polaritons, which are usually formed from the coupling of heavy-hole excitons with cavity photons, have two allowed spin projections (projections of the total angular momentum) on the axis of growth. In the absence of an external magnetic field, these two eigenstates, usually referred to as the ‘‘spin-up’’ and ‘‘spin-down’’ states, and their linearly polarized superpositions, have the same energy. Polariton-polariton interactions lift this degeneracy and bring about a mixing of the linearly polarized polariton states. Moreover, additional mixing comes from the longitudinal-transverse (LT) splitting of polaritons [42]. This splitting also gives rise to the precession of the polariton pseudospin vector around an effective magnetic field [43, 44]. Shelykh and co-workers first theoretically showed that assuming perfect thermal equilibrium and cylindrical symmetry of the microcavity, spin-dependent polariton-polariton interactions enable the formation of polariton condensates with a well-defined linear polarization [45]. They used a Hamiltonian density- based formulation and showed that the free

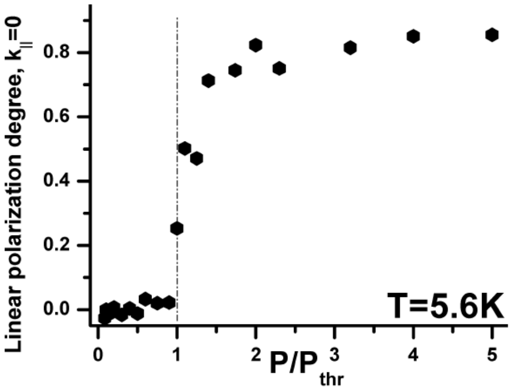

Figure 2.4. Degree of linear polarization as a function of the normalized pump power for a CdTe-based polariton laser. (J. Kasprzak, Ph.D. Thesis, Universite´ Joseph Fourier – Grenoble 1 (2006); The data have also been reported in J. Kasprzak et al., Phys. Rev. B **75**, 045326 (2007))

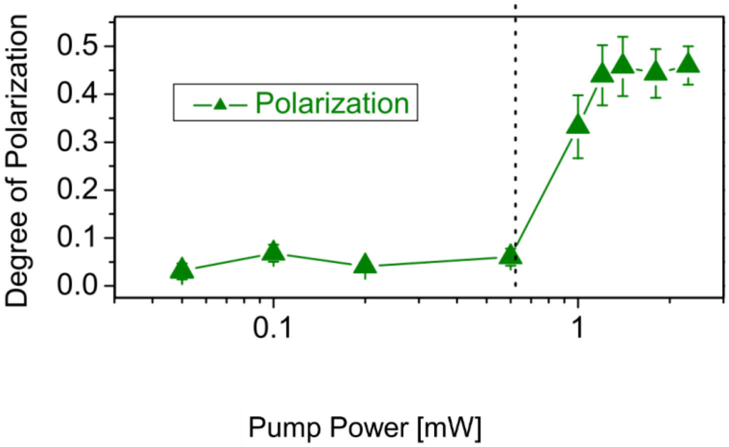

Figure 2.5. Degree of linear polarization as a function of the normalized pump power for a GaAs-based polariton laser. (R. Balili et al., Science **316**, 1007 (2007))

energy density of the condensate is minimized with the formation of linear polarization. This is so mainly because of fact that the polariton-polariton interactions are highly spin-anisotropic. In general, the strength of the interaction constant for polaritons with opposite spin (usually attractive) is typically much smaller than the interaction constant for same-spin polaritons (usually repulsive). Because of this, the polariton condensate is generally expected to be linearly polarized in the absence of external causes, which explicitly break the symmetry between the spin-up and spin-down components, such as an external magnetic field or spin-polarized excitation [46]. This lifting of spin degeneracy enables the realization of spin-polarized polariton lasers, as will be discussed in Chapter V.

Following the initial studies on steady-state linear polarization, a very intriguing property about the true nature of the output linear polarization was first reported by Baumberg and co-workers [47]. This was the observation of the buildup of the spontaneous vector polarization at room temperature in bulk GaN-based microcavities. The observational results are summarized in Fig. 2.6. Further explanation of the data in Fig. 2.6, will be provided subsequently. Above threshold, the emission was found to be instantaneously polarized, but with no preferential orientation. The Stokes vector of emitted light changed its direction stochastically in independent realizations of the polariton condensate, such that the steady-state time-integrated resultant output polarization remained zero at all excitations (Fig. 2.6 (c)). This was unlike the several low temperature experiments on BEC in CdTe- and GaAs-based multiple quantum well-based cavities in which the above-threshold linear polarization direction was preferentially oriented along one of the crystallographic axes [38, 42]. This so-called “pinning effect” is discussed in Chapter III. It is this pinning effect, which is probably caused by defects or lattice disorder or mirror birefringence, which enables the detection of steady-state linear polarization in the measurements shown in Figs. 2.5 and 2.6. An explanation of these observed phenomena, as was furnished by Baumberg and co-workers [47], follows.

Firstly, a simple mathematical treatment of the polarization properties of polariton condensates is provided. It may be remembered that the excitons-polaritons are spinor quasiparticles with two possible spin projections along the axis of growth. The so-called spin-up and spin-down pure states correspond to right-handed and left-handed circular polarizations of the emitted light. Therefore, the order parameter, or the many-body wavefunction of the polariton condensate, may be written as follows: $\mathbf{\Psi}(\mathbf{r}) = [\Psi_\uparrow (\mathbf{r})\ \Psi_\downarrow (\mathbf{r})]^T$, where $\Psi_\uparrow (\mathbf{r})$ and $\Psi_\downarrow (\mathbf{r})$ are the spin-up and spin-down components, respectively [47]. This complex two-dimensional vector, $\mathbf{\Psi}(\mathbf{r})$, also describes the in-plane component of the electric field of the photonic component of the polariton condensate [42]. The order parameter is usually normalized with respect to the overall condensate occupation number, at any given injection. The dimensionless concentration of the condensate state is $N_0 = (\mathbf{\Psi}^*. \mathbf{\Psi})$.

All the information about the output polarization state of the emitted light is encoded in the wavefunction. Thus, for example, the physical phenomenon of a purely linearly polarized condensate state can be mathematically expressed as $\mathbf{\Psi}^* \mathrm{X}\ \mathbf{\Psi} = 0$ [42]. The 3D polarization vector, **S** (also known as the Stokes vector in classical optics or as the pseudospin vector in quantum mechanics), can be related to the wavefunction components as follows: $S_x = \mathrm{Re}\,(\Psi_\uparrow^* \Psi_\downarrow)$, $S_y = \mathrm{Im}(\Psi_\uparrow^* \Psi_\downarrow)$, and $S_z = ½\,(|\Psi_\uparrow|^2 - |\Psi_\downarrow|^2)$ [7]. The pseudospin vector **S**, schematically shown in Fig. 2.7, encodes information both about the exciton-spin state and about the orientation of its dipole moment. The absolute degree of polarization of the condensate can be expressed as $\rho = (|\Psi_\uparrow|^2 + |\Psi_\downarrow|^2)/N_0$, where N_0 is the occupation number of the condensate. It is related with the degrees of linear, diagonal, and circular polarization ρ_l, ρ_d, ρ_c, respectively, by $\rho = \sqrt{\rho_l^2+\rho_d^2+\rho_c^2}$, where $\rho_{l,\,d,\,c} = 2S_{x,\,y,\,z}/N_0$.

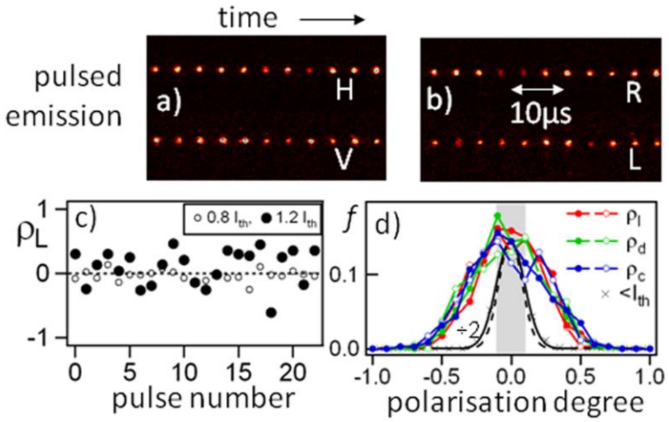

Figure 2.6. Above-threshold polarization-resolved emission when analyzing along (a) horizontal or vertical and (b) right or left circular bases. (c) Extracted linear polarization degree showing stochastic variation from pulse to pulse above and below threshold. (d) Histogram of the fraction of each polarization state f along linear, diagonal, and circular bases of nearly 2000 polariton condensates. Open and closed circles show repeated measurement with reversed polarization split (e.g., H/V and V/H), while crosses show below-threshold unpolarized emission statistics (curve divided by 2 to fit on scale, within detection sensitivity shaded gray and scaled dashed line). (J. J. Baumberg et al., Phys. Rev. Lett. **101**, 136409 (2008))

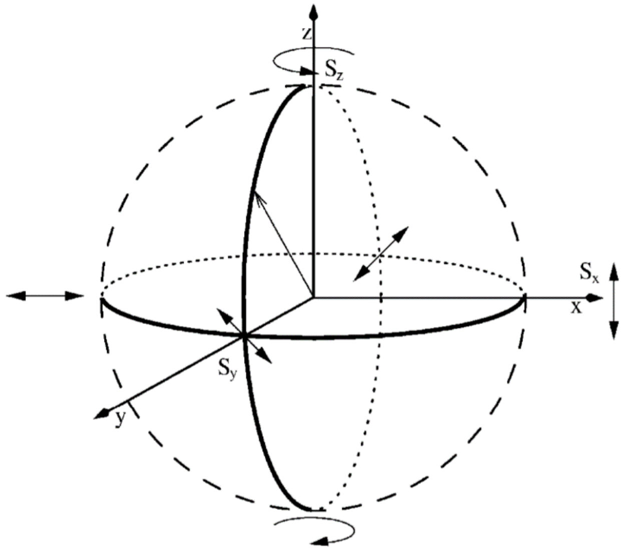

Figure 2.7. A Poincaré sphere with a pseudospin. The equator of the sphere corresponds to different linear polarizations, while the poles correspond to two circular polarizations. (K. V. Kavokin et al., Phys. Rev. Lett. **92**, 017401(2004))

In strongly coupled microcavities pumped below the condensation threshold, $|\boldsymbol{\Psi}| = 0$. Thus, also the sub-threshold emission from the cavity should be essentially unpolarized (Fig. 2.6 (c)). However, at the onset of threshold, the order parameter $\boldsymbol{\Psi}$ abruptly and discontinuously builds up due to the phase-coherent stimulated scattering of polaritons from the higher-energy states to the ground state [47]. This stimulated scattering of polaritons is due to a bosonic final-state stimulation process, and the above-mentioned build-up of the order parameter heralds the onset of a second-order phase transition. Using the method pioneered by Rubo [48], the time evolution of the probability of realizing a given value of the order parameter at a given time $P(\boldsymbol{\Psi},t)$ is governed by a nonlinear Fokker-Planck-type equation, as follows:

$$\partial P/\partial t = \nabla[\, P\nabla U(\boldsymbol{\Psi},t) + D(t)\nabla P \,], \qquad (1)$$

where the effective potential for the case of driven-dissipative spinor interacting condensates (open spin-polarized quantum systems) is given by:

$$U = \{[W_{out}(t)-W_{in}(t)]\,|\,\boldsymbol{\Psi}\,|^2 + \alpha|\,\boldsymbol{\Psi}\,|^4\}/4, \qquad (2)$$

and the diffusion coefficient $D=W_{in}(t)/4$ [47]. The effective potential in the order parameter space is shown in Fig. 2.8. Here $W_{in}(t)$ is the rate at which polaritons are introduced into the condensate which is dependent on the value of the excitation and the strength of the coupling of the condensate to the reservoir of excitons-like polaritons having large wave vectors (the excited states) [47]. $W_{out}(t)$ is the loss rate of the condensate mainly determined by the polariton radiative lifetime (there are other independent non-radiative channels, such as absorption of ground-state polaritons by phonons), while $\alpha > 0$ is the repulsive polariton-polariton interaction constant for polaritons having same spins. The population of the condensate N_0 is related to W_{in} and W_{out} via the Boltzmann equation:

$$dN_0(t)/dt = W_{in}(t)(N_0+1) - W_{out}(t)N_0 \qquad (3)$$

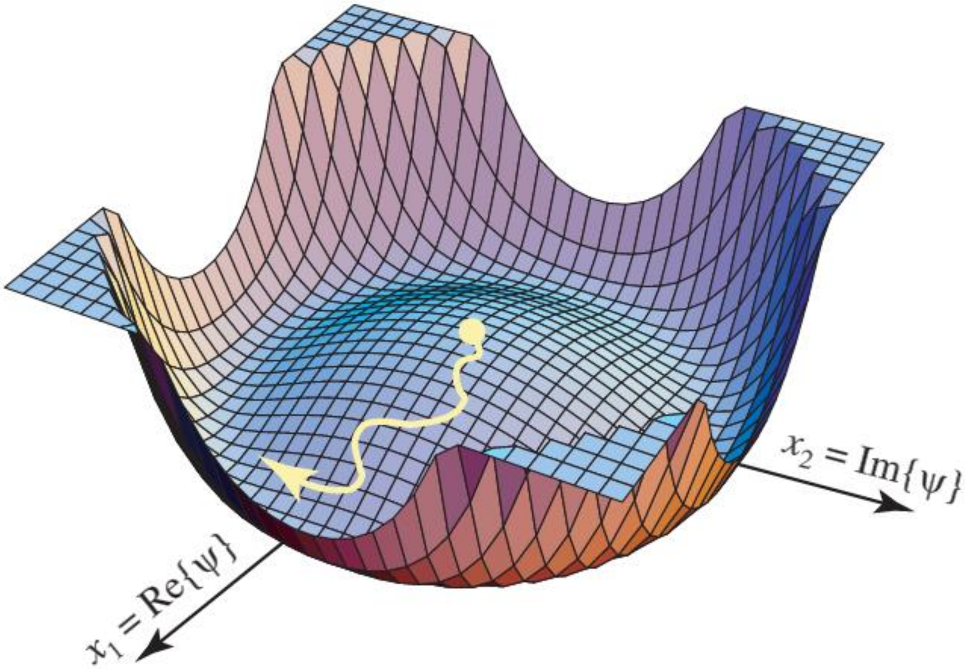

Figure 2.8. The effective potential in the order parameter space. The wavy yellow line depicts the stochastic evolution of the order parameter into the minima close to the circumference, as described in the text. (Yu. G. Rubo, Phys. Status Solidi A **201**, 641 (2004))

The "(N_0+1)" term is a hallmark of final-state stimulation. Above threshold, $W_{in}>W_{out}$ (the condensate is existent above threshold, so it has to be replenished faster than it radiatively decays) so that the potential of Eq. (2) has a maximum at $|\mathbf{\Psi}| = 0$ surrounded by a circular minimum at finite (non-zero) $|\mathbf{\Psi}|$. This allows for an efficient diffusion of the order parameter out of the center of the effective potential towards the minima, as shown in Fig. 2.8 [48]. The buildup of this order parameter explicitly results in a polarization buildup. The resulting value of the absolute polarization is fixed by the minimum of the effective potential (2), which has no preferential polarization, so that in each independent realization, the system chooses its polarization randomly keeping the absolute polarization degree same in all cases. This is summarized in Fig. 2.6 (d). This is the true underlying nature of the polarization of light emitted by a microcavity and is observable only in time-resolved measurements made on microcavities, in which the previously discussed “pinning effect” is absent. This phenomenon, of above-threshold spontaneous stochastic vector polarization, was also subsequently observed in a GaAs-based multiple quantum-well microcavity both in the strong coupling as well as in the weak-coupling regimes of operation [49].

2.4 Rate-Equation-Model Based Approaches for the Polariton Lasing Regime

The dissertation will later examine, in Chapters III, V and VI, how two distinct classes of rate equation-based approaches can be used to calculate the output characteristics of these polariton lasers. The different approaches used to study these lasers, usually vary in the respective mathematical treatments of the ground state of the lower polariton branch, which evolves with excitation into a coherent state. The purpose of this section is to study how an equation describing the time evolution of the polariton ground state, can be devised. When a simplified macroscopic mean-field theory-based approach is used to describe polariton-polariton interactions, the coherent polariton field can be shown to obey a complex driven-dissipative Gross–Pitaevskii equation (GPE) of the form [17]:

$$\frac{d\psi_\sigma}{dt} = \frac{1}{2}\left[W(t) - \Gamma_c\right]\psi_\sigma + \frac{1}{2}\left(\gamma + i\Omega\right)\psi_{-\sigma} - \frac{i}{\hbar}\left[\alpha_1\left|\psi_\sigma\right|^2 + \alpha_2\left|\psi_{-\sigma}\right|^2\right]\psi_\sigma \qquad (4)$$

The order parameter $\psi_\pm$ describes the many-body wavefunction of polariton condensates with +1 and -1 projections of spin to the structure axis. *W(t)* represents the pump term (the drive term), whereas Γ_c represents the decay of polaritons from the cavity (the dissipation term). Γ_c is inversely proportional to the polariton lifetime, which is mainly governed by the cavity quality factor. The constants Ω and γ, in units of inverse time, correspond to the effective magnetic field leading to the energy splitting of the polarized condensate states and to the spin relaxation term, respectively. The effective magnetic field originates from the LT splitting of polariton states, as described in the previous section. The first term of the equation, i.e., $\frac{1}{2}[W(t)-\Gamma_c]\psi_\sigma$ along with the polariton spin relaxation term, i.e., $\frac{1}{2}(\gamma)\psi_{-\sigma}$, together account for the non-linear character of the Schrödinger-like equation. Constants α_1 and α_2 describe the interactions of polaritons with the same and opposite spin projections, respectively. Equation (4) will be used in Chapters III and V, to model the time evolution of the polariton lasing state.

There are several important assumptions which have been made in the formulation of the above-mentioned equation. The kinetic equation term has not been explicitly written. It is assumed that the total polariton energies have been appropriately referenced or renormalized to take into account the same. One can also, in principle, introduce a potential energy term such as V_d, which takes into account the intra-cavity photonic disorder [50]. Elastic polariton-polariton collisions bring about a blueshift of the condensate energy by a value of $\alpha_1|\psi_\sigma|^2+\alpha_2|\psi_{-\sigma}|^2$. A similar term of the form $g_R n_R(\mathbf{r}, t)$, where $n_R(\mathbf{r}, t)$ is the density of reservoir exciton-like polaritons, can be introduced to simulate the elastic interaction of polaritons with the reservoir excitons [50]. The Gross-Pitaevskii equation is coupled to the equations of motion for the reservoir polariton and for the injected electron-hole plasma, as follows:

$$\frac{dN_r}{dt} = -\Gamma_r N_r - W(t)\left[\left|\psi_-\right|^2 + \left|\psi_+\right|^2 + 1\right] + W_e n_{e-h}(t) \tag{5}$$

$$\frac{dn_{e-h}}{dt} = \frac{J}{q} - \frac{n_{e-h}}{\tau_{e-h}} - W_e n_{e-h} \tag{6}$$

where, N_r is the exciton reservoir occupation, and $n_{e\text{-}h}$ is the occupation of the free carrier reservoir. It may be noted that all the states, except for the ground state, together constitute the reservoir. $W(t)$ defines the rate of the polariton relaxation towards the ground state, and is mathematically expressed as follows:

$$W(t) = a_{ph} N_r(t) + b_{pol} N_r^2(t) \tag{7}$$

Equation (7) considers two relaxation mechanisms, namely the polariton-phonon scattering characterized by the scattering rate a_{ph} and polariton-polariton scattering with the rate b_{pol}. Both of these mechanisms serve to replenish the ground-state polaritons. This approach, based on the complex driven-dissipative Gross–Pitaevskii equation (GPE) for modeling the condensate, has been shown to recover the elementary excitation spectra of non-equilibrium condensates, as predicted by more rigorous approaches such as the Keldysh Green function method [50]. This was done in the work of Szymańska et al. [34], which was alluded to in the introduction of this chapter. An alternative approach which doesn't directly invoke the polariton wavefunctions and is based on a quasi-analytic formalism devised by Iorsh et al. [51], is discussed in great detail in Chapter VI. The spin-dependent version of the said formalism has been shown to have good agreement with the measured data in Chapter VI.

2.5 Summary

In summary, this chapter presents some of the key concepts and features of non-equilibrium polariton condensates. Polariton and photon lasing have been compared, distinguished and their relative merits and demerits have been discussed. The nature of output polarization of polariton lasers, which encodes a lot of important of physics of polaritons, has also been discussed. Particularly, the origin of the linear polarization in polariton lasers has been discussed at length. Finally, the chapter concludes with a discussion of a generalized Gross–Pitaevskii equation used to model the low-energy polariton states.

Chapter III

Output Linear Polarization Characteristics of GaN-Based Polariton Diode Lasers

3.1 Introduction

As has been motivated in the introduction to this dissertation, real world practical use of polariton lasers as solid-state optoelectronic devices, which can potentially compete with and even displace conventional semiconductor laser diodes, necessitates room temperature operation with electrical injection. The major progress, with regards to this goal, was made at the University of Michigan, where Bhattacharya and co-workers demonstrated a room-temperature GaN-based electrically injected polariton laser. The breakthrough was achieved by replacing the surface-emitting geometry, which had been a defining feature of semiconductor microcavities wherein strong coupling-based studies had previously been conducted, by the edge-emitting geometry characteristic of in-plane Fabry-Pèrot lasers. This circumvents the problem of electrical injection through thick dielectric Bragg reflector (DBR)-based mirrors, which potentially increases the series resistance of the diodes. The uniqueness of the present polariton device lies in the fact that simultaneously both a low resistance diode can be processed as well as strong optical feedback can be achieved with high quality laterally deposited DBR mirrors.

This edge-emitting geometry has been used throughout this dissertation to design and process polariton laser devices. In the polariton laser devices described in this chapter as well as the spin-polarized polariton lasers studied in Chapter VI, the directions of cavity resonance and flow of electrical current are mutually orthogonal. A schematic representation of the device highlighting this aspect, is shown in Fig. 3.1. An SEM image of one of the devices is shown in Fig. 3.2. All of these devices also have bulk nominally intrinsic GaN as their active regions.

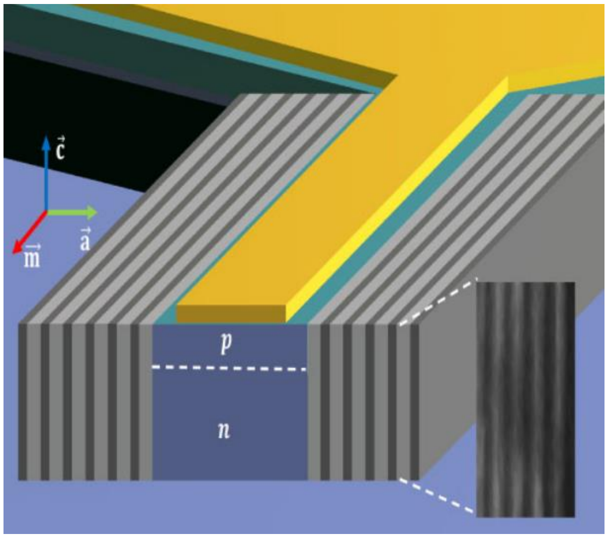

Figure 3.1. Schematic representation of the GaN microcavity diode. The inset shows a scanning electron microscopy image of the SiO_2/TiO_2 DBR mirror on one side. (Bhattacharya et. al., Phys. Rev. Lett. **112**, 236802 (2014); Featured in *Physics* and selected as Editors' Suggestion)

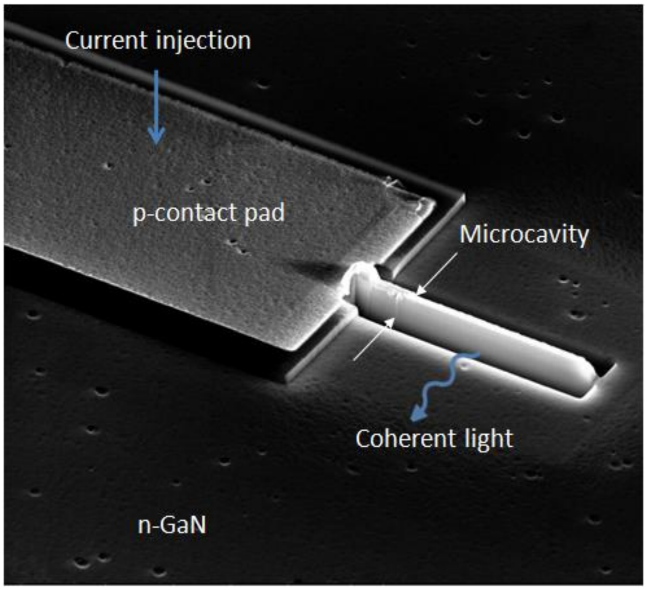

Figure 3.2. Scanning electron microscopy image of the GaN polariton laser diode. (Courtesy of Dr. Thomas Frost, formerly of the Bhattacharya Research Group, University of Michigan)

3.2 A Polariton Laser Diode as a Low Power Polarized Source

A stable linearly polarized coherent ultraviolet (UV) or deep UV light source is required for biochemical analysis, photo-alignment of nematic liquid crystals, eye surgery, and other industrial applications [52-56]. A single source or an array, to get higher powers, would be adequate for such applications. Current planar GaN-based UV lasers have threshold currents ~ 10 kA/cm^2 or higher. A polariton laser is an inversionless coherent light source operating in the strong coupling regime of light-matter interaction. Exciton-polariton lasers have been realized with suitable semiconductor microcavities with both optical and electrical pumping. Coherent emission is produced by spontaneous radiative recombination from a macroscopic, coherent and degenerate exciton-polariton condensate. The non-linear threshold of a polariton laser is lower than that of a conventional photon laser because the former does not require the inversion of electronic population and quantum degeneracy may be reached at very low polariton densities.

An important characteristic of the output of a polariton laser is its polarization. Below the non-linear threshold, the optical output is essentially unpolarized. As the non-linear threshold is reached, there is spontaneous build-up of linear polarization in the emission spectra, which is a consequence of spontaneous symmetry breaking in the degenerate condensate. The linear polarization results from a breaking of the ground state degeneracy into two closely spaced states. Above threshold the condensate occupies the lower of these two states and the linear polarization of the emission corresponds to this state.

In this chapter, an experimental study of the output linear polarization characteristics of a GaN-based electrically pumped microcavity polariton laser, is described. Electrically pumped bulk GaN microcavity polariton lasers operating at room temperature have been studied. The devices are characterized by a threshold current density in the range of J_{th} ~

125 A/cm^2 to 375 A/cm^2, a detuning ranging from ~ -4 meV to -13 meV and a strong coupling in the microcavity characterized by a Rabi splitting of ~ 33.9 to 35.5 meV. In particular, the steady state linear polarization build up, caused by polarization pinning, in the output of multiple devices, is investigated. It is observed that the emission is unpolarized below the non-linear threshold and is linearly polarized above it with a maximum polarization of ~ 22 %. For higher injection currents, the degree of polarization decreases. It is also observed that in one device the non-linear threshold for the linear polarization resolved output is significantly lower than that for the unresolved output, a hitherto unobserved phenomenon, which possibly indicates that the microcavity may be spatially inhomogeneous and the polarization splitting is different in different domains.

3.3 Polariton Lasing and Strong-Coupling Characteristics

In the present study, several identical electrically pumped bulk GaN-based microcavity polariton lasers fabricated from a single epitaxially grown heterostructure sample as shown in Fig. 3.3(a), have been characterized. The device heterostructure was grown by plasma-assisted molecular beam epitaxy on c-plane n-type GaN-on-sapphire substrate. The processing of the diodes is initiated by selective deposition of Ni-Au p-contact, followed by rapid thermal annealing at 550^o C in an air ambient for two minutes. Next a 5 μm x 40 μm cavity region is defined by standard UV lithography and high density plasma etching, down to the substrate through the $In_{0.18}Al_{0.82}N$ layer. This is followed by deposition of 1 μm SiO_2 contact pads and subsequent deposition of Ti/Au interconnect metal for both p- and n- contacts. The final dimensions of the cavity, 690 nm (5λ) length x 40 μm width are patterned by focused ion beam (FIB) etching. Six and seven pairs of SiO_2/TiO_2 distributed Bragg reflector (DBR) mirrors are deposited on opposite sides of the FIB etched cavity by electron beam evaporation. All measurements reported here have been done at room temperature. The microcavity quality factor, Q, and the corresponding cavity mode lifetime, τ_c, are determined to be ~ 1700 and ~ 0.3 ps, respectively, from room temperature microphotoluminescence measurements. The microphotoluminescence data is shown in Fig. 3.3(c).

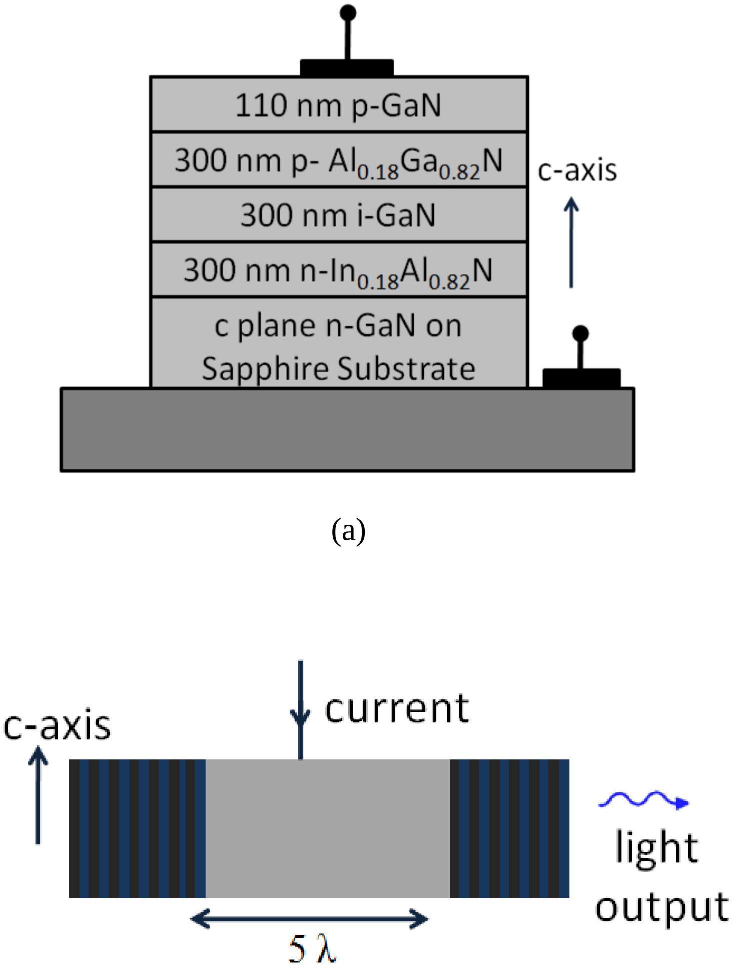

(a)

(b)

Figure 3.3 (a) Schematic representation of the double heterostructure GaN microcavity diode (not drawn to scale), (b) schematic representation of the edge emission geometry of the polariton laser diode.

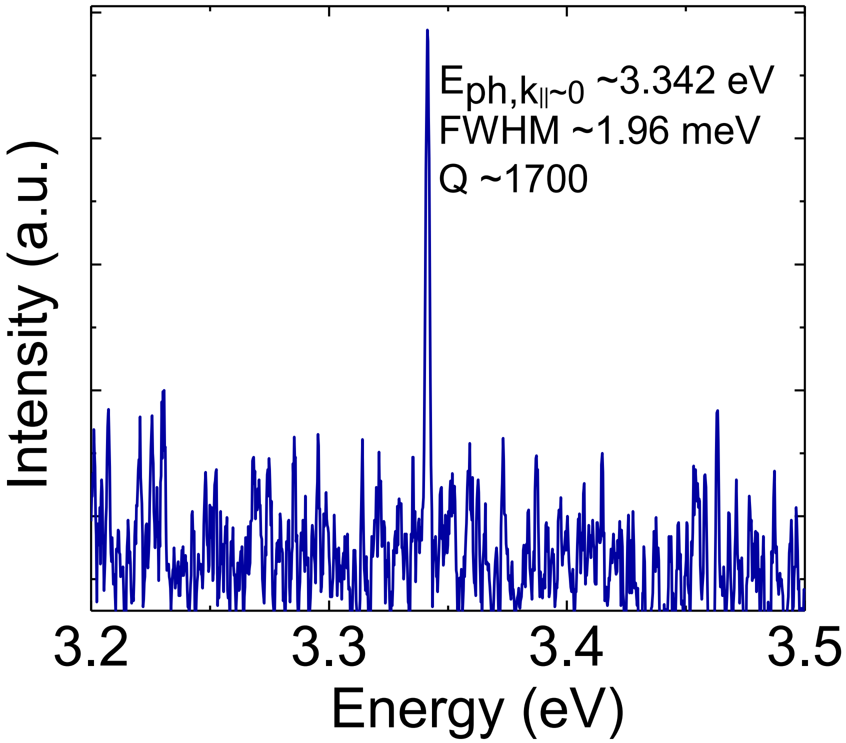

(c)

Figure 3.3 (c) Measured microphotoluminescence spectrum of the GaN microcavity.

The cavity quality factor, Q, of the bulk GaN-based optical micro-resonator and the corresponding cavity mode lifetime τ_C are determined to be ~1700 and ~ 0.3 ps, respectively, from room-temperature microphotoluminescence measurements. The microcavity diode was optically excited non-resonantly with a frequency-tripled Ti-sapphire laser (at an excitation wavelength of 266 nm) focused to a spot size of ~50 μm in diameter on one facet of the device, along the axis of cavity resonance, and the photoluminescence was collected from the other facet of the device and transmitted by an UV multimode optical fiber to a monochromator having a spectral resolution of ~ 0.03 nm. Figure 3.3(c) shows the measured cavity resonance, which has a full-width-at-half-maximum (FWHM) of ~ 1.96 meV centered at the peak emission energy of 3.34 eV.

Angle-resolved electroluminescence measurements were made to ascertain the strong coupling regime of operation of the devices and to determine the polariton dispersion characteristics. The measurements were carried out at a low value of continuous wave (CW) current injection (later confirmed to be 0.95 J_{th}, where J_{th} is the non-linear threshold to be described later). From the analysis of the measured sub-threshold lower polariton (LP) dispersion characteristics, in the framework of the 2x2 coupled harmonic oscillator model, the cavity-to-exciton detuning δ and vacuum-field Rabi splitting Ω of two devices are found to be in the ranges of -4 meV to -13 meV and 33.9 meV to 35.5 meV, respectively. The dispersion curves are calculated assuming the exciton linewidth of 6 meV. The data are shown in Fig. 3.4. In the following, the polariton lasing features are described in more detail.

The output light-current (L-I) characteristics of the devices were determined by recording the electroluminescence in the direction normal ($k_{||}$~0) to the Bragg mirrors (zero angle), as a function of continuous wave injection current. The LP emission intensities were recorded by a photomultiplier tube after spectrally filtering the output luminescence through an imaging monochromator. The output power was also directly measured with an optical power meter at sufficiently high injections above threshold. Both techniques yielded identical trends. As shown in Fig. 3.5 (a), a non-linear threshold signaling the onset of stimulated scattering is observed at a current density of J_{th} ~ 262.5 A/cm^2. The corresponding LP density at threshold is 3.88 x 10^{16} cm^{-3}, calculated with an excitonic radiative recombination lifetime of 0.71 ns. The non-linear region of the electroluminescence is characterized by a slope of ~13.7 and the enhancement of the output coherent luminescence over the active lasing regime is ~ 3.5 orders of magnitude. Both values are comparable to the corresponding characteristics of the best optically pumped CdTe-based, GaAs-based and GaN-based polariton lasers reported in the literature and are significantly better than those reported for electrically pumped devices. The onset of non-linearity and threshold are accompanied by an abrupt reduction of the LP emission linewidth and

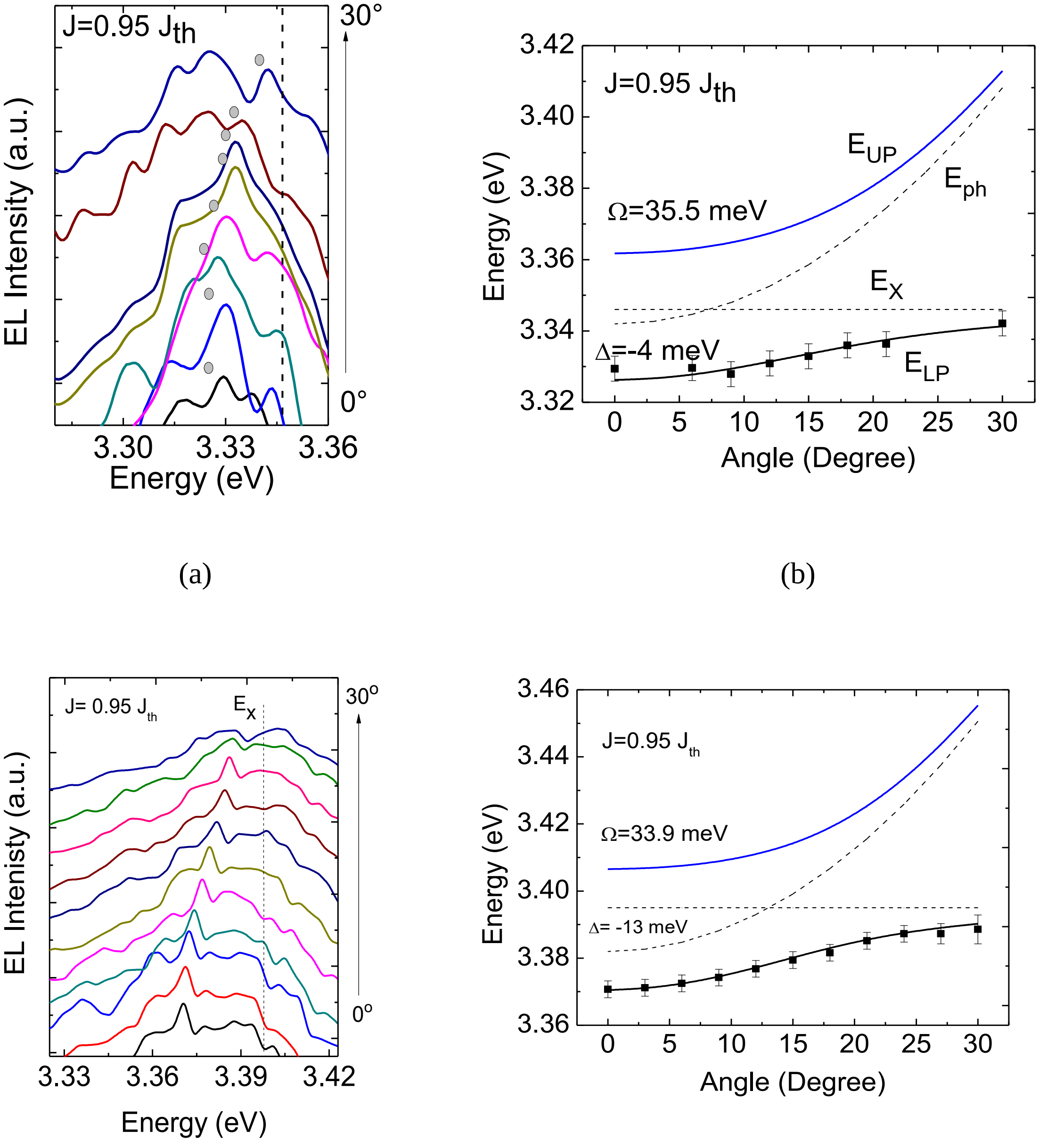

(a) (b)

(c) (d)

Figure 3.4. (a) and (c) Measured five point moving average filtered angle-resolved electroluminescence of Devices 1 and 5 respectively. The spectra are offset vertically for clarity. The dashed lines represent the exciton transitions; (b) and (d) corresponding polariton dispersion characteristics of Devices 1 and 5 respectively.

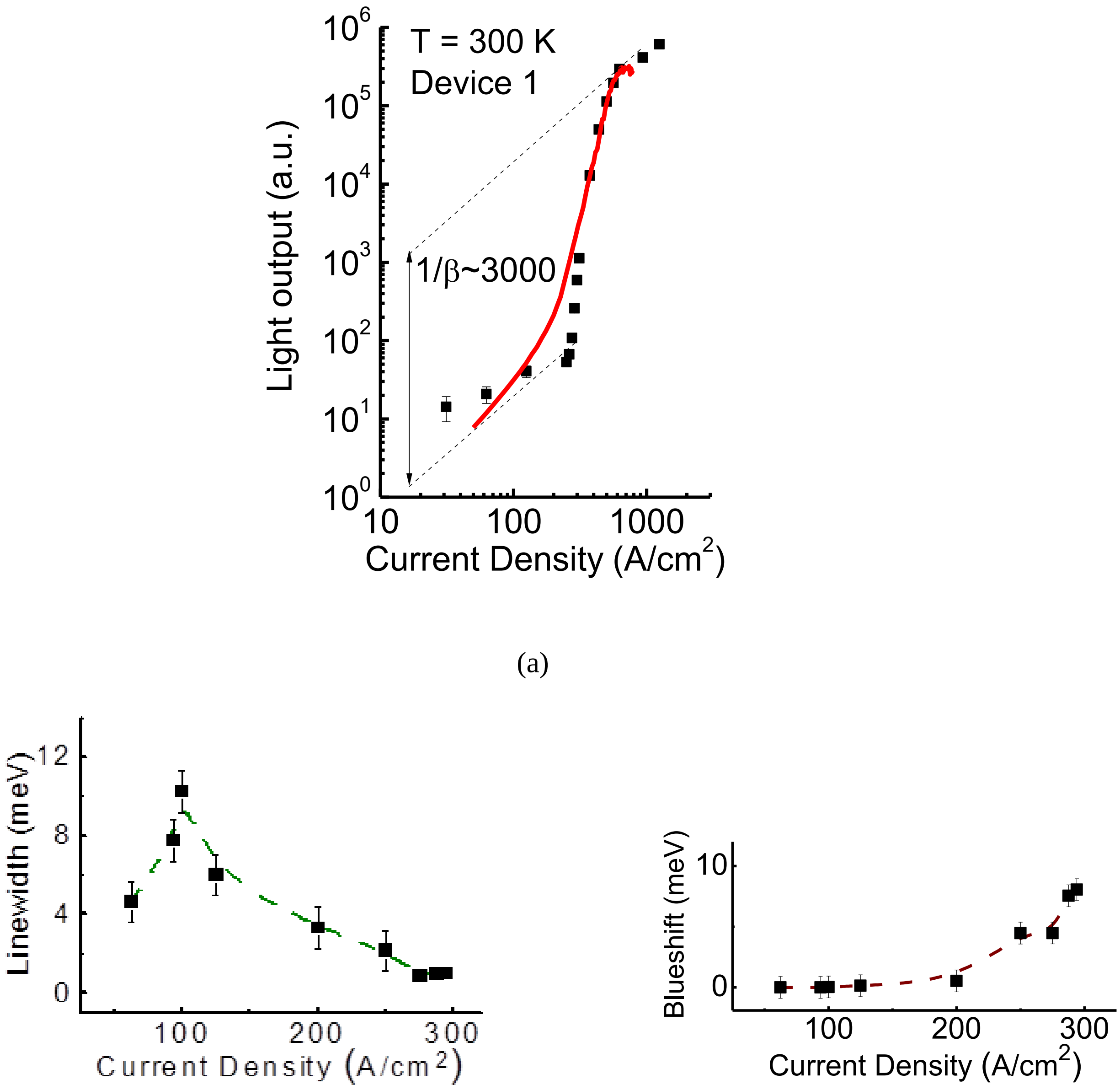

(a)

(b)

(c)

Figure 3.5 (a) Normal incidence ($k_{\|} \sim 0$) LP electroluminescence intensities recorded as a function of injected current density. The solid line represents theoretically calculated values, (b) LP emission linewidth as a function of injected current density, (c) blueshift of the LP electroluminescence peak emission as a function of injected current density. The dashed lines in (b) and (c) are guides to the eye.

pumped CdTe-based, GaAs-based and GaN-based polariton lasers reported in the literature and are significantly better than those reported for electrically pumped devices. The onset of non-linearity and threshold are accompanied by an abrupt reduction of the LP emission linewidth and a blue-shift of the LP electroluminescence peak energy (~ 8 meV) shown in Figs. 3.5 (b) and (c), respectively. The minimum measured emission linewidth is ~ 870 μeV, which corresponds to a LP coherence time of ~ 4.8 ps. The spontaneous radiative recombination lifetime of the lower polaritons in the condensate is estimated as $\tau_{LP} = \tau_C / |C(k_{||} = 0)|^2 = 0.6$ ps. With further increase of the injection current, the transition from strong coupling to weak coupling takes place and at J = 36.8 kA/cm^2 conventional photon lasing due to population inversion is observed. The two-threshold lasing behavior is shown in Fig. 3.6.

The polariton occupation in momentum space at different injection levels was also measured by angle-resolved electroluminescence in several devices. The occupation is calculated from the output power measured with an optical power meter after spectrally filtering the part of the electroluminescence spectrum centered on the lower polariton resonances. The polariton occupation number per $k_{||}$ state is calculated using the relation, $I_{LP} = \frac{\eta n_{LP}^{\infty}(k_{||}) |C(k_{||})|^2 Mhc}{\tau_C \lambda}$ [14], where η is the collection efficiency, $\tau_C / |C(k_{||})|^2$ is the spontaneous radiative recombination lifetime of the lower polaritons, M is the number of transverse states included in the detection cone, and $|C(k_{||})|^2$ is the photon fraction at a wave vector $k_{||}$. The number of states within the detection cone is given by $M = D^2 / 16 (k_o \Delta\theta)^2$, where D is the diameter of the emission spot, $k_o = 2\pi / \lambda$ (the free-space wave number) and $\Delta\theta$ is the detection half angle. The polariton condensate occupation numbers are very similar in all the devices. Representative data are shown in Fig. 3.7. A random and non-thermal LP occupation below threshold transforms to a peaked

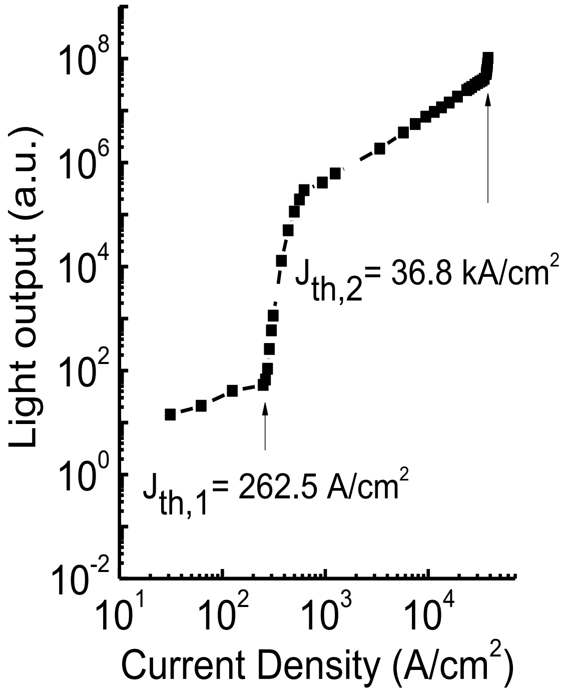

Figure 3.6. Two threshold lasing behavior with the nonlinearities due to polariton and conventional uncoupled cavity mode-mediated photon lasing, respectively.

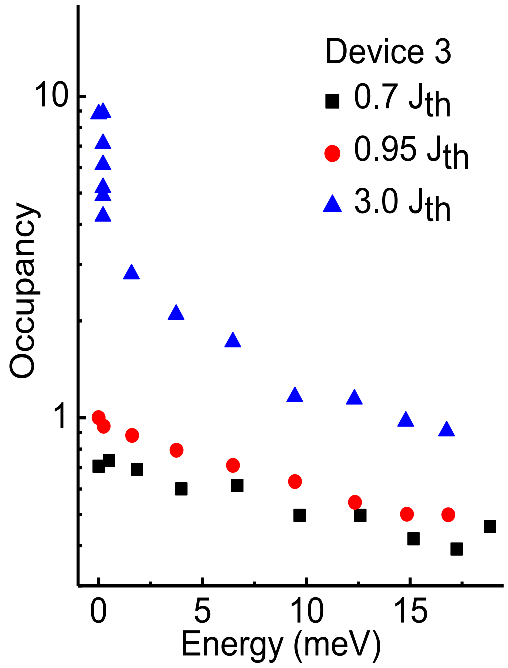

Figure 3.7. LP ground state occupancy for different $k_{||}$ states as a function of injection, determined from angle-resolved electroluminescence measurements.

occupancy at $k_{||} \sim 0$ above threshold, signaling the formation of a coherent polariton non-equilibrium condensate. There is no evidence of a relaxation bottleneck at any injection.

3.4 Steady-State Output Linear Polarization Characteristics

The degree of linear polarization of the polariton emission in the normal direction ($k_{||} \sim 0$) has been measured as a function of injection current in multiple devices. Figure 3.8 is a plot of the electroluminescence intensity as a function of the angle of the linear analyzer. Below the non-linear threshold, the emission is depolarized. Above threshold, a maximum linear polarization of ~ 22 % is recorded for an injection level of 275 A/cm$^{2.}$ The linear polarization is found to be preferentially oriented along the $[1\bar{1}00]$ crystallographic axis in all the devices.

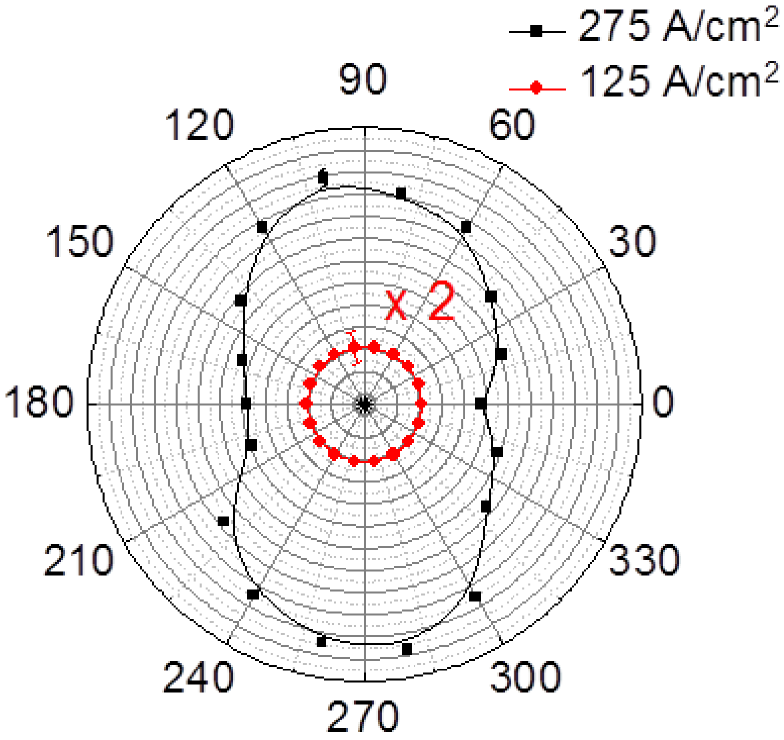

Figure 3.8. Polar plots of the normal incidence ($k_{||} \sim 0$) LP electroluminescence intensities recorded as a function of angle of linear analyzer below and above threshold of Device 1 (The single error bar shown in this figure is common to all the corresponding data points)

Figures 3.9 (a) and (b) depict the measured steady state linear polarization of the output LP electroluminescence as a function of the injection current for two devices. The output is essentially unpolarized below the threshold value, the degree of linear polarization being below the detection limit of the measurement system. At threshold, there is a sharp increase in linear

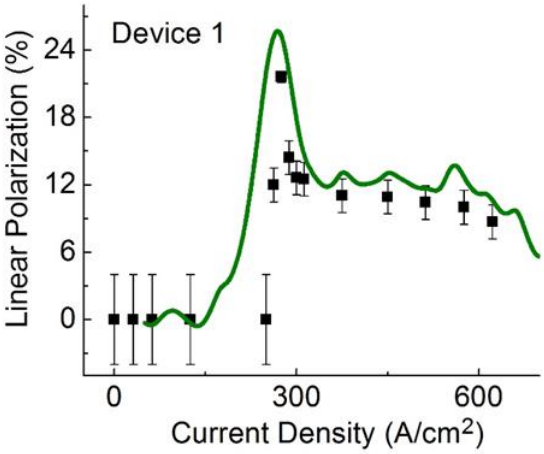

(a)

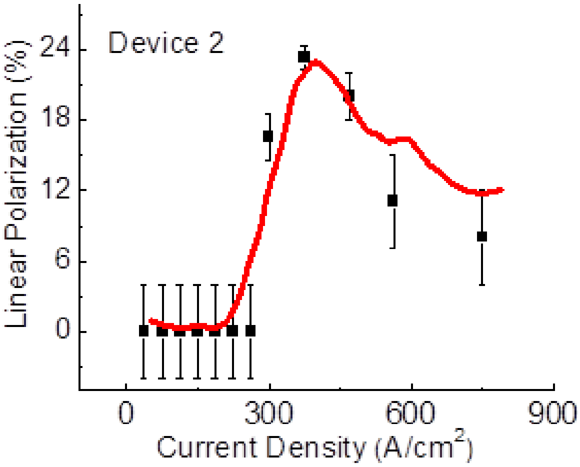

(b)

Figure 3.9 (a) and (b) Measured steady-state degree of linear polarization of Device 1 and Device 2, respectively, as a function of injected current density. The solid line represents the theoretically calculated values.

polarization due to stimulated LP scattering from the unpolarized reservoir to the polarized seed condensate in the presence of a small linear polarization splitting [57]. This is followed by a peaking and a steady decrease at higher injection, which is the depinning effect [18]. The depinning effect is a result of strong polariton-polariton repulsive interactions and self-induced Larmor precession of the Stokes vector of the condensate [18, 58]. The measured thresholds for linear polarization agree with the non-linear threshold in the light-current characteristics within the limits of experimental accuracy.

3.5 Linear Polarization Resolved Light-Current Characteristics

Polarization-resolved light-current characteristics were also measured and are plotted alongside the polarization integrated characteristics for two devices in Figs. 3.10 (a) and (b). The data of Device 2 in Fig. 3.10 (b) indicate that the value of the threshold current density remains unchanged for the two cases within the experimental accuracy. In contrast, similar data for Device 1 shown in Fig. 3.10 (a) indicate a reduction of the threshold current density of the polarization-resolved output by ~ 70 A/cm^2 compared to that of the polarization unresolved output as one can clearly see in the inset. This effect was only observed in one device, nonetheless during repeated measurements. It may be remembered that this device also exhibited the highest degree of non-linearity and strong coupling over a wide injection range.

The lower threshold of a specific linear polarization resolved electroluminescence probably results from a spatially inhomogeneous polarization splitting in the GaN microcavity, similar to what has been observed before in a CdTe microcavity [57, 59]. Some parts of the sample may be characterized by a large splitting of the linearly polarized modes and a specific linear polarization build-up occurs with a lower threshold. In other domains, the polarization splitting is negligibly small, resulting in emission which will be unpolarized in the steady state.

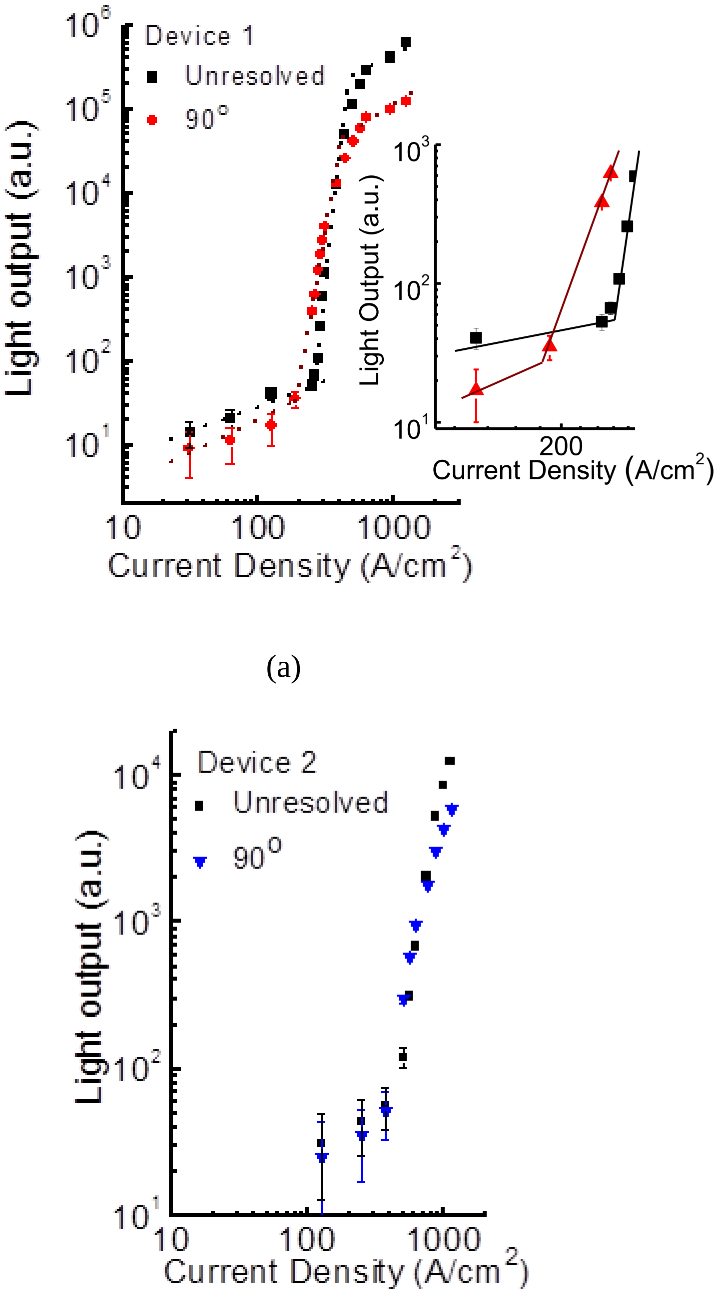

(a)

(b)

Figure 3.10 (a) and (b) Linear polarization-resolved (along 90° angle of the linear analyzer) and unresolved light-current characteristics of Device 1, and Device 2, respectively. The inset of (a) shows an enlargement highlighting the different thresholds.

The lowering of threshold observed here is less than the expected factor of 2 due to deviations in the microcavity characteristics from an ideal case. Nonetheless, this is the manifestation of inhomogeneity, probably arising from defects, in the linear polarization resolved electroluminescence of a polariton laser. Similar, albeit not identical, results have been observed in InGaAs microcavities, under non-resonant circularly polarized optical pulsed excitation, where the transition from the strong- to the weak-coupling regime takes place with increasing excitation at different powers for polaritons with opposite spin polarizations and is determined by the relative populations of the polaritons with opposite spin orientations [60, 61].

3.6 Theory of Output Linear Polarization of Polariton Diode Lasers

The experimental results were theoretically analyzed by virtue of a fruitful collaboration with Professor Alexey Kavokin at the University of Southampton, England and Professor Ivan Iorsh at the National Research University for Information Technology, Mechanics and Optics (ITMO), St. Petersburg. The theoretical model was primarily devised by Professor Kavokin and the computation was primarily done by Professor Iorsh. The experimental results have been analyzed by modeling the kinetics of the system with the four-coupled stochastic differential equations [18, 58]:

$$\frac{d\psi_\sigma}{dt} = \frac{1}{2}\left[W(t) - \Gamma_c\right]\psi_\sigma + \frac{1}{2}\left(\gamma + i\Omega\right)\psi_{-\sigma} - \frac{i}{\hbar}\left[\alpha_1\left|\psi_\sigma\right|^2 + \alpha_2\left|\psi_{-\sigma}\right|^2\right]\psi_\sigma + \theta_\sigma(t) \tag{1}$$

$$W(t) = a_{ph}N_r(t) + b_{pol}N_r^2(t) \tag{2}$$

$$\frac{dN_r}{dt} = -\Gamma_r N_r - W(t)\left[\left|\psi_-\right|^2 + \left|\psi_+\right|^2 + 1\right] + W_e n_{e-h}(t) \tag{3}$$

$$\frac{dn_{e-h}}{dt} = \frac{J}{q} - \frac{n_{e-h}}{\tau_{e-h}} - W_e n_{e-h} \tag{4}$$

The order parameter $\psi_\pm$ describes the many body wavefunction of polariton condensates with +1 and -1 projections of spin to the structure axis, N_r is the exciton reservoir occupation, and n_{e-h} is the occupation of the free carrier reservoir. $W(t)$ defines the rate of the polariton relaxation towards the ground state. Two relaxation mechanisms, namely the polariton-phonon scattering characterized by the scattering rate a_{ph} and polariton-polariton scattering with the rate b_{pol}, have been considered. In all probability, the phonon scattering process (the first term on the right-hand side of equation (2)) does not involve a single scattering event but rather proceeds through a cascade of phonon emissions. Nevertheless, the phenomenon of final-state stimulation is present and for the rate of polariton-polariton scattering, it is proportional to square of the reservoir occupation as the rate of any two-body collision process. The first term in the right-hand side of equation (2) describes the phonon induced scattering of excitons and is linearly dependent on the exciton reservoir occupation. The two-body collision process is described by the second term in equation (2) which is quadratic in the exciton reservoir occupation. Γ_c is inversely proportional to the polariton lifetime, which is mainly governed by the cavity quality factor. The constants Ω and γ correspond to the effective magnetic field leading to the energy splitting of the polarized condensate states and to the spin relaxation term, respectively. Constants α_1 and α_2 describe the interactions of polaritons with the same and opposite spin projections, respectively. Phenomenological constants Γ_r and W_e describe the decay rate of the excitons in the reservoir and the exciton formation rate, respectively.

The noise term $\theta(t)$ is defined by its correlators:

$$\left\langle \theta_\sigma(t)\theta_{\sigma'}(t')\right\rangle = 0 \qquad (5)$$

$$\left\langle \theta_\sigma(t)\theta^*_{\sigma'}(t')\right\rangle = \frac{1}{2}W(t)\delta_{\sigma\sigma'}\delta(t-t') \qquad (6)$$

The system of equations (1-4) is then numerically solved using the stochastic Runge-Kutta algorithm. For the numerical calculations, the following parameters corresponding to conventional GaN -based laser diodes are used [51]: Γ_c = 1.3 ps^{-1}, γ = 0.0035 ps^{-1},Ω = 0.03 ps^{-1}, α_1 =0.0001 ps^{-1}, α_2 = -0.1α_1, a_{ph} = 10^{-11} ps^{-1}, b_{pol} = 10^{-12} ps^{-1}, Γ_r = 0.001 ps^{-1}, W_e = 0.01 ps^{-1}, τ_{e-h} = 2000 ps. The ground state occupation number is given by $n(t) = |\psi_+|^2 + |\psi_-|^2$ and the components of the condensate pseudospin linked to the output light polarization are:

$$S_x = \mathrm{Re}\left(\psi_+^*\psi_-\right) \tag{7}$$

$$S_y = \mathrm{Im}(\psi_+^*\psi_-) \tag{8}$$

$$S_z = \frac{1}{2}(|\psi_+|^2 - |\psi_-|^2) \tag{9}$$

Time and noise averaged signals have been recorded during the measurements. Namely the degree of linear polarization is given by $s_x = \left\langle \int dt S_x(t) / \int dt n(t) \right\rangle$, where brackets symbolize averaging over the noise. The results of the experiments and the numerical simulations are compared as follows. Figure 3.5 (a) shows the calculated dependence of the condensate occupation number $n(t)$ on the injected current density alongside the measured data. In order to obtain the theoretical values of the degree of linear polarization for Device 2, the following parameters have been varied with respect to the analysis for Device 1: the spin relaxation rate, γ, has been changed from 0.0035 ps^{-1} to 0.005 ps^{-1} , the polariton radiative rate Γ_c has been changed from 1.3 ps^{-1} to 1 ps^{-1} and the internal magnetic field Ω has been changed from 0.03 ps^{-1} to 0.05 ps^{-1}. It is observed that the calculated linear polarization shows a good agreement with the measured data, in general. One can see that the difference in current density dependence of the linear polarization between devices 1 and 2 is chiefly due to the different spin relaxation and polariton radiative decay rates. The spin relaxation rate and the polariton radiative decay rate is ~ 30% faster and ~ 30% slower respectively, in device 2 as compared to device 1.

These differences are ascribed to the different magnitudes of photonic disorder in the two devices. The value of the peak polarization is ~ 22 % for both devices and is governed by the ratio of the polarization relaxation rate γ and the polariton radiative decay rate Γ_c.The lower is this ratio, the shorter is the time the polariton condensate possesses for relaxation to the lowest energy polarization state. This ratio and thus the degree of peak polarization is observed to be lower than that reported by Levrat *et al.* [18]. The rate of the decrease of the linear polarization beyond the peak depends on the ratio of the nonlinear coefficient α_1 and the linear polarization splitting Ω .

3.7 Conclusions

In conclusion, the chapter reports on detailed steady state measurements of the linear polarization degree of electroluminescence in several diode polariton lasers. The linear polarization build-up is caused by the pinning effect that arises due to the energy splitting of polariton modes polarized along different crystal axes. In addition to the injection dependent linear polarization, the polarization resolved output light-current characteristics have also been studied. A maximum degree of linear polarization of ~ 22 % is observed. The experimental results have been theoretically analyzed by modeling the kinetics of the system with a system of coupled stochastic differential equations. The agreement of theory and experiment is very good, in general. In one of the devices, a surprising and significant lowering of the laser threshold is observed for the polarization resolved output, compared to that for the unresolved output. This effect is believed to be induced by the spatial inhomogeneity in the microcavity due to defects or photonic disorder.

Chapter IV

Spin Injection in GaN-Based Electronic Devices and Light Sources

4.1 Introduction

GaN is deemed to be suitable for room temperature spintronics applications owing to its intrinsically weak spin-orbit coupling (Δ_{SOC} ~ 17 meV). Values of electron spin relaxation lifetimes in bulk n-doped wurtzite GaN, ranging from 35 to 50 ps, have been reported from room temperature time-resolved Kerr-rotation and time-resolved Faraday rotation spectroscopy measurements [25, 26]. Spin diffusion parameters in relatively defect-free single wurtzite GaN nanowires (NWs) have also been determined from four-terminal Hanle spin precession measurements [27], which yielded a maximum spin lifetime ~ 100 ps and a spin diffusion length of ~ 260 nm at room temperature. The following measurements were carried out to ascertain the basic spintronic characteristics of bulk GaN injected with a spin-polarized current via FeCo/MgO tunnel barrier contacts. An electron spin injection efficiency of ~ 7.9 % and electron spin diffusion length of ~ 176 nm were determined for the spin injector contact, and bulk GaN, respectively.

4.2 Four-Terminal Non-Local Magnetoresistance Effect

In the present study, measurements have been made on bulk GaN lateral spin valves with FeCo/MgO ferromagnetic contacts. The spin diffusion length and spin lifetime are independently estimated from channel-length dependent non-local magnetoresistance (MR) measurements and four-terminal Hanle spin precession measurements respectively.

The lateral ferromagnet-semiconductor spin valves were fabricated upon n (Si)-doped wurtzite c-plane GaN (0001) grown by metal-organic chemical vapor deposition (MOCVD). Several ferromagnet/semiconductor/ferromagnet (FM/SC/FM) lateral spin valves were fabricated with varying channel lengths ranging from 250 nm to 450 nm. The channel width in all the spin valves is 400 μm. A schematic of the device, along with the four terminal non-local MR measurement scheme, is illustrated in Fig. 4.1.

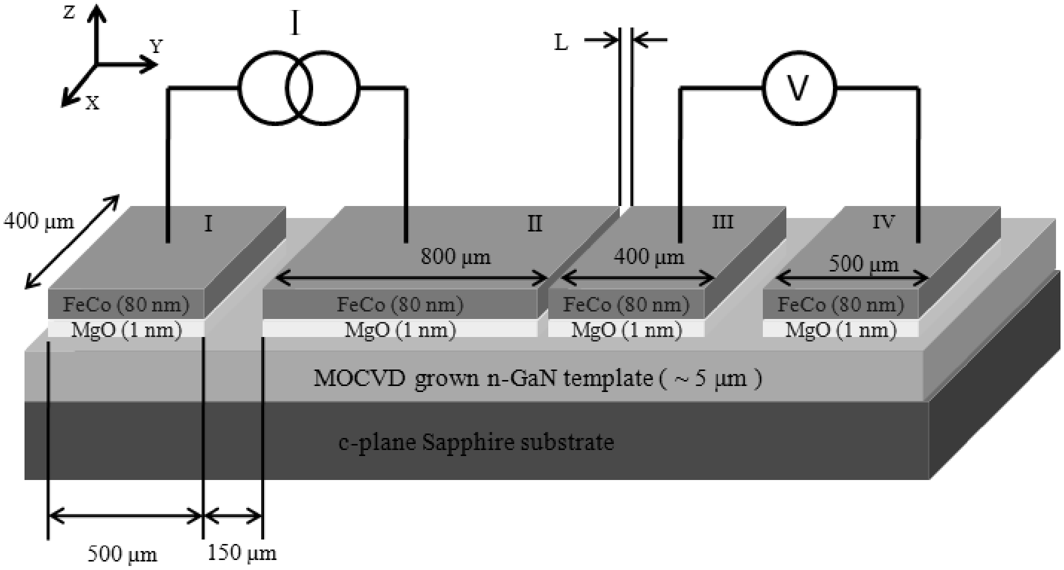

Figure 4.1. Schematic illustration of the four-terminal non-local measurement scheme (not drawn to scale).

Non-local magnetoresistance and spin accumulation measurements were made on the GaN-based devices. The measurements were performed, using standard four-probe ac lock-in techniques, at 300 K in a magneto-optical cryostat. Samples of varying channel lengths were mounted between the poles of an electromagnet such that the applied external magnetizing field is aligned to the plane of spin transport. Results from non-local measurements performed at T=300 K for the spin valve with channel length L=250 nm are shown in Fig. 4.2 (a). The magnetoresistance, defined as, $MR = \frac{R(\uparrow\downarrow) - R(\uparrow\uparrow)}{R(\uparrow\uparrow)}$ peaks at |H| ~ 292 Oe in both directions of the magnetic field. A peak magnetoresistance of 0.514 % is recorded for L=250 nm at an applied bias of 1V. Figure 4.2 (b) shows a plot of the peak magnetoresistance as a function of L. From the value of peak magnetoresistance for L → 0, a maximum spin polarization ($\Pi_s = \frac{\beta - 1}{\beta + 1}$) of 7.9 % at the injector ferromagnetic contact is derived. The value of the peak magnetoresistance as L → 0, can be expressed as $MR = \frac{R_{\uparrow\downarrow} - R_{\uparrow\uparrow}}{R_{\uparrow\uparrow}} = \frac{(\beta - 1)^2}{4\beta}$. Here, $\beta = \frac{R_{\downarrow TB}}{R_{\uparrow TB}}$ is defined as the spin selectivity of the tunnel barrier. Analysis of the channel-length dependent data yields a spin-flip lifetime ~ 23 ps and a corresponding spin diffusion length of ~ 140 nm at 300 K.

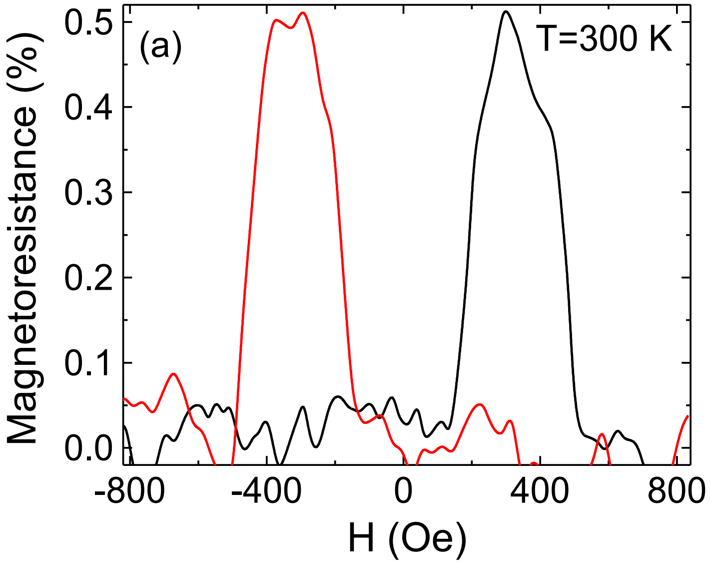

Figure 4.2. (a) Magnetoresistance as a function of applied magnetic field for a 250-nm channel length lateral spin valve measured at 300 K. The black and red lines indicate increasing and decreasing magnetic field sweeps, respectively.

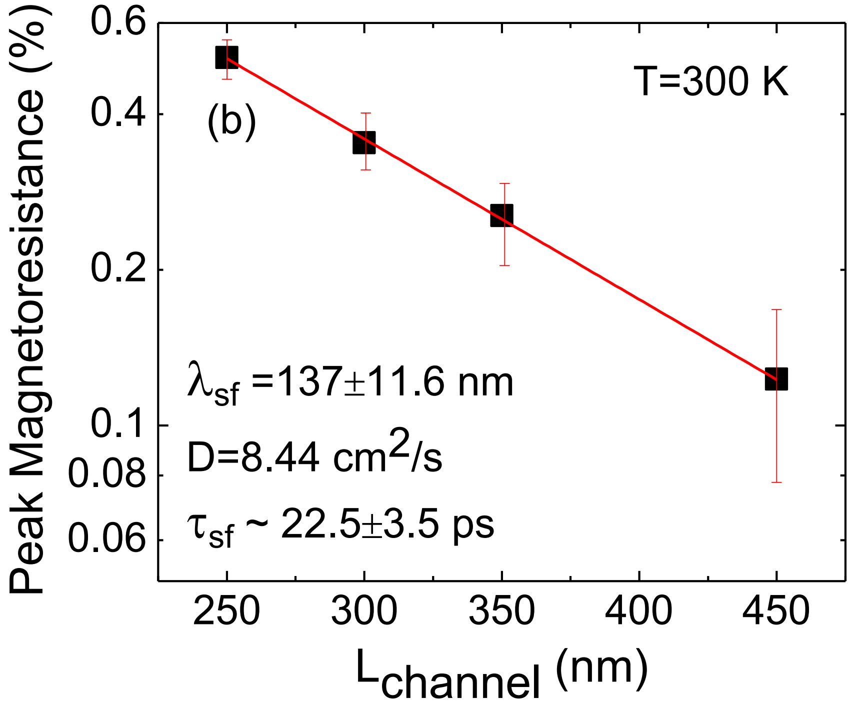

Figure 4.2. (b) Peak magnetoresistance as a function of channel length measured at 300 K.

4.3 Detection of Hanle Spin Precession at Room Temperature

To conclusively establish electrical spin injection into the channel, four-terminal Hanle spin precession measurements were performed with the same lateral spin valves at room temperature. A gradual change in the measured non-local voltage is observed due to Larmor precession of the diffusing electron spins and consequent spin dephasing in an applied transverse magnetic field B_z. The Larmor frequency $\omega_L = g\mu_B B_z / \hbar$, where g is the Landé g-factor, μ_B is the Bohr magneton, and $\hbar$ is reduced Plank's constant. The data shown in Fig. 4.3 is a clear demonstration of the Hanle effect, where the top and bottom branches correspond to parallel and antiparallel magnetization of contacts II and III. The spin-flip lifetime, τ_{sf}, was deduced by analyzing the data for a channel length of L=250 nm (solid lines in Fig. 4.3) with the following equation:

$$\frac{V_{NL}}{I_{inject}} \propto \pm \iiint_{y_2, y_1, t} \frac{1}{\sqrt{4\pi Dt}} \exp\left[-\frac{\left(y_2 - y_1 - v_d t\right)^2}{4Dt}\right] \cos(\omega_L t) \exp\left[-\frac{t}{\tau_{sf}}\right] dt dy_1 dy_2 \tag{1}$$

where D is the electron diffusion constant, τ_{sf} is the spin-flip lifetime, v_d is the drift velocity which is assumed to be zero for electron spin transport mediated entirely by diffusion [62], and + (-) signs indicate parallel (antiparallel) magnetization state of the FM electrodes. From Hall mobility measurements on a bulk GaN-on-sapphire sample, one obtains a majority carrier mobility $\mu \sim 261$ cm^2/V-s and a majority carrier concentration n ~ $1\text{x}10^{18}$ cm^{-3}. From the Einstein's relation $\frac{D}{\mu} = \frac{\frac{1}{q}\int_0^\infty S(E)F(E)dE}{\int_0^\infty S(E)\frac{\partial F}{\partial E}dE}$, where *S* is the density of states, *F* is Fermi-Dirac distribution, *q* is electronic charge and *D* is the diffusion constant, a value of D=8.44 cm^2/s is derived. Using a g-factor of 1.94 for GaN [26], a value of spin-flip lifetime $\tau_{sf} \approx 37$ ps is obtained, which translates to a spin diffusion length of $\lambda_{sf} \approx 176$ nm at T=300 K using the relation $\lambda_{sf} = (D\ \tau_{sf})^{1/2}$. This value is in good agreement with the spin diffusion length derived from the non-local magnetoresistance measurements, within the limits of errors incurred during measurements and analysis of data.

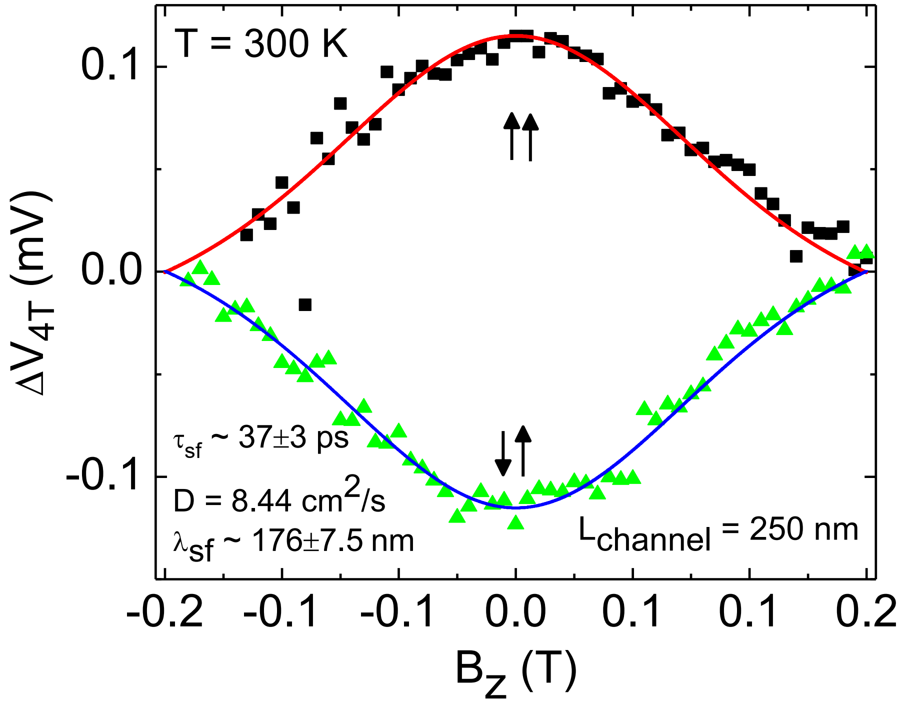

Figure 4.3. Four-terminal Hanle spin precession data measured for a 250-nm channel length lateral spin valve at 300 K.

4.4 Effects on Defects and Dislocations on Electron Spin Relaxation

A value of ~ 37 ps for the spin relaxation time in GaN is in excellent agreement with previously reported values obtained from time-resolved Faraday rotation and time-resolved Kerr rotation measurements performed on GaN samples having similar n-doping levels. The latter results were explained by invoking the D'yakonov-Perel spin scattering mechanism. A common feature in the samples used in the previous studies and the present one is that the defect density in the active region is ~ 10^8 cm^{-2}. While differences in doping levels have been accounted for, the large defect density has not been taken into account. It may be remembered that a significantly larger value of τ_{spin} ~ 100 ps was measured at room temperature by Hanle spin precession and non-local spin transport measurements on a single GaN nanowire in which the density of defects is 10^2–10^3 cm^{-2}. Further, although the spin-orbit coupling in bulk GaN is appreciably weaker than that of GaAs (the valence-band splitting in GaN is 20 meV whereas in GaAs it is 340 meV), it is observed that room temperature spin-flip lifetimes in bulk GaN (40 ps) is smaller than those of bulk GaAs (200 ps) in which the dislocation density is almost negligible. It is therefore apparent that defects in GaN do play a significant role in determining spin transport characteristics. Spin-polarized electrons trapped in defects encounter further precessional dephasing owing to local fields, such as the hyperfine field, due to the stronger interaction of the trapped and consequently confined electrons with the nuclear system. Electron spin dephasing mediated by hyperfine interaction with the nuclear spin bath is an important effect for confined or localized electrons which is true for these electrons trapped in the defects. It is probable that another major dephasing channel is the strong exchange interaction between electrons trapped in adjacent defect states. It has been recently demonstrated experimentally and theoretically described how inelastic scattering between conduction and shallow donor impurity-bound electrons in unintentionally doped n-type Si(100) leads to dephasing of both spins by mutual spin exchange [63]. It has also been observed in bulk n-type GaN samples wherein the n-doping level is approximately identical (~10^{18} cm^{-3}) that the spin lifetime decreases significantly with the increase in dislocation density, which may be potentially attributed to larger Elliott-Yafet spin scattering rates in these materials with larger defect densities. Detailed analysis of the data with this scattering, including spin dephasing brought about by the defects, in these wurtzite crystals is beyond the scope of this chapter.

4.5 GaN-based Spin-polarized Light-Emitting Diodes

A more direct way of detecting successful electron spin injection and transport in a direct band-gap semiconductor is by using a spin-polarized light-emitting diode geometry. The light-emitting diode acts as a detector of the steady-state electron spin polarization in the active region of the device. From measurements of the degree of the output circular polarization and taking into account the appropriate magnetization and light emission geometries, a value of the degree of the electron spin polarization can be inferred. For example, a value of steady-state electron spin polarization of ~ 18 % was ascertained from the observed degree of output circular polarization of ~ 6 %. It should be noted that these values are highly dependent on the doping density, defect density, bias and the local lattice temperature. Thus, for example, the value of ~ 18 % is less than the value of ~ 8 %, which was obtained from non-local magnetoresistance measurements. There could be multiple reasons for the same. The principal ones include the fact that the spin-valve data are obtained from measurements made on n-type GaN-on-sapphire epitaxial templates. These have larger doping as well as defect (mainly, charged threading dislocations) densities than the active GaN layers of the spin-LEDs. This was the last examination, which was conducted to ascertain the feasibility of GaN for room-temperature spin-optronics. Room temperature circularly polarized electroluminescence is observed from bulk GaN-based double-heterostructure edge-emitting light emitting diodes operated with continuous-wave spin-polarized electrical injection. A schematic of the diode is shown in Fig. 4.4. The measured in-plane magnetizing field-dependent output circular polarization in the quasi-Voigt geometry is coincident with the hysteresis characteristics of the spin-injector confirming electron spin injection in remanence from the n-type FeCo/MgO tunnel spin contacts. A peak output circular polarization of ~ 6 ± 1 % is measured at 300 K. The active region of these devices is bulk GaN and thus the generation of edge-emitting circularly polarized electroluminescence originating from spontaneous radiative recombination of spin-polarized carriers is quantum-mechanically allowed.

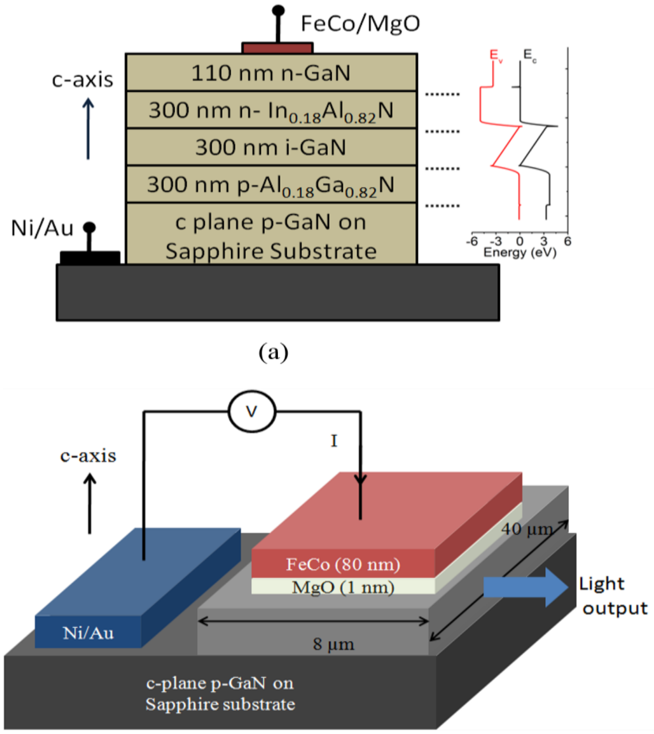

(a)

(b)

Figure 4.4. (a) Schematic representation of the double heterostructure GaN-based spin-polarized light-emitting diode (LED) (not drawn to scale). A representative energy band-diagram of the device heterostructure is shown alongside; (b) schematic representation of the edge emission geometry of the spin-polarized LED.

4.5.1 Introduction

A low-power stable electrically controlled circularly polarized visible light source is useful for a wide range of applications including preparation of chiral compounds and chiro-optical spectroscopy of biochemically active molecules, non-invasive medical diagnosis of cancerous tissues and turbid tissue-like scattering media, optical data storage and processing, photonic technologies such as color-image projection and stereoscopic displays, reconfigurable optical interconnects and ultrafast optical switches, cryptographic optical communications and telecommunications with enhanced bandwidth, and the probing of magnetic properties of solids in the visible range. A convenient technique of obtaining such a circularly polarized light source is by the spontaneous radiative recombination of spin-polarized carriers in a light emitting diode (LED) or laser whose operation stems from optical selection rules which govern the conversion between the injected carrier spin polarization and the output photon circular polarization. The bulk of the reports on spin LEDs is in the near-infrared wavelength range, with GaAs-based devices [64-71]. More recently, results from GaN-based visible spin LEDs have also been reported [72-75]. An edge-emitting spin LED combines the above-mentioned benefits of circularly polarized light source and the natural advantages of edge-emitting devices over conventional surface-emitting geometries for practical applications such as fiber-optic communications, which include more efficient coupling of the radiated beam into fibers. Further, an edge-emitting spin-polarized electroluminescent device allows the use of the large in-plane remanent magnetization of a convenient spin injector [76, 77] and of very short transport distance of the spin polarized injected carriers. Circularly polarized edge-emitting electroluminescence originating from electron spin injection has been observed in both zinc-blende (GaAs-based) [70] and wurtzite (GaN-based) III-V semiconductors [74] at low temperatures. In this section, the room temperature characteristics of edge-emitting bulk GaN-based spin-polarized LEDs fabricated with n-type ferromagnetic FeCo/MgO spin contacts and operated with the in-plane remanent magnetization of the contact, are reported.

4.5.2 Optical Selection Rules

The establishment of steady-state electron, or hole, spin coherence in a semiconductor is accomplished mainly by electrical spin injection or by excitation with circularly polarized light. Generation of circularly-polarized electroluminescence from the spontaneous radiative recombination of a resultant spin population asymmetry of the injected carriers, and creation of a spin population imbalance through excitation by circularly-polarized light are mutually complementary physical processes. When the electric field polarization of an optical excitation incident on bulk wurtzite GaN is parallel (orthogonal) to the c-axis, the ratio of the relative oscillator strengths for the optical transitions from the valence bands A (Γ_9 symmetry), B (Γ_7 symmetry) and C (Γ_7 symmetry) to the conduction band is 0: 0.0484: 0.9516 (1: 0.9516: 0.0484). These oscillator strengths are deduced from the expansion coefficients of the eigenvectors of the valence-band states. One obtains the value of ‘a’, the coupling parameter for wave functions of Γ_7 valence-band states [78], for bulk wurtzite GaN to be ~ 0.22, assuming the valence-band parameters Δ_1, Δ_2 and Δ_3 to be ~ 10.2, 6 and 6 meV respectively [78, 79], from which the above-mentioned transition strengths are calculated.

In the case of surface-emitting geometry, where the electric field polarization is orthogonal to the c-axis, a steady-state electron spin polarization of 100% in the light-emitting active region will generate a resultant output circular polarization of ~ 2.5 %, assuming no contribution from the crystal-field split-off valence band C. In the case of an edge-emitting GaN-based LED, which has been characterized in our present study, where photon propagation is in a direction orthogonal to the structural growth axis (c-axis), the electric field amplitude of the circularly-polarized light, on an average, will have equal contributions from electric fields oriented along and orthogonal to the c-axis. Therefore, the relative oscillator strengths for the fundamental optical transitions from valence bands A, B and C to the conduction band (which will generate the A-, B- and C- free excitons) are 0.5: 0.5: 0.5 as shown in Fig. 4.5. Further, at 300 K the three different GaN resonant excitonic transitions spectrally broaden and merge to form a single absorption or emission line. Assuming the valence bands are equally populated, which is usually the case in room-temperature electrical spin injection experiments, one can deduce the following relation between the steady-state optical (Π_{CP}) and electron spin polarizations (Π_{inj}), in a way similar to that used in zinc-blende crystals:

$$\Pi_{CP} = \frac{\left(I(\sigma^+)-I(\sigma^-)\right)}{\left(I(\sigma^+)+I(\sigma^-)\right)} = \frac{(n_\downarrow+0.5n_\uparrow)-(n_\uparrow+0.5n_\downarrow)}{(n_\downarrow+0.5n_\uparrow)+(n_\uparrow+0.5n_\downarrow)} = \frac{0.33(n_\downarrow-n_\uparrow)}{(n_\downarrow+n_\uparrow)} = -0.33\ \Pi_{inj} \qquad (2)$$

Here $I(\sigma^+)$ and $I(\sigma^-)$ are the intensities of the σ^+ and σ^-- polarized light, respectively, and $n_\downarrow$ and $n_\uparrow$ are the densities of spin-down and spin-up conduction-band electrons, respectively. Thus, ideally a steady-state injected electron spin polarization of 100 % should give rise to a steady-state output circular polarization of ~ 33 %. From Fig. 4.5, it can be observed that the transitions induced between valence bands B and C, the light-hole and the crystal-field split-off bands, respectively, and the conduction band will populate the same spin orientation of electrons in the conduction band which will be opposite to that generated by transitions from the valence band A.

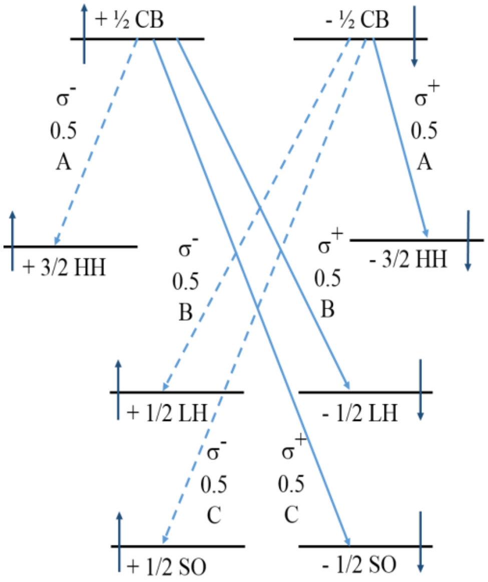

Figure 4.5. Electric dipole allowed radiative interband transitions and corresponding optical polarizations for electroluminescence propagating orthogonal to c-axis of bulk wurtzite GaN. The numbers and the letters adjacent to the arrows indicate the relative transition strengths and the nature of the transitions respectively.

4.5.3 Device Processing and Characterization

The device heterostructure, schematically depicted in Fig. 4.4 (a), of the edge-emitting spin LED (Fig. 4.4 (b)) was grown by plasma-assisted molecular beam epitaxy on wurtzite c-plane p-type (Mg-doped) epitaxial GaN (0001)-on-sapphire template. A representative energy band-diagram of the device heterostructure is shown alongside Fig. 4.4 (a). The n-type $In_{0.18}Al_{0.82}N$ layer serves the dual function of an optical cladding as well as a carrier confinement layer. The doping levels of the n-type $In_{0.18}Al_{0.82}N$ and p-type $Al_{0.18}Ga_{0.82}N$ doped layers are ~ 5 X 10^{18} and ~ 6 X 10^{17} cm^{-3}, respectively. The active region of these devices is bulk GaN and thus the generation of edge-emitting circularly polarized electroluminescence originating from spontaneous radiative recombination of spin-polarized carriers is quantum-mechanically allowed [70]. The devices have been characterized in the quasi-Voigt geometry, wherein the direction of the externally applied magnetizing field and consequently the spin angular momentum quantization axis, the components of the total angular momenta of the spin-polarized electrons and the unpolarized holes, and the wave-vector of the emitted light, are all aligned in the same direction. The latter is oriented along the $[1\ 1\ \overline{2}\ 0]$ crystallographic axis (orthogonal to the a-plane) and thus is orthogonal to the growth direction (c-axis). The thickness of the GaN-based active material in our double-heterostructure LEDs is ~ 300 nm which is ~ 100 times the typical value of the excitonic Bohr radius at room temperature and thus quantum confinment effects should not intervene. Device fabrication is initiated by selective deposition of Ni-Au p-contact, followed by definition of the 8 μm x 40 μm active region by standard UV photolithography and high density plasma etching down to the substrate. Following this, 1 nm MgO tunnel barrier and 80 nm FeCo spin injector are deposited by electron beam evaporation to form the n-type ferromagnetic tunnel contact (Fig. 4.4 (b)). The surface of the sample was etched with buffered

HF solution before deposition of the spin injector materials. The deposition parameters of the electron beam evaporator were optimized to accomplish an electron beam evaporated film thickness of 1 nm of MgO, which was measured indirectly by variable-angle spectroscopic ellipsometry having the capability of resolving sub-nanometer thicknesses.

The spectrally-resolved electroluminescence intensities at the free-excitonic emission wavelength was measured as a function of injection and are shown in Fig. 4.6. The slope of the light-current characteristics is ~ 1.5. The diodes are characterized by a typical turn-on voltage of ~ 2.5 V and the leakage current of the diode at ~ − 11 μV is less than 10 nA. Four-terminal Hanle spin precession measurements have been made at room temperature on non-local GaN-based lateral spin valves formed with identical n-type FeCo/MgO ferromagnetic tunnel contacts, wherein an external magnetic field was applied along the c-axis, as described in a previous section of this chapter. Electron spin relaxation length and spin-flip lifetime of ~ 176 nm and ~ 37 ps,

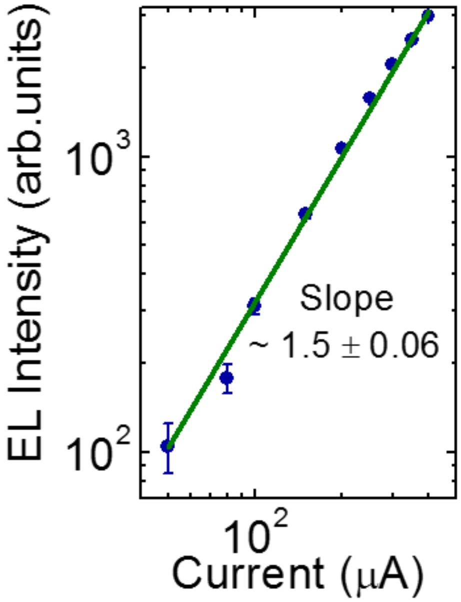

Figure 4.6 Light-current characteristics of the spin-polarized LED. The solid line shows a power-law fit to the measured data.

respectively, were derived from analysis of the measured data. In the edge-emitting spin-polarized LEDs being characterized here, the injected spin-polarized electrons have to effectively traverse a distance of ~ 410 nm before reaching the recombination volume.

4.5.4 Circular Polarization Measurements

The optical polarization state of the output electroluminescence was measured employing Stokes polarimetry from which the circular polarization-resolved electroluminescence intensities at the free excitonic emission wavelength are obtained. The output electroluminescence was transmitted to an UV quarter-wave (λ/4) plate whose fast axis was appropriately oriented to the transmission axis of the following Glan-Thompson linear analyzer, to spectrally resolve the left- and right-handed circular polarization components. The circular polarization-resolved luminescence was then spectrally dispersed by a 0.75 m imaging monochromator having a spectral resolution of ~ 0.03 nm at ~ 435.8 nm and detected by a photomultiplier tube.

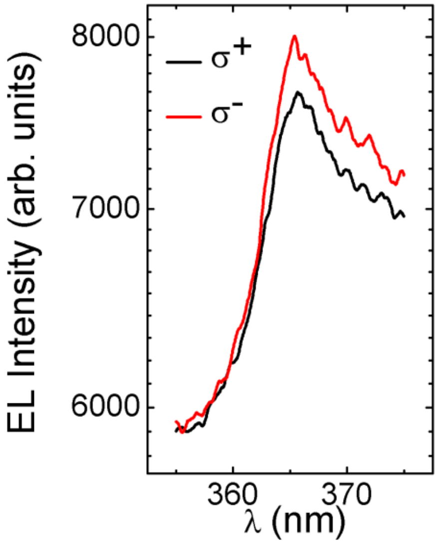

Figure 4.7. Circular-polarization resolved electroluminescence spectra recorded at an injected current of ~ 1 mA after in-plane magnetization of the ferromagnetic contacts with a magnetizing field, H, of ~ - 1 kOe. The spectra have been smoothed using weighted adjacent-averaging filtering.

The polarization resolved electroluminescence spectra measured at an injected current of ~ 1 mA, after magnetizing the contacts with an in-plane field of ~ - 1 kOe, are shown in Fig. 4.7. The asymmetry in the lineshape is probably due to an acceptor-bound excitonic transition centered at ~ 380 nm, which is characteristic of devices grown on p-type (Mg-doped) epitaxial GaN (0001)-on-sapphire templates. The spectra have been recorded over the wavelength range of ~ 355 nm to ~ 375 nm since our objective was the observation of excitonic feature(s) centered at ~ 365.5 nm. A circular polarization of ~ - 2.5 % is observed at the excitonic emission peak. As shown in Fig. 4.8, the degree of circular polarization of the edge-emitting LEDs, biased at a constant injected current strength of ~ 640 µA, is seen to closely follow the in-plane magnetization of an 80 nm FeCo layer, which demonstrates that the measured polarization originates from spin injection by the ferromagnetic FeCo/MgO contact. The degree of circular polarization saturates at ~ 5 % for applied magnetic fields greater than the in-plane saturation field for FeCo. The output circular polarization data, as shown in Fig. 4.8, are obtained from the polarization-resolved emission intensities recorded by a photomultiplier tube after spectrally filtering the excitonic feature(s) centered at ~ 365.5 nm through an imaging monochromator. The degree of circular polarization above the saturation H field, with an injection of ~ 1mA, is less than that with ~ 640 µA because the polarization decreases with increasing injection due to the reduced efficiency of the tunneling process for the spin-polarized carriers at higher biases [69, 80]. A peak value of ~ 11 % for the circular polarization is expected from the electron spin injection efficiency for the FeCo/MgO contact, for which a value of ~ 32 % has been reported at room temperature [69]. The lower values observed is probably due to efficient spin relaxation of the spin-polarized electrons during their transport to the active region. Spin relaxation in GaN is usually interpreted as being mediated by the D’yakonov-Perel spin scattering mechanism.

However, it has also been observed that the spin lifetime decreases significantly with the increase in dislocation density, which may be potentially attributed to larger Elliott-Yafet spin scattering rates in wurtzite GaN crystals with larger defect densities. The defect density, in these samples grown on GaN-on-sapphire epitaxial templates, is ~ 6 X 10^8 cm^{-2}. The excitation dependence of the output circular polarization has also been studied. It may be observed that there is a reduction in the value of the output polarization with increasing injection. The data are shown in Fig. 4.9. Similar behavior has also been observed in GaAs-based incoherent

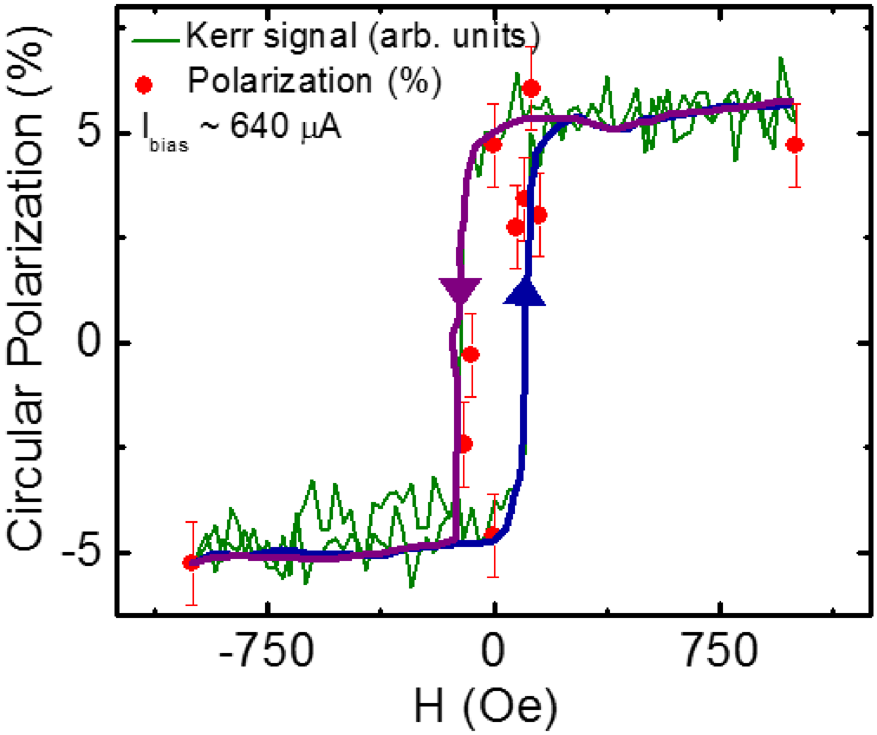

Figure 4.8. Degree of circular polarization of the spin-polarized LED measured as a function of the in-plane magnetizing field. The normalized in-plane magnetization curve determined from ferromagnetic hysteresis measurements made on electron beam evaporated bulk 80 nm thick FeCo film is shown for comparison. The solid lines are guides to the eye representing increasing and decreasing magnetic field sweeps respectively.

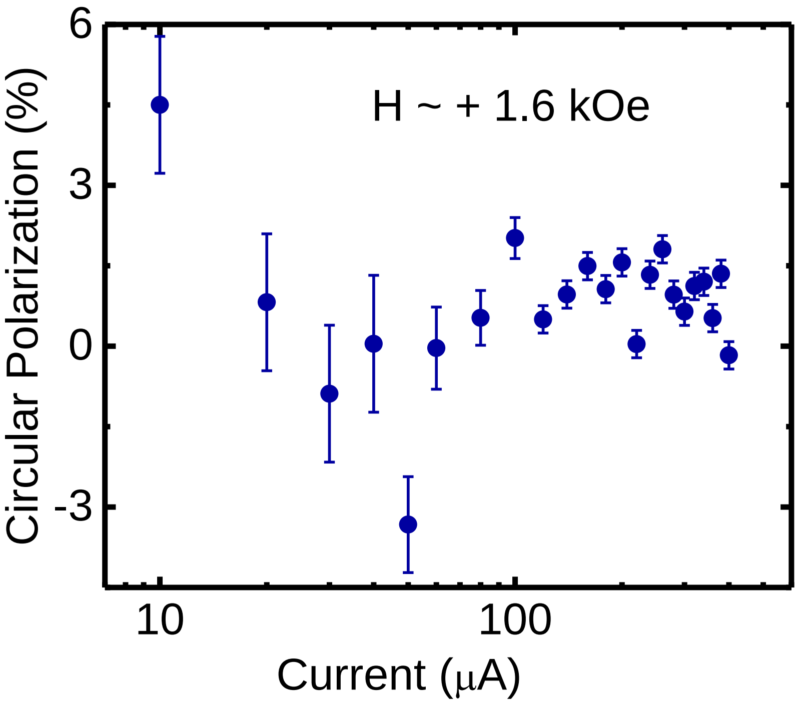

Figure 4.9. Degree of circular polarization measured as a function of injected current after magnetizing the ferromagnetic contacts with magnetizing field, *H*, of ~ + 1.6 kOe.

electroluminescent devices having similar n-type CoFe/MgO contacts. A similar excitation dependence has also been reported in optical experiments and was attributed to spin relaxation through the D'yakonov-Perel (DP) relaxation mechanism before the photogenerated electrons reached the device active region [81, 82]. In semiconductors lacking inversion symmetry such as GaAs and GaN, DP spin relaxation occurs due to spin precession about an effective magnetic field whose orientation and magnitude depends on the electron momentum. Larger values of electron momenta, which are gained at higher values of biases, result in a bigger effective magnetic field, which brings about faster and more effective spin relaxation of the diffusing electrons [69]. It is also possible that the decrease in the steady-state photon polarization decreases with increasing injection and thus with increasing tunnel-junction bias is due to the reduced efficiency of the tunneling process for the spin-polarized carriers at higher biases [80].

4.5.5 Enhancement of the Total Output Electroluminescence

The unresolved output electroluminescence spectra of the spin-polarized LEDs were also measured before and after in-plane magnetization of the n-type ferromagnetic FeCo/MgO tunnel contacts as a function of injection current under identical conditions. The spectra recorded for an injection current of ~ 9 mA before and after in-plane magnetization (H ~ 2.35 kOe) of the n-type ferromagnetic tunnel contacts are shown in Fig. 4.10 (a). The recorded spectra were spectrally integrated across the entire wavelength range of the spectral acquisitions from 328.68 nm to 418.68 nm and the integrated intensity is a measure of the total light output from these LEDs in arbitrary units. The variation of the light output with injection current before and after in-plane magnetization of the tunnel contacts is illustrated in Fig. 4.10 (b). The average slopes of the light-current characteristics are ~ 0.83 and ~ 0.77 before and after in-plane magnetization, respectively. In both cases, the slope of the light-current characteristics slightly increases at an injected current of ~ 2 mA, which is probably related to increased acceptor atom activation and consequent enhanced p-type conductivity due to field-induced ionization effects [83].

It has been observed that any injection, after in-plane magnetization of the n-type ferromagnetic contacts, there is an enhancement of the output electroluminescence intensity. This is similar to the observations made by Kim *et. al.* [84] who reported an increase of the optical output power of InGaN/GaN multiple quantum-well (MQW) flip-chip LEDs with a FeCo ferromagnetic layer deposited on a p-ohmic reflector after in-plane magnetization. The observed enhancement was attributed to increase in the internal quantum efficiency in the MQWs of the LEDs due to a gradient of the magnetic field from the FeCo ferromagnetic layer, which enhanced the transport of carriers towards the InGaN MQWs. In all probability, a similar mechanism is in effect in these bulk GaN-based LEDs, wherein the remanent magnetization of the spin contacts induces a magnetic field gradient and accelerates the drift of the spin-polarized carriers across the $In_{0.18}Al_{0.82}N$ layer, thus reducing the probability of the spin-polarized carriers from getting trapped in non-radiative recombination centers in the cladding layer, towards the light-emitting heterojunction. The percentage increase of the total light output upon magnetization as a function of injection current is plotted in Fig. 4.10(c). A maximum enhancement of ~ 91 % is observed and the enhancement decreases with injection. The saturation of the enhancement is probably related to the characteristic saturation of integrated electroluminescence intensities of the excitonic resonances with increasing injection due to a combination of excitonic luminescence quenching, saturation of the excitonic oscillator strength, heating effects and increased dominance of non-radiative recombination channels.

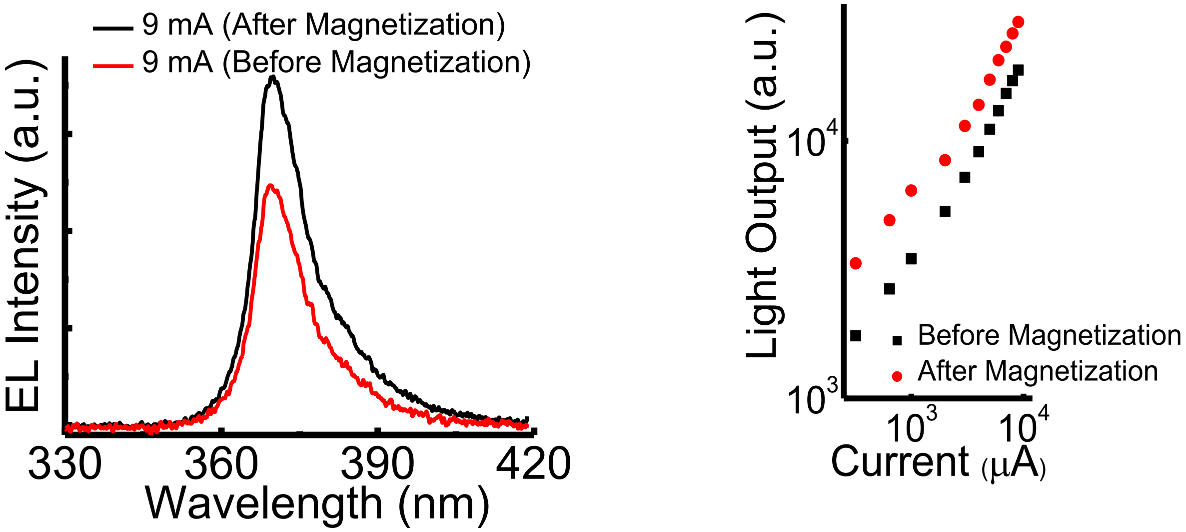

(a)

(b)

Figure 4.10 (a) Unresolved smoothed electroluminescence spectra recorded at an injected current strength of ~ 9 mA before and after magnetization of the ferromagnetic contacts; (b) light-current characteristics of the spin-polarized LED measured before and after magnetization of the ferromagnetic contacts.

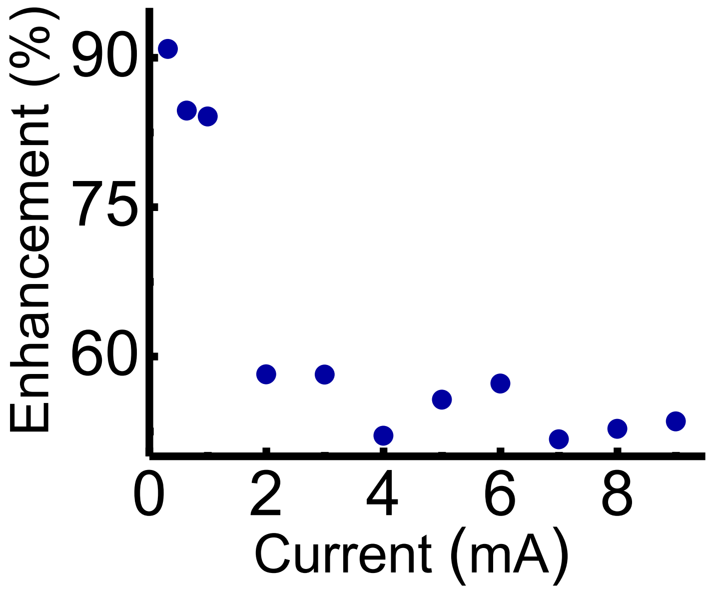

(c)

Figure 4.10 (c) Percentage enhancement of the light output as a function of injection as a result of magnetization of contacts.

4.6. Summary

In conclusion, electrical spin injection, transport, and detection have been performed in bulk GaN-based lateral spin-valves with FeCo/MgO tunnel contacts at room temperature. Diffusive electronic spin transport in GaN has been verified from channel length-dependent non-local MR measurements and four-terminal Hanle spin precession measurements performed in the same devices. The spin diffusion length and spin lifetime obtained from both measurements in good agreement. Electrical injection and optical detection of electron spin coherence in double-heterostructure GaN-based edge-emitting light-emitting diodes equipped with FeCo/MgO tunnel contacts, have also been demonstrated at room temperature. A maximum degree of circular polarization of ~ 6 % is observed in the output electroluminescence from the spin-LEDs.

Chapter V

Room-Temperature Spin Polariton Diode Laser

5.1 Introduction

The output of a microcavity coherent light source is generally linearly polarized in the emitter-cavity photon strong coupling regime in the absence of pinning caused by photonic structural disorders [45, 85-86]. However, it has been experimentally demonstrated that the orientation of this polarization is stochastic and hence the polarization cannot be experimentally recorded in the steady state [47, 49]. Linear polarization can be observed in the steady state output only by pinning along a preferred crystallographic axis and the degree of polarization decreases at high pumping levels due to the depinning effect caused by polariton-polariton repulsive interactions and self-induced Larmor precession of the Stokes vector of the condensate [11]. These trends in the linear polarization have been observed in polariton lasers pumped optically and electrically. In the case of optical excitation, it is also possible to obtain a circularly polarized output above threshold and this behavior has been verified experimentally in the steady state at cryogenic temperatures [5, 87-89]. The degree of circular polarization is determined by the interplay of polariton thermalization by scattering (polariton-phonon, polariton-electron and polariton-polariton) and polariton pseudospin precession in the effective magnetic field due to the TE-TM splitting [85, 90]. Circular polarization has not been observed in the output of an electrically injected polariton laser since carriers are injected with no net polarization [16]. The output can be circularly polarized due to the interplay of spin-dependent polariton-polariton interactions and stimulated relaxation of exciton polaritons at high injection densities where the depinning of linear polarization is observed, but this circular polarization is small, random and largely uncontrolled. On the other hand, it is possible to obtain a controlled and variable circularly polarized output by electrically injecting spin polarized carriers with a suitable ferromagnetic contact or a diluted magnetic semiconductor acting as a spin injector, as demonstrated with conventional photon lasers designed as vertical cavity surface-emitting lasers (VCSELs) and light-emitting diodes (LEDs).

5.2 The Spin Polariton Laser Device

Several identical electrically pumped bulk GaN-based microcavity polariton lasers fabricated from a single epitaxially grown heterostructure sample, as schematically shown in Fig. 5.1, have been characterized.

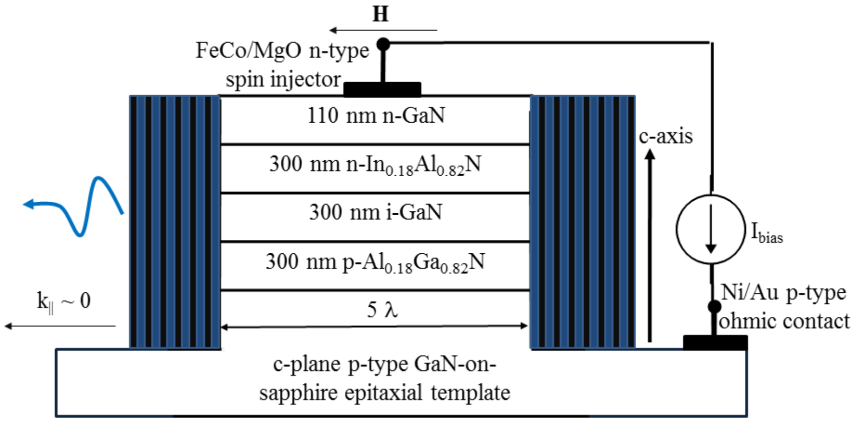

Figure 5.1. Schematic representation of the spin-polarized double heterostructure GaN- based microcavity diode (not drawn to scale) in the quasi-Voigt measurement geometry.

The device fabrication is described as follows. The device heterostructure, schematically depicted in Fig. 5.1, of the edge-emitting spin-polarized microcavity exciton-polariton laser diode, is grown by plasma-assisted molecular beam epitaxy (PAMBE) on wurtzite c-plane p-type (Mg-doped) ~ 5 μm thick hydride vapor-phase epitaxial (HVPE) GaN (0001)-on-sapphire substrate. The active region of the microcavity diode consists of 300 nm thick nominally undoped GaN. The 300-nm thick n-type (Si-doped) $In_{0.18}Al_{0.82}N$ layer is lattice matched to GaN and therefore allows the growth of high quality epitaxial layers. Moreover, $In_{0.18}Al_{0.82}N$ has a high refractive index contrast with GaN, which enhances optical confinement. The p-type $Al_{0.18}Ga_{0.82}N$ layer acts as an electron blocking layer because of its higher bandgap and provides photon confinement because of its lower refractive index than GaN. Therefore, the $In_{0.18}Al_{0.82}N$ and $Al_{0.18}Ga_{0.82}N$ layers of this heterostructure form the lower and upper cladding respectively for bulk-GaN waveguide layer. Device fabrication is initiated by selective deposition of 1 nm thick MgO tunnel barrier and 80 nm thick ferromagnetic FeCo alloy using electron beam evaporation technique to form the n-type ferromagnetic spin injector contacts. The salient deposition parameters of the electron beam evaporator were optimized to obtain the desired film thicknesses, which were measured indirectly employing variable-angle spectroscopic ellipsometry having capability of resolving sub-nm thicknesses. Next, a 5μm x 40μm cavity region is defined by UV lithography, which is subsequently etched down to the substrate through the 300-nm thick p-type $Al_{0.18}Ga_{0.82}N$ layer using high density plasma etching. The p-type ohmic contact is formed by selective deposition of Ni/Au on the p-doped GaN layer by electron beam evaporation. This deposition step is followed by plasma enhanced chemical vapor deposition of 1 μm SiO_2, which is next patterned and etched to form the contact pads. This is followed by FeCo deposition onto the contact pads to form the n-type metal interconnect, which is used for electrical probing of the device.

The final dimensions of the cavity, 690 nm (5λ) X 40 μm, are patterned by focused ion beam (FIB) etching. A final step of FIB etching is performed at extremely low current levels to ensure optically flat surfaces at the two cavity ends along the longitudinal dimension (the axis of resonance) orthogonal to the structural growth axis of the cavity. Six and seven pairs of SiO_2/TiO_2 distributed Bragg reflector (DBR) mirrors are deposited on the two ends of the cavity (FIB etched facets) by electron beam evaporation to complete the definition of the 5λ bulk GaN-based optical resonant cavity. The current-voltage characteristics of all the seven devices characterized in the present study are shown in Fig. 5.2.

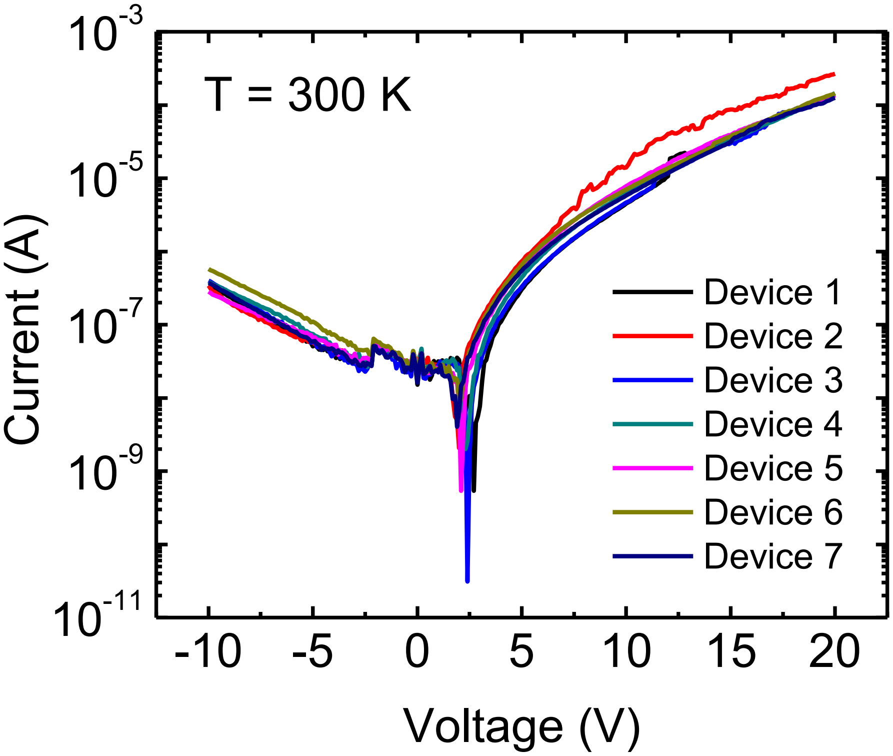

Figure 5.2. Measured current-voltage (I-V) characteristics of the seven devices characterized in the present study, plotted in a logarithmic-linear scale.

Two significant changes are incorporated in polariton laser diodes discussed in Chapter III, to accomplish successful electrical spin injection and transport. First, the regular n-type ohmic contact is replaced by n-type FeCo/MgO spin-injector contacts to introduce a net electron spin imbalance in the laser diode. The spin polarization of the injection current is dependent on the electron spin injection efficiency, for which a value of ~ 8 % has been reported for the FeCo/MgO contact at room temperature, in the previous chapter. Second, the diode heterostructure is grown on a p-type substrate so that the FeCo/MgO spin contact can be formed on the n-GaN layer on top. This reduces the transport length of the spin-polarized electrons to the active recombination region. The longitudinal spin transport length is ~ 400 nm in these devices, which is approximately twice that of the measured spin diffusion length at room temperature. Since the microcavity diodes have an edge-emitting geometry, wherein the direction of cavity resonance and current injection are in mutually orthogonal directions, a parasitic contribution to the output circular polarization arising from magnetic circular dichroism (MCD) is absent in our diode lasers. The in-plane magnetization of FeCo enables the use of an edge-emitting geometry, which utilizes the important advantages of ferromagnetic metals such as small coercive fields and high remanent magnetization. These are the characteristics which allow nonvolatile spin manipulation using modest magnetic fields and is thus a very practical consideration for device applications. Further, the use of a bulk (three-dimensional) active layer ensures that the heavy-hole exciton pseudo-spin can, in principle, be oriented along the direction of light propagation, as the electron spin and the heavy-hole angular momenta can both be aligned along the edge. The device cross-section being small, any difference in the measured characteristics between the devices is attributed to the number of defects in the active region. The defect density in the active region is ~ 6.1×10^{8} cm^{-2}. All measurements reported here have been done at room temperature.

The microcavity quality factor, Q, and the corresponding cavity mode lifetime, τ_{ph}, are determined to be ~ 3200 and ~ 0.6 ps, respectively, from microphotoluminescence measurements.

5.3 Strong Coupling Characteristics

To ascertain the exciton-photon strong-coupling characteristics, of the GaN-based devices, angle-resolved electroluminescence measurements were made at a continuous-wave (CW) injection close to the lower exciton-polariton (LP) condensation threshold (~ 0.95 J_{th}) using a digital readout angular mount having an angular precision of ~ 0.1^{o}. The spectra were recorded employing a combination of a 0.75 m Czerny-Turner imaging monochromator (with a spectral resolution of ~ 0.03 nm at ~ 435.8 nm) and a photomultiplier tube for a range of different emission angles. LP resonant peaks are observed below the exciton energy at all angles and the LP peaks tend to approach the exciton energy at higher angles (Fig. 5.3 (a)). The corresponding polariton dispersion characteristics, which are calculated using a 2 X 2 coupled harmonic oscillator model, are shown in Fig. 5.3 (b). From this analysis, one obtains values for the cavity-to-exciton detuning Δ and vacuum-field Rabi splitting Ω_{VRS} to be ~ – 7.5 meV and ~ 36.1 meV, respectively. These are calculated assuming an exciton linewidth of ~ 6 meV. An independent set of sub-threshold angle-resolved electroluminescence characteristics, as compared to those shown in Figs. 5.3 (a) and (b), have also been measured in an independent device. The angle-resolved electroluminescence spectra and the corresponding polariton dispersion curves are shown in Fig. 5.4, from which it may be deduced that the cavity-to-exciton detuning Δ and vacuum-field Rabi splitting Ω_{VRS} to be ~ – 6 meV and ~ 37 meV, respectively. Thus, the strong coupling parameters are quite close in both of the spin devices, which have been characterized in the present section.

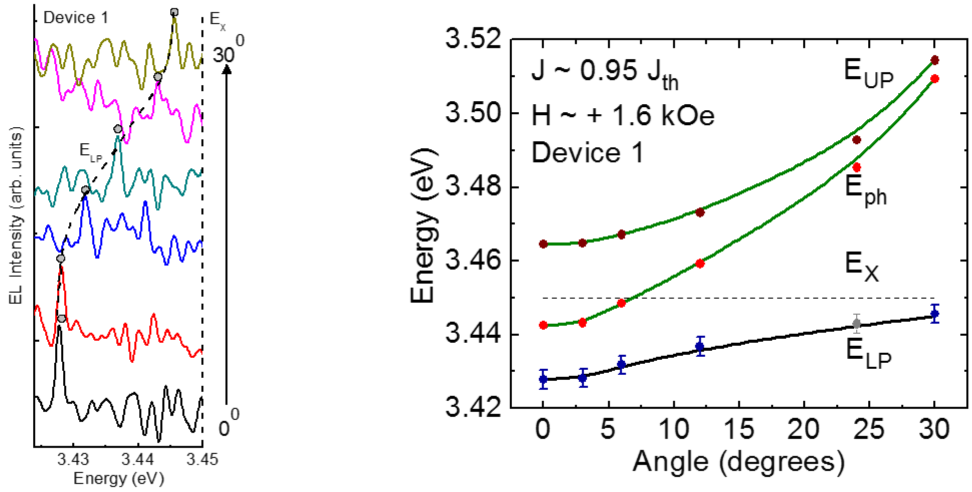

(a) (b)

Figure 5.3. (a) Sub-threshold angle-resolved electroluminescence spectra; (b) corresponding polariton dispersion curves. The red (wine) circles represent the computed cavity photon (upper-polariton) dispersion and the blue circles correspond to the "data points" in (a).

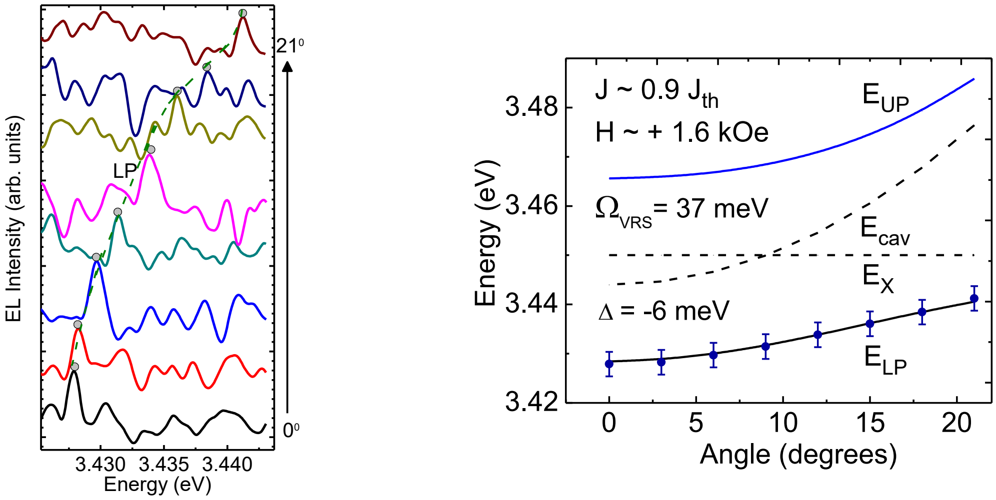

(a) (b)

Figure 5.4. (a) Measured angle-resolved electroluminescence spectra of Device 7. The spectra have been vertically offset for clarity. The dashed line represents the lower polariton (LP) transition, (b) corresponding polariton dispersion characteristics.

The process of electron spin injection should not alter the strong-coupling characteristics of these GaN-based devices in any way. The sub-threshold angle-resolved electroluminescence spectra of an identical device, having normal n-type ohmic contacts instead of ferromagnetic tunnel contacts, are shown in Fig. 5.5 (a). From the corresponding polariton dispersion curves, values for the cavity-to-exciton detuning Δ and vacuum-field Rabi splitting Ω_{VRS} are deduced to be ~ – 13 meV and ~ 33.9 meV, respectively.

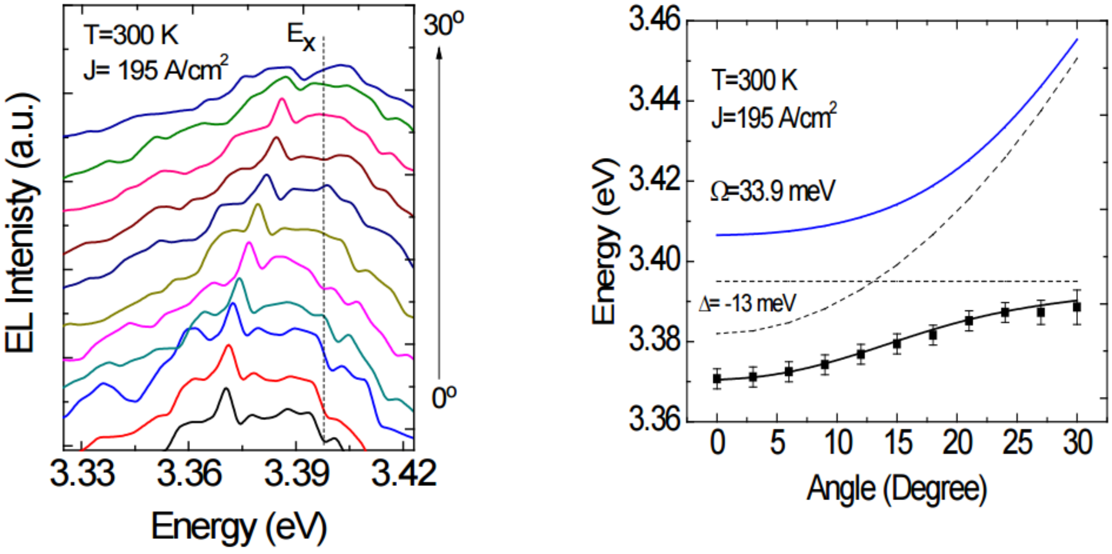

(a) (b)

Figure 5.5. (a) Measured angle-resolved electroluminescence spectra of an identical GaN-based device with n-type ohmic contacts. The spectra have been vertically offset for clarity. The dashed line represents the excitonic transition, (b) corresponding polariton dispersion characteristics.

5.4 Polariton Lasing Characteristics

The output light-current (L-I) characteristics of the devices were determined by recording the electroluminescence in the direction normal ($k_{||}$~0) to the Bragg mirrors as a function of continuous wave (CW) injection current. The measurements were made with the injection of spin-polarized electrons via the FeCo/MgO contact in a remanent magnetization state. As shown in Fig. 5.6 (for the device of Figs. 5.3 (a) and (b)), a non-linear threshold signaling the onset of stimulated scattering is observed at a current density of $J_{th} = 69$ A/cm^2.

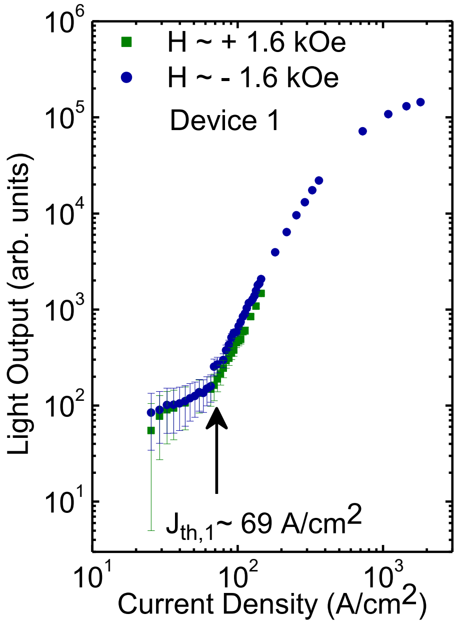

Figure 5.6. Normal incidence ($k_{\|} \sim 0$) LP electroluminescence intensities recorded as a function of injected current density after in-plane magnetization of the contacts with H ~ ± 1.6 kOe. The vertical arrow indicates the onset of non-linearity.

The corresponding lower-polariton (LP) density at the non-linear threshold is ~ 1.02 x 10^{16} cm^{-3}, calculated with a measured excitonic lifetime of ~ 0.71 ns. Similar L-I characteristics for another device are shown in Fig. 5.7 (a). With further increase of the injection current, the transition from strong to weak coupling takes place and a second non-linearity, most possibly due to population inversion and photon lasing, is observed at J ~ 7.2 kA/cm^2 (Fig. 5.7 (b)). The threshold is shown more clearly in the inset of this figure. The onset of non-linearity and polariton lasing threshold are accompanied by an abrupt reduction of the LP emission linewidth

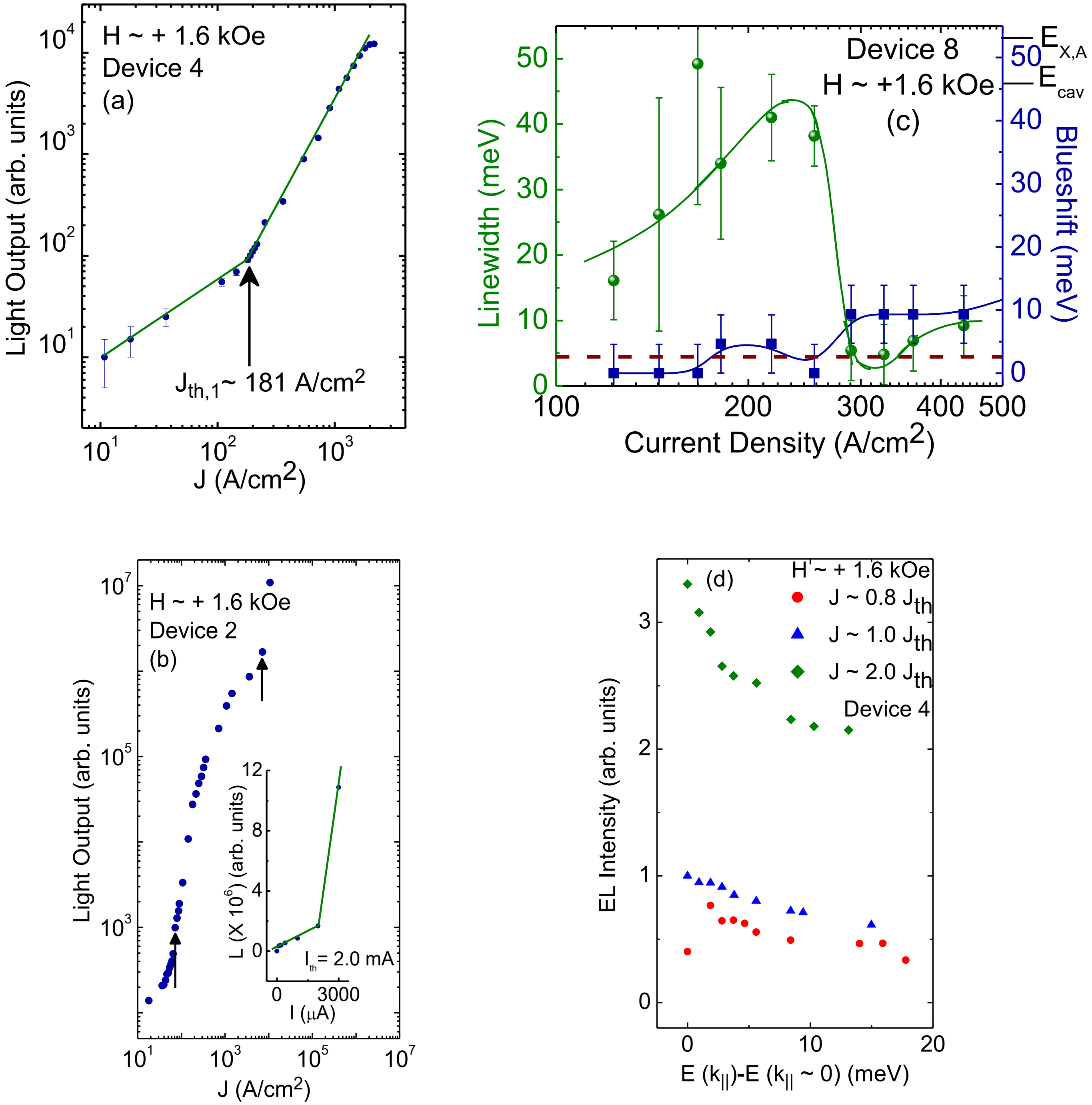

Figure 5.7 (a) Normal incidence ($k_{||} \sim 0$) LP electroluminescence intensities recorded as a function of injected current density; (b) two threshold lasing behavior with the nonlinearities due to polariton and photon lasing. The inset shows an enlargement highlighting the threshold at higher injection; (c) LP emission linewidth and blueshift of the LP electroluminescence peak emission energy as a function of injected current density. The resolution of the measurement (~ 4.6 meV) is indicated as a horizontal dashed line; (d) LP emission intensities for different $k_{||}$ states as a function of the energy difference $E(k_{||}) - E(k_{||} \sim 0)$, determined from angle-resolved electroluminescence measurements at different injection densities.

and a blue-shift of the LP electroluminescence peak energy (~ 9 meV at the polariton lasing threshold) shown in Fig. 5.7 (c). The minimum measured LP emission linewidth amongst all the devices measured is ~ 970 μeV, which corresponds to a LP coherence time of ~ 4 ps. The spontaneous radiative recombination lifetime of the lower polaritons in the condensate is estimated to be $\tau_{LP}=\tau_{ph}/\ |C(k_{||} = 0)|^2$ ~ 1.1 ps. The polariton occupation in momentum space at different injection levels was also measured in the same device by angle-resolved electroluminescence in several devices. The occupation is calculated from the output power measured with an optical power meter. The polariton condensate occupation numbers are very similar in all the devices. Representative data are shown in Fig. 5.7 (d). A random and non-thermal LP occupation below threshold transforms to a peaked occupancy at $k_{||}$~0 above threshold, indicating the formation of a coherent bosonic condensate. It may be observed, from Fig. 5.7 (d) that there is no appreciable saturation of the thermal part of the emitted LP intensity with injection beyond threshold. In general, for polariton lasers being operated in the kinetic regime, no such saturation should be expected [91]. Further, the population of certain excited states above the condensate may increase above the polariton lasing threshold due to the interplay of the phonon-assisted polariton scattering and polariton-polariton scattering. In the previous works on GaN-based polariton lasers, it has been observed that polariton-polariton interactions give rise to non-linear increase of the emission intensity with the pump intensity at large emission angles [13]. The normal incidence light-current characteristics of Devices 1 and 2 have already been discussed. The characteristics of another device (Device 3) are shown here (Fig. 5.8) for completeness. The non-linear polariton lasing threshold current of ~ 19 μA corresponds to an equivalent injected current density of ~ 69 A/cm^2, assuming the dimensions of the effective cross-sectional area of the microcavity diode in the plane normal to the diode injection current as ~ 690 nm (5λ) X 40 µm.

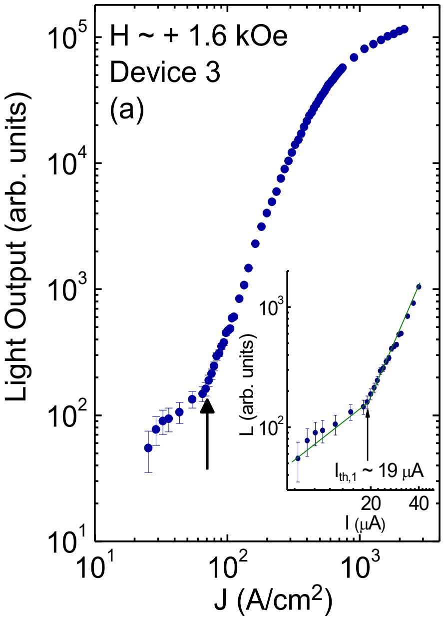

Figure 5.8. Normal incidence ($k_{||}$ ~ 0) LP electroluminescence intensities of Device 3 recorded as a function of injected current density. The inset shows an enlargement highlighting the polariton lasing threshold. The vertical arrows indicate the onset of non-linearity. The solid lines in the inset are guides to the eye.

5.5 Thermalization of the Lower-Polariton (LP) Population in Momentum ($k_{||}$) Space

The thermalization of the lower exciton-polariton population has also been examined by angle-resolved electroluminescence measurements at the polariton lasing threshold in Device 4. The polariton emission intensities were measured at each external emission angle by spectrally resolving the LP peaks (using an imaging monochromator as a spectral band-pass filter with a spectral resolution of ~ 0.03 nm) and measuring the output electroluminescence intensities by an optical power meter. At the polariton lasing threshold, it is observed that the polariton emission intensities, as a function of the collection (detection) angle, follow a quasithermal classical

Maxwell-Boltzmann-like distribution (Fig. 5.9). The angular distribution of the lower polaritons was analyzed using the relation: $N = N_0 \exp(-(E(k_{||})-E(k_{||} \sim 0))/kT_{LP})$, where $E(k_{||})$ is the LP resonance energy at the in-plane wave-vector $k_{||}$ (deduced using the one-to-one correspondence between the angle of the out-coupled photon and the in-plane wave number of the polaritons) and N_0 is the relative occupancy at $k_{||} = 0$. The "fitting" parameters in the above relation are N_0 and the effective temperature of the polariton thermal cloud T_{LP}. The relative measured occupancy N_0 at the polariton lasing threshold (~ J_{th}) has been arbitrarily set to unity. From analysis of the angle-resolved data measured at the polariton lasing threshold, one obtains $N_0 = 0.98 \pm 0.01$ and $T_{LP} = 372.3 \pm 20.7$ K. This value of T_{LP} is in excellent agreement with the effective temperature of ~ 360 ± 30 K reported by Baumberg et al. [47] in a bulk GaN-based microcavity polariton laser excited with short optical pulses at room temperature.

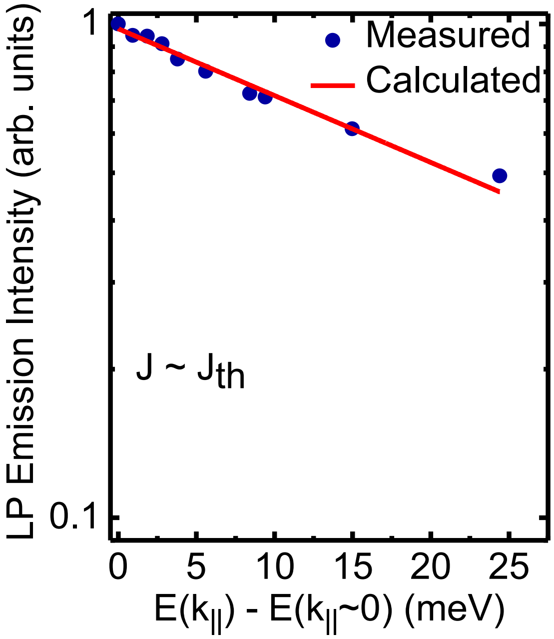

Figure 5.9. Lower exciton-polariton electroluminescence intensity measured at the polariton lasing threshold as a function of energy. The solid line depicts a classical thermal Maxwell-Boltzmann distribution-based analysis of the measured data points, from which an effective temperature T_{LP} of ~ 372 K is deduced for the polariton thermal cloud.

5.6 Output Polarization Characteristics of the Spin Polariton Laser

5.6.1 Experimental Results

The degree of circular polarization of the polariton emission in the normal direction ($k_{||}$ ~ 0) has been measured as a function of injection current in multiple devices after the application of a suitable in-plane magnetizing field to the n-type FeCo/MgO spin injector. The measurements were made in remanence with the magnetic field switched off. The degree of circular polarization above threshold follows the measured in-plane magnetization of a ~ 80 nm FeCo layer, which demonstrates that the observed electroluminescence polarization originates from the FeCo contact, as shown in Fig. 5.10. The output optical polarization state of the devices has been characterized in the quasi-Voigt geometry, wherein the externally applied in-plane magnetizing field (H) and consequently the spin angular momentum quantization axis, the components of the total angular momenta of the spin-polarized electrons and the unpolarized holes, and the wave-vector of the emitted light, are all aligned in the same direction. The magnetizing field was swept in the plane of the n-type ferromagnetic contacts along the axis of cavity resonance in the direction normal to the DBR mirrors to magnetize the spin injector contacts. The steady-state linear and circular polarization characteristics of the output LP electroluminescence as a function of the injected current density were measured in the normal direction ($k_{||}$ ~ 0) with the spin injector contact in a remanent magnetization state, after the magnetizing field is turned off. The output electroluminescence was transmitted through a UV quarter-wave ($\lambda/4$) plate, whose fast axis was appropriately oriented to the transmission axis of the following Glan-Thompson linear analyzer, to spectrally resolve the left- and right-handed circular polarization components. The circular polarization-resolved luminescence was then spectrally dispersed by a 0.75 m imaging monochromator having a spectral resolution of ~ 0.03

nm at ~ 435.8 nm and detected by a photomultiplier tube. For steady-state linear polarization measurements, the output electroluminescence was transmitted to a Glan-Thompson linear analyzer whose orientation was referenced to the [0001] crystallographic axis (c-axis), which is the structural growth axis of the microcavity diode. The polarization-resolved luminescence was spectrally dispersed by a 0.75 m Czerny-Turner imaging monochromator (with a spectral resolution of 0.023 nm at 435.8 nm) and detected by a photomultiplier tube. The degrees of linear and circular polarizations, as a function of injection, were computed from the polarization-resolved LP electroluminescence intensities at the LP emission wavelength without actually recording injection-dependent polarization-resolved spectra. The magnetizing field-dependent output circular polarization data above the polariton lasing threshold ($J \sim 1.6\ J_{th}$) has also been measured. As shown in Fig. 5.10, the degree of circular polarization above threshold is seen to track the measured in-plane magnetization of a ~ 80 nm FeCo layer, which demonstrates that the observed electroluminescence polarization originates from the FeCo contact. The discrepancy observed at higher magnetizing fields is probably due to degradation of the device contacts (measurements were made sequentially starting from negative fields) and consequent reduction in the electron spin injection efficiency of the ferromagnetic contacts. As may be observed in Fig. 5.10, reversing the direction of the magnetizing field reverses the helicity of the output circular polarization. The helicity of the circular polarization is governed by the direction of the in-plane magnetization of the ferromagnetic contact.

The measured linear polarization as a function of injection for Device 2 is shown below (Fig. 5.11). As shown in Fig. 5.11, the steady-state output linear polarization of the microcavity emission is negligible below the polariton lasing threshold. Below the condensation threshold, the degree of linear polarization has an essentially noise-limited value ranging from ~ 1.8 % to ~ 2.7 % (originating probably due to detector noise) and it increases to a maximum value of ~ 33.4 % at the polariton lasing threshold. The measured threshold for linear polarization (J ~ 72.5 A/cm^2) agree extremely well with the nonlinear threshold in the light-current characteristics (J ~ 72.5 A/cm^2 in Fig. 5.7(b)) within the limits of experimental accuracy. From Fig. 5.11, one can also observe a value of ~ 17.2 ± 5 % at J ~ 2.0 J_{th}. Figure 5.12 depicts an independent measurement on the same device (Device 2) at J ~ 2.0 J_{th}, from which a value of ~ 20.3 % can be deduced for the degree of linear polarization. It is also observed from Fig. 5.12 that the plane of linear polarization is preferentially oriented along the ~ 90^0 angle of the linear analyzer, which in our measurement geometry corresponds to the $[1\bar{1}00]$ crystallographic axis (orthogonal to the m-plane) of the wurtzite GaN crystal. It was previously observed that the linear polarization is

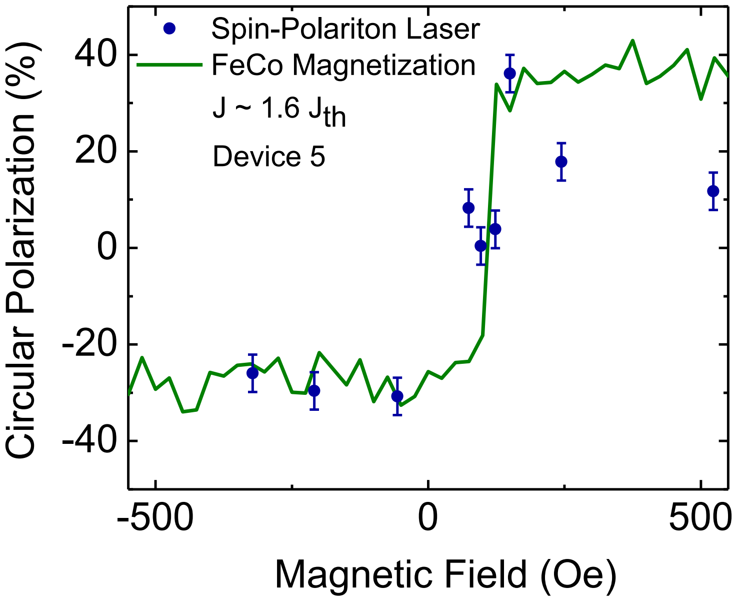

Figure 5.10. Measured steady-state degree of circular polarization as a function of magnetizing field at a constant injected current density J ~ + 1.6 J_{th}. The normalized in-plane magnetization curve for a ~ 80 nm FeCo layer is shown for comparison. (The magnetization curve is courtesy of Prof. Zunaid Baten, formerly of the Bhattacharya Research Group, University of Michigan)

similarly pinned orthogonal to the m-plane in polariton diode lasers operated with unpolarized electrical excitation. It may be remembered that the 0^0 angle of the linear analyzer corresponds to [0001] crystallographic axis (c-axis), which is the structural growth axis of the microcavity diode.

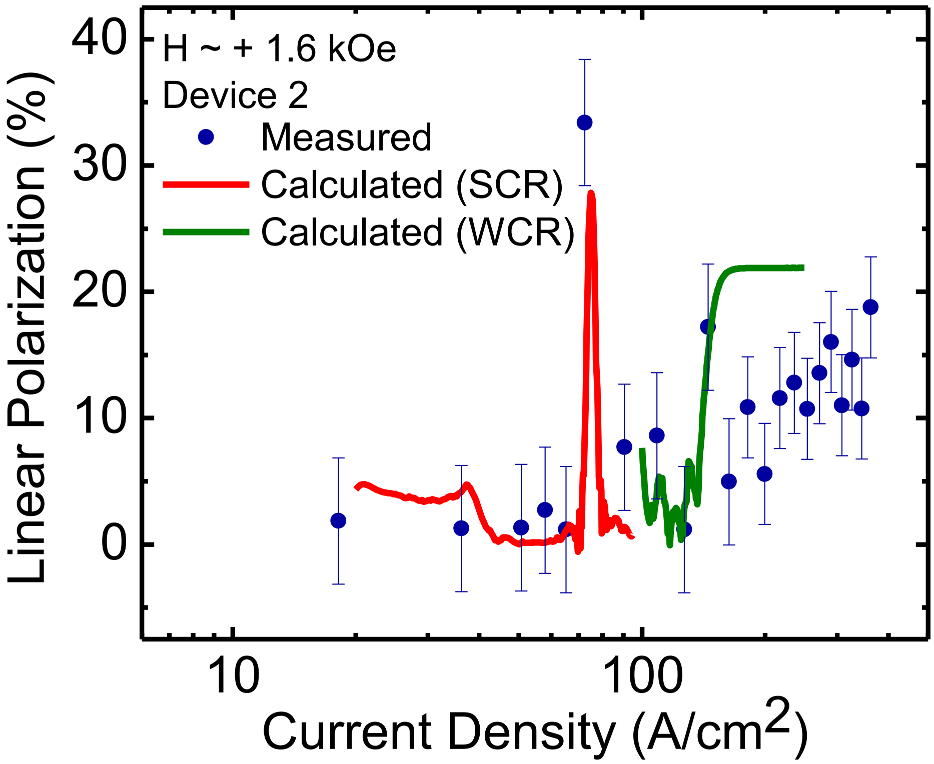

Figure 5.11. Measured steady-state degree of linear polarization as a function of injected current density recorded after in-plane magnetization of ferromagnetic contacts with H ~ + 1.6 kOe. The red (green) solid lines represents the calculated values assuming strong(weak)-coupling regime of operation.

Figure 5.13 (a) shows the circular-polarization resolved LP electroluminescence intensities measured as a function of injection after magnetization of the contacts with H ~ + 1.6 kOe. Below the non-linear threshold, the degree of circular polarization of the microcavity emission is essentially zero because of complete spin relaxation of the excitons. Above the polariton lasing threshold, with the onset of stimulated LP-LP scattering, the dynamics which populate the LP condensate states become much faster than competing spin relaxation processes and one of the

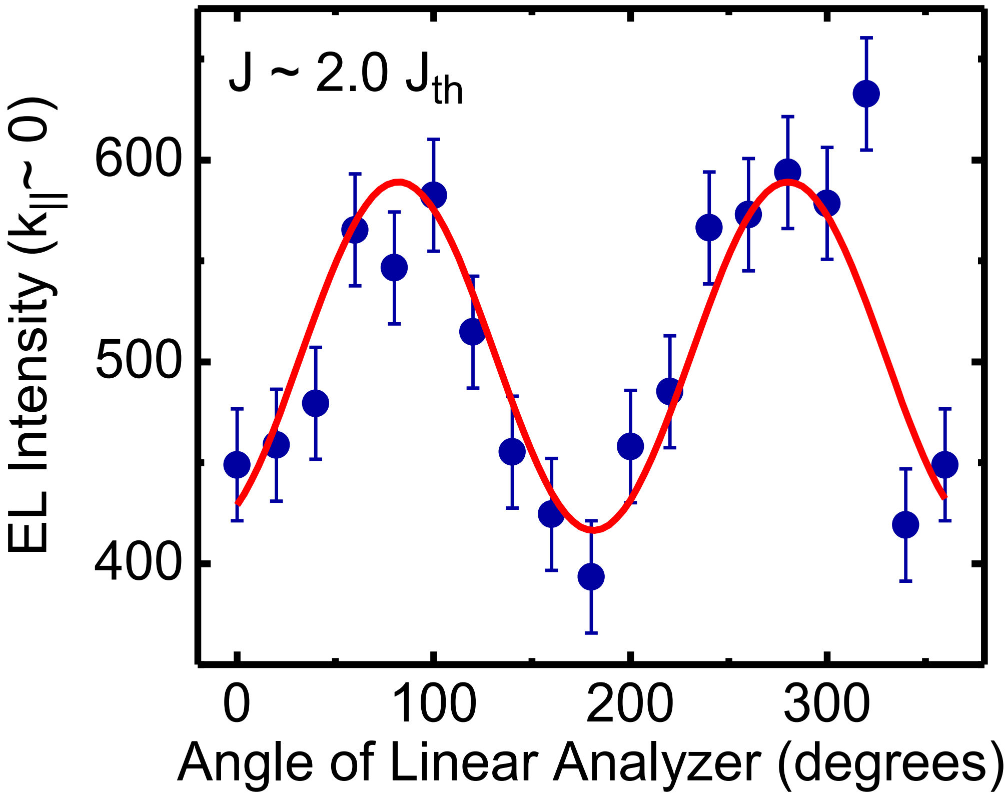

Figure 5.12. Electroluminescence intensity of the ground state emission above the polariton lasing threshold at $k_{||}$ ~ 0 measured as a function of the angle of the linear analyzer. The solid line is a guide to the eye.

spin-polarized components of the condensate increases faster than the other giving rise to a net output circular polarization. Any possible difference in threshold between the two components might be small and within the limits of experimental error. Figure 5.13 (b) depicts the measured steady state circular polarization of the output LP electroluminescence of the same device as a function of injection. There is a non-linear increase of the polarization at threshold and a maximum value of output circular polarization of ~ 25 % is observed above the non-linear threshold.

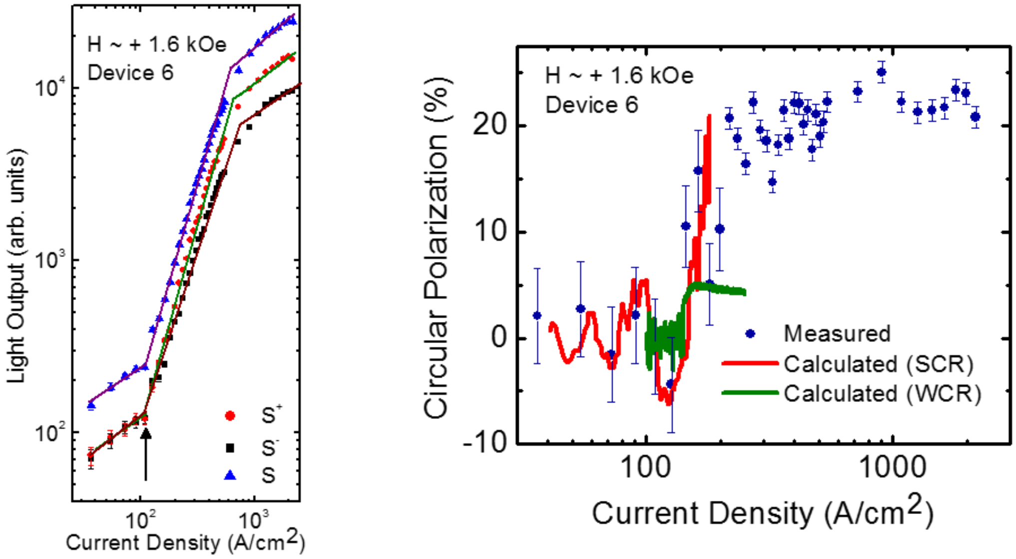

(a) (b)

Figure 5.13. (a) Measured normal incidence ($k_{||} \sim 0$) circular polarization-resolved LP electroluminescence intensities as a function of injected current density recorded after in-plane magnetization of ferromagnetic contacts with H ~ + 1.6 kOe. The total light intensity S is the summation of the right-hand (S^+) and left-hand circularly polarized (S^-) LP emission intensities. The arrow indicates the onset of non-linearity and the solid lines are guides to the eye; (b) measured steady-state degree of circular polarization as a function of injected current density recorded after in-plane magnetization of ferromagnetic contacts with H ~ + 1.6 kOe. The red (green) solid lines in (b) represent the calculated values assuming strong(weak)-coupling in the microcavity.

5.6.2 Theoretical Analysis of the Measured Data

Our collaborators, Professors Alexey Kavokin and Professor Ivan Iorsh, performed the theoretical analysis detailed here. The circular polarization is superimposed on the linear polarization of the output to produce a net elliptic polarization. The measured polarization results, have been analyzed with some simplifying assumptions, with the object of verifying the build-up of circular spin polarization due to the bosonic stimulation effect. The injected carriers are assumed to be partially spin polarized. The ground state of the polariton condensate is also assumed to be subjected to the in-plane effective magnetic field originating from the splitting of X and Y polarized polariton states. The spin-dependent polariton-polariton interactions in the condensate are considered. Holes are assumed to be unpolarized and thus the spin polarization in the electron-hole plasma originates entirely due to the spin-polarized electrons. The rate equations for free carriers and incoherent excitons as well as the Gross-Pitaevskii equations for the polariton condensate, written in the basis of spin-up and spin-down electron states and corresponding optically active exciton states, are as follows:

$$\frac{dN_e^{\uparrow}}{dt} = \xi P - W_{exc-form} N_e^{\uparrow} N_R^{\uparrow} + \frac{1}{\tau_{s,e}}(N_e^{\downarrow} - N_e^{\uparrow}); \frac{dN_e^{\downarrow}}{dt} = (1-\xi)P - W_{exc-form} N_e^{\downarrow} N_R^{\downarrow} - \frac{1}{\tau_{s,e}}(N_e^{\downarrow} - N_e^{\uparrow})$$

$$\frac{dN_R^{\uparrow,\downarrow}}{dt} = -\frac{N_R^{\uparrow,\downarrow}}{\tau_R} + W_{exc-form} N_e^{\uparrow,\downarrow} N_R^{\uparrow,\downarrow} \pm \frac{1}{\tau_{s,R}}(N_R^{\downarrow,\downarrow} - N_R^{\uparrow,\uparrow}) - (a_{ph} N_R^{\uparrow,\downarrow} + b_{exc} N_R^{\uparrow,\downarrow 2})(1+|\Psi^{\uparrow,\downarrow}|^2)$$

$$i\mathrm{h}\frac{d\Psi^{\uparrow,\downarrow}}{dt} = E\Psi^{\uparrow,\downarrow} + i\mathrm{h}(a_{ph} N_R^{\uparrow,\downarrow} + b_{exc} N_R^{\uparrow,\downarrow 2})\Psi^{\uparrow} - \frac{i\mathrm{h}}{\tau_c}\Psi^{\uparrow,\downarrow} + \alpha_1 |\Psi^{\uparrow,\downarrow}|^2 \Psi^{\uparrow,\downarrow} + \alpha_2 |\Psi^{\downarrow,\uparrow}|^2 \Psi^{\uparrow,\downarrow} \pm \Omega\Psi^{\downarrow,\uparrow}$$

(1)

Here $N_e^{\uparrow}, N_e^{\downarrow}, N_R^{\uparrow}, N_R^{\downarrow}$ are the electron and exciton reservoir occupation numbers corresponding to spin-up and spin-down electron states, respectively, $\Psi^{\uparrow}, \Psi^{\downarrow}$ are the wavefunctions of spin-up and spin-down polariton condensates, ξ is the degree of spin polarization of the injection current corresponding to an electron spin injection efficiency of ~ 8 % [92], P is the injected current density; $W_{exc-form} \sim 0.1$ ps^{-1} is the exciton formation rate, $\tau_{s,e} \sim 40$ ps is the electron spin relaxation time [92], $\tau_{s,R} \sim 0.2$ ps is the exciton pseudospin relaxation time [93], $\tau_R = 1$ ns is the exciton non-radiative recombination time, a_{ph} = 7 X 10^{-10} ps^{-1}, b_{exc} =10^{-10} ps^{-1} are the phonon-polariton and polariton-polariton scattering rates, $\tau_c \sim 1$ ps is the polariton lifetime, $\alpha_1 = 4\ \mu\text{eV}, \alpha_2 = -0.4\ \mu\text{eV}$ are the nonlinearity parameters describing the interactions of polaritons with parallel and antiparallel spins, respectively, and $\Omega = 0.1\ \text{meV}$ is the linear polarization splitting that governs the effective magnetic field acting upon the polariton pseudospin components [9].The calculated variation of circular polarization with injection is shown alongside the measured data in Fig. 5.13 (b) and a good agreement is observed. In contrast, calculations performed assuming the weak-coupling regime of operation (zero magnitudes for the interaction coefficients and the linear polarization splitting) cannot reproduce the measured data. The calculated variation of linear polarization with injection is also shown alongside the measured data in Fig. 5.11 (b) and a good agreement is observed in this case as well.

5.6.3 Magnetizing-Field (H-Field) Dependent Light-Current of the Ground-State ($k_{||} \sim 0$) LP Electroluminescence

The effect, if any, of the in-plane magnetizing field (H-field) on the light-current characteristics of polariton diode lasers, has also been examined. Measurements are made at remanence after magnetizing the n-type ferromagnetic contacts with varying magnitudes and polarities of H-fields, as shown in Fig. 5.14. At two magnitudes of H-fields (H ~ + 83.6 Oe and ~ + 1.6 kOe), the spectrally resolved electroluminescence intensities are measured up to a slightly higher injection (~ 500 µA) to observe the restoration of linearity in the light-current characteristics beyond the non-linear enhancement in the active lasing regime. It is observed that there is no appreciable difference in the threshold currents for the cases plotted in Fig. 5.14

within the margin of measurement errors. The threshold current I_{th} is found to vary from ~ 14 µA to ~ 19 µA and may be attributed to measurement errors and or, slight variations and or changes in the device properties (such as the contacts potentially changing the injection efficiency) with extensive measurement and consequent device heating and degradation. Further, any changes in the LP electroluminescence intensities may be attributed to slight changes in the optical alignment and other experimental conditions.

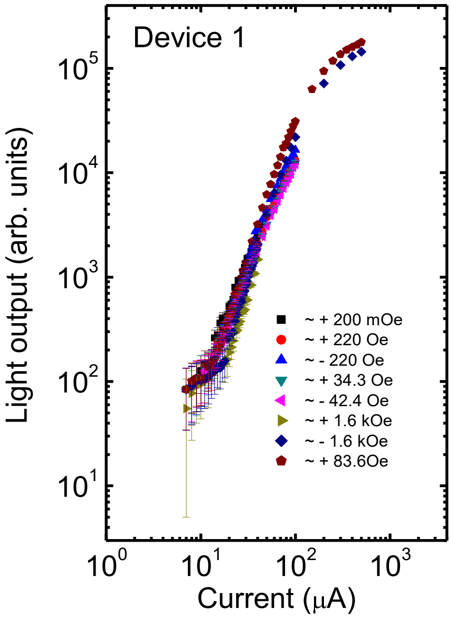

Figure 5.14. Normal incidence ($k_{||}$ ~ 0) LP electroluminescence intensities recorded as a function of injected current density, for varying magnitudes and polarities of in-plane magnetizing fields (H-fields) employed to magnetize the n-type ferromagnetic contacts. All measurements were made at remanence in the absence of any magnetic field.

5.7 Mach-Zehnder Interferometry Measurements

The far-field interference pattern of the polariton condensate was measured using a slightly misaligned Mach-Zehnder interferometer to ascertain the spatial coherence properties of the output LP electroluminescence. An UV beam splitter is utilized to split the output luminescence from the device, generating two identical copies of the LP emission which are transmitted through two perfectly balanced arms of the interferometer. The two copies of the emission intensity profile are then made to interfere with each other in the far-field by overlapping them spatially, which is accomplished by tuning the orientation of one of the reflecting mirrors for one path which is mounted diagonally on a piezo-stage. The system creates a double image of the condensate with a spatial resolution of ~ 1 μm. A pinhole placed at the image plane serves as a spatial filter for selecting the dark and bright fringes, the intensities of which are measured by a photomultiplier tube after spectrally filtering with an imaging monochromator. The visibilities at several injections were calculated from the recorded LP emission intensities without actually imaging the interference pattern. This was done because the output luminescence, at the far-field image plane, was below the sensitivity of the UV CCD cameras at our disposal. The measured interference fringe contrast (interference fringe visibility) is plotted as a function of the injection current in Fig. 5.15. The interference fringe contrast is computed as $C = (I_{max} - I_{min}) / (I_{max} + I_{min})$, where I_{max} and I_{min} denote the maximum (bright fringe) and the minimum (dark fringe) LP emission intensities of the interference pattern, respectively. Below threshold, the contrast has an essentially noise limited value ranging from ~ 3 % to ~ 6 % and it increases to a value of ~ 24 % at the polariton lasing threshold. A peak visibility of ~ 44 % is recorded above threshold at an injected current density of $J = 1.4\ J_{th}$.

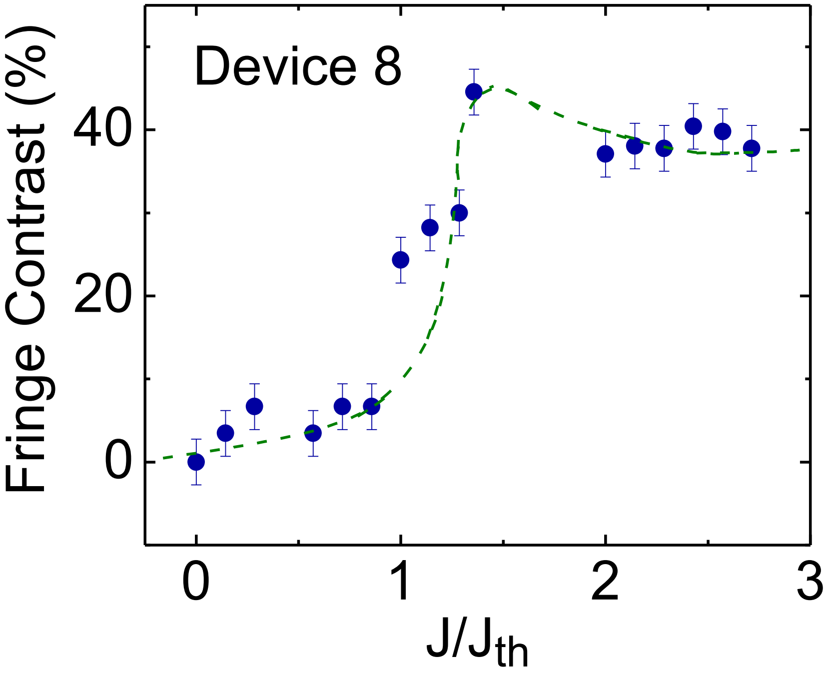

Figure 5.15. Interference visibility measured as a function of the injected current density for approximately zero displacement between the double images of the normal-incidence LP emission. The dashed line is a guide to the eye.

5.8 Summary

Thus, it may be concluded that stimulated scattering of spin-polarized excitons to the polariton condensate above the lasing threshold leads to the build-up of circular polarization of the emission of polariton lasers which paves the way to realization of a low-threshold semiconductor source of coherent circularly polarized UV to blue light. In contrast, spin-VCSELs have to be magnetized along the hard axis of the spin-injector and thus require higher fields for operation [19, 33, 94-95]. Further, while the operation of the spin polariton laser considered in the present study is at room temperature, spin-VCSELs have been operated only at low temperatures. The threshold current densities of previously reported electrically injected spin-VCSELs range from ~ 2 kA/cm^2 to ~ 8 kA/cm^2 [19, 33, 94-95]. The threshold current densities in the present spin-polarized polariton lasers range from ~ 69 A/cm^2 to ~ 181 A/cm^2, which are significantly lower. While a degree of output circular polarization of ~ 25 % has been observed in the present devices above threshold, a degree of circular polarization ranging from ~ 8 % [94] to ~ 23 % [19] were observed in the spin-VCSELs. Higher degrees of circular polarization (~ 55 %) were also demonstrated in the spin-VCSELs by adopting a specialized electrical biasing scheme [33].

In conclusion, electrical spin injection from a FeCo/MgO Schottky tunnel barrier in an electrically pumped spin polariton diode laser, has been demonstrated. The polariton lasing characteristics have been measured with spin polarized injection current in remanence. The measured output circular and linear polarization have been analyzed by solving the rate equations for free carriers and excitons and the Gross-Pitaevskii equations for the polariton condensate. The device represents a bias-tunable low energy coherent polarized light source operating at room temperature.

Chapter VI

Spin-injection-induced Gain Anisotropy in a Polariton Diode Laser

6.1 Introduction

An exciton-polariton laser is a microcavity light source where coherent photons are emitted from a non-equilibrium and degenerate polariton condensate by spontaneous emission in the strong coupling regime of exciton-photon interaction. Stimulated polariton-polariton scattering [96] is the relevant phase-coherent optical gain mechanism in these devices. The separation of the processes of bosonic final-state stimulation and emission leads to coherent emission without the need for population inversion, as in a conventional photon laser, and therefore the threshold pump level is considerably smaller. This has been amply demonstrated in optically and electrically pumped polariton lasers realized with several materials and semiconductor heterostructures as has been discussed in Chapters III and V. The output polarization in the steady state, above threshold, can be linear or circular, or a combination of both, depending on the nature of the excitation, defect-induced pinning and static disorder in the microcavity, TE-TM splitting of the excitonic pseudospins, and injection density. Spontaneous stochastic circular polarization has also been observed in GaAs-based polariton condensates at low temperatures [46].

On the other hand, Chapter V discussed how a controlled and variable circularly polarized output can be obtained by injecting spin-polarized electrons in a polariton diode laser. The magnitude and helicity of the output circular polarization is deterministically governed by the in-plane magnetization of the ferromagnetic contacts. Preferential injection of spin-polarized carriers leads to a differential population of exciton pseudospins and it is the relative spin relaxation rates compared to the polariton scattering rates that ultimately determine the nature and evolution of the polarization of the optical output as a function of excitation. In the present study, the individual polarized components of the output have been investigated in detail in the context of spin-induced gain anisotropy (anisotropy in stimulated scattering rate) in the polariton condensate. The gain anisotropy gives rise to hitherto unidentified effects such as threshold lowering of the preferred polarization mode and enhancement of the output emission intensity at and beyond the threshold. The calculated data have been compared with measured ones, where possible. The dynamical behavior of the output polarization components has also been examined for the first time by using the relevant spin-dependent rate equation model. Spontaneous magnetization in a GaAs-based exciton-polariton condensate has been previously demonstrated; wherein condensates spontaneously emerge in either of two discrete spin-polarized states, which emit highly circularly polarized coherent light (up to ~ 95%) [46]. Although this is a remarkable observation, nevertheless the output circular polarization is essentially stochastic and uncontrolled. In this chapter, a simple and elegant mechanism to generate highly circularly polarized emission at room temperature in GaN-based condensates, which is deterministic and thus amenable to external manipulation. The helicity is controlled exclusively by the magnetization of the electron spin injector. High frequency relaxation oscillations are observed in the calculated output, which result from the dynamic exchange of energy between carriers and exciton-polaritons, for the two polarization components. The present study reveals that very high output circular polarizations, close to 100 %, can be obtained with a modulated biasing scheme, even with rather modest values of injected electron spin polarization such as ~ 8 %, which are practically feasible at room temperature, as has been demonstrated in Chapter IV.

6.2 Spin-Dependent Rate Equation Model

The output optical characteristics of electrically pumped bulk GaN-based spin-polarized microcavity polariton lasers was discussed in the previous chapter. These double heterostructure edge-emitting microcavity diodes with side-clad dielectric Bragg reflector (DBR) mirrors and vertical current injection are characterized by a typical emission wavelength λ ~ 365 nm. Typical values for the cavity-to-exciton detuning Δ and the vacuum-field Rabi splitting Ω_{VRS} in these devices are ~ – 7.5 meV and ~ 36.1 meV, respectively. An important objective of the work was the study of the evolution of the steady-state output circular polarization with injection. The degree of circular polarization of the lower-polariton (LP) emission in the normal direction ($k_{||}$ ~ 0) was measured as a function of injection current after the application of a suitable in-plane magnetizing field to the n-type FeCo/MgO spin injector. The measurements were made in remanence, with the magnetic field switched off, with continuous-wave (CW) current injection. Figure 5.1(a) shows the circular-polarization resolved lower-polariton (LP) occupation numbers measured as a function of injection after magnetization of the contacts with H ~ + 1.6 kOe. These ground-state occupancies are estimated by normalizing to unity the recorded electroluminescence intensities for each of the helicities, at their respective thresholds. The inset of Fig. 6.1(a) depicts the measured steady state circular polarization of the output LP electroluminescence as a function of injection, deduced from the data of Fig. 6.1(a). There is a non-linear increase of the polarization at threshold and a maximum value of output circular polarization of ~ 25 % is observed above the non-linear threshold. These experimental data have already been reported in the previous chapter.

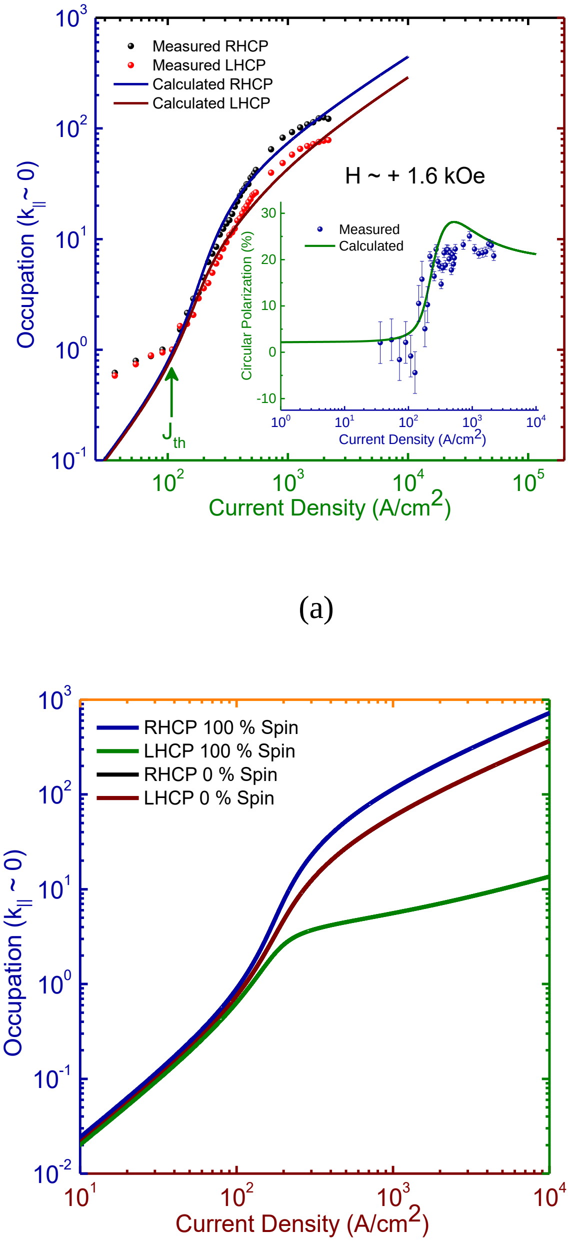

(a)

(b)

Figure 6.1 (a) Circular polarization-resolved lower-polariton (LP) occupation numbers, measured along angle of zero emission ($k_{||}$ ~ 0), as a function of injected current density recorded after in-plane magnetization of ferromagnetic contacts with H ~ + 1.6 kOe. The solid blue (brown) line represents the calculated light-current characteristics for the right (left)-circularly polarized components, respectively. The inset shows the measured steady-state degree of circular polarization as a function of injected current density. The green solid line, in the inset, represents the calculated polarization values; (b) circular polarization-resolved lower-polariton (LP) occupation numbers, calculated for zero angle of emission ($k_{||} \sim 0$), as a function of injected current density, for 100 % and 0 % injected electron spin polarizations, respectively.

Experimental data showing the strong coupling regime of operation of these polariton laser diodes and their output spectral characteristics, such as the emission linewidth and blueshift of the peak emission energy, have also been discussed in the previous chapter.

The measured circular polarization have been analyzed results with the object of investigating the magnification of the injected spin polarization due to the bosonic stimulation effect, using a spin-dependent rate equation model. This rate equation model has been devised following Iorsh et al. [51], wherein they present a simplified quasi-analytic model for GaN-based polariton lasers. The injected electrons are assumed to be partially spin polarized. The following rate equations for free carriers, excitons and exciton-polaritons are solved, taking into account both of their respective spin projections along the axis of light emission:

$$\frac{dN_{eh}^{\uparrow}}{dt} = \xi\frac{\vec{J}.\vec{S}}{q} - \frac{N_{eh}^{\uparrow}}{\tau_{eh}} - WN_{eh}^{\uparrow} + \left(\frac{N_{eh}^{\downarrow} - N_{eh}^{\uparrow}}{\tau_{s,e}}\right) \tag{1}$$

$$\frac{dN_{eh}^{\downarrow}}{dt} = (1-\xi)\frac{\vec{J}.\vec{S}}{q} - \frac{N_{eh}^{\downarrow}}{\tau_{eh}} - WN_{eh}^{\downarrow} - \left(\frac{N_{eh}^{\downarrow} - N_{eh}^{\uparrow}}{\tau_{s,e}}\right) \tag{2}$$

$$\frac{dN_{R}^{\uparrow}}{dt} = -\frac{N_{R}^{\uparrow}}{\tau_{R}} + \left(\frac{N_{R}^{\downarrow} - N_{R}^{\uparrow}}{\tau_{s,R}}\right) + WN_{eh}^{\uparrow} - aN_{R}^{\uparrow}(N_{P}^{\uparrow}+1) + ae^{-\beta\Delta_{\text{esc}}}N_{P}^{\uparrow}N_{R}^{\uparrow} - b(N_{R}^{\uparrow})^{2}(N_{P}^{\uparrow}+1) - cN_{eh}^{\uparrow}N_{R}^{\uparrow}(N_{P}^{\uparrow}+1) \tag{3}$$

$$\frac{dN_{R}^{\downarrow}}{dt} = -\frac{N_{R}^{\downarrow}}{\tau_{R}} - \left(\frac{N_{R}^{\downarrow} - N_{R}^{\uparrow}}{\tau_{s,R}}\right) + WN_{eh}^{\downarrow} - aN_{R}^{\downarrow}(N_{P}^{\downarrow}+1) + ae^{-\beta\Delta_{\text{esc}}}N_{P}^{\downarrow}N_{R}^{\downarrow} - b(N_{R}^{\downarrow})^{2}(N_{P}^{\downarrow}+1) - cN_{eh}^{\downarrow}N_{R}^{\downarrow}(N_{P}^{\downarrow}+1) \tag{4}$$

$$\frac{dN_{P}^{\uparrow}}{dt} = -\frac{N_{P}^{\uparrow}}{\tau_{P}} + aN_{R}^{\uparrow}(N_{P}^{\uparrow}+1) - ae^{-\beta\Delta_{\text{esc}}}N_{P}^{\uparrow}N_{R}^{\uparrow} + b(N_{R}^{\uparrow})^{2}(N_{P}^{\uparrow}+1) + cN_{eh}^{\uparrow}N_{R}^{\uparrow}(N_{P}^{\uparrow}+1) + \gamma(N_{P}^{\downarrow} - N_{P}^{\uparrow}) \tag{5}$$

$$\frac{dN_{P}^{\downarrow}}{dt} = -\frac{N_{P}^{\downarrow}}{\tau_{P}} + aN_{R}^{\downarrow}(N_{P}^{\downarrow}+1) - ae^{-\beta\Delta_{\text{esc}}}N_{P}^{\downarrow}N_{R}^{\downarrow} + b(N_{R}^{\downarrow})^{2}(N_{P}^{\downarrow}+1) + cN_{eh}^{\downarrow}N_{R}^{\downarrow}(N_{P}^{\downarrow}+1) - \gamma(N_{P}^{\downarrow} - N_{P}^{\uparrow}) \tag{6}$$

Here $N_{eh}^{\uparrow}$, $N_{eh}^{\downarrow}$, $N_{R}^{\uparrow}$, $N_{R}^{\downarrow}$, $N_{P}^{\uparrow}$ and $N_{P}^{\downarrow}$ are the electron, exciton reservoir and ground-state lower-polariton occupation numbers corresponding to spin-up and spin-down electron states, respectively, ξ is the pump current spin polarization assumed to be ~ 60 %, J is the injected current density, S is the cross-sectional area of the active region of the microcavity diode having dimensions of 690 nm by 40 μm, $W \sim 10000$ ps^{-1} is the excitonic formation rate, $\tau_{s,e} \sim 40$ ps is the electron spin relaxation time, $\tau_{eh} \sim 2000$ ps is the total electron-hole recombination lifetime,

$\tau_R = 1$ ns is the exciton non-radiative recombination time, $\tau_{s,R} \sim 120$ ps is the excitonic pseudospin relaxation time, $a \sim 10^{-7}$ ps^{-1}, $b \sim 10^{-9}$ ps^{-1}, $c \sim 10^{-14}$ ps^{-1} are the phonon-polariton, polariton-polariton and polariton-electron scattering rates, $\beta = 1/k_BT$, $\Delta_{esc} \sim 20$ meV is the trap depth of the LP branch, $\tau_c \sim 1$ ps is the polariton lifetime, and $\gamma \sim 0.035$ ps^{-1} is the effective spin relaxation for the lower-polaritons at the band bottom. The pump current spin polarization is defined as $\xi = (1 + P_{spin})/2$ where P_{spin} is the injected electron spin polarization. This definition is also consistent with the formalism presented in the previous chapter. Thus, for example, an injected electron spin polarization of 8 % ($P_{spin} = 0.08$) translates to a pump current spin polarization of 54 % ($\xi = 0.54$). Further, to theoretically incorporate the effects of non-idealities in the device performance, principally nonradiative recombination and carrier leakage from the active recombination region, a damping factor has been introduced for the electrical excitation. Replacing J by J^{η} where $\eta \sim 0.7$, gives best agreement to our measured data. This is consistent with a previous analysis of the sub-threshold regime of the polariton light-current characteristics in similar devices, as discussed in Ref. [16]. The calculated variation of the circular polarization-resolved light-current characteristics is shown alongside the measured data in Fig. 6.1(a) and a good agreement is observed. It has been reported, that because of the various uncertainties in the process of estimation, there can be up to one order of magnitude uncertainty in the ground-state polariton occupations at threshold which explains the observed discrepancy below threshold [13]. The agreement of the measured output circular polarization data with calculated values is shown in the inset of Fig. 5.1(a).

The excitonic formation term is non-linear in the present model as well as in the one presented in the previous chapter. Here, the total unbound electron-hole plasma occupation number has been used as a single quantity, instead of individual electron and hole densities, and thus this term in equations (1) and (2) apparently looks linear. Other significant differences between the two formalisms include the inclusion of terms accounting for polariton-electron scattering and phonon-assisted depopulation of the polariton ground state in the present work. There is an appreciable variation in the values of some of the parameters, especially those corresponding to the excitonic terms, in the present theoretical model as compared to those in the coupled stochastic differential equation model of the previous chapter. The origin of these differences is not entirely apparent. In all probability, it may be a complex interplay of the different natures of terms, which have been included in each of the models. Further, in the coupled stochastic differential equation approach, a complex additive white Gaussian noise term is usually introduced to explicitly bring about symmetry breaking. This has been both theoretically discussed [58] as well as experimentally justified in the literature [17, 18]. In the present chapter, a simplified approach, which results in a smooth variation of the calculated parameters such as of the ground-state occupations as a function of excitation, has been employed.

6.3 Spin-induced Gain Anisotropy

In Fig. 6.1(b), two contrasting cases are studied, wherein all the above parameters are kept identical, and the magnitude of the pump current (injected electron) spin polarization is increased to 100 % (100 %) and decreased to 50 % (0 %), respectively. Even with 100 % spin polarization of the CW pump current, a maximum steady-state degree of circular polarization of ~ 90 % is calculated. This motivated us to explore alternate biasing schemes to enhance the output polarization to almost unity, even when using small values for the pump current spin polarization such as ~ 60 %, which are practically realizable in these devices. It is important to

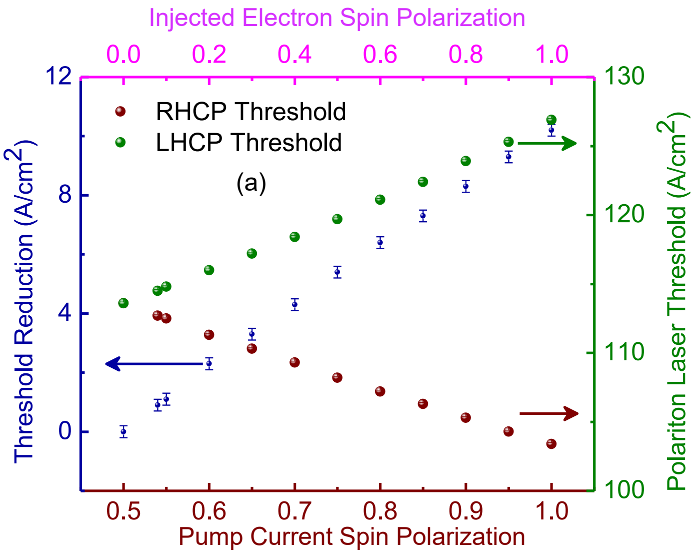

(a)

Figure 6.2 (a) Variation of the calculated polariton laser thresholds for each of the individual helicities, and the reduction in the threshold for the preferred polarization component (right-hand circularly polarized) with respect to that for operation without spin injection, as a function of the pump current spin polarization. The errors bars represent the uncertainties in the process of estimation of the threshold reduction, originating from the resolution of current density used in our calculations;

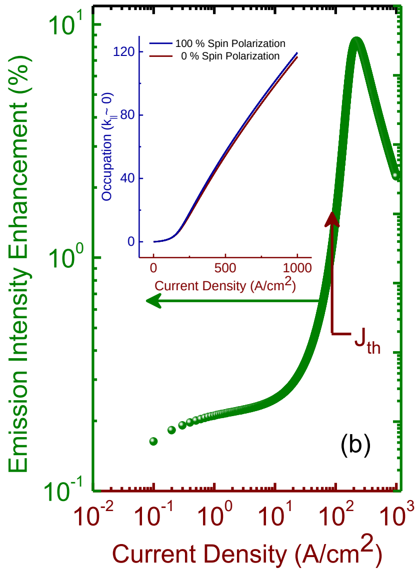

(b)

Figure 6.2 (b) Percentage of enhancement of the total electroluminescence on switching from 0 % to 100 % electron spin polarization, as a function of the injected current density. The inset shows the two light-current characteristics plotted in a double linear scale, to clearly depict the separation in the two, effected by the process of electron spin injection.

note that a reduction in the threshold for the right-hand circularly polarized (RHCP) component with 100 % pump current spin polarization is observed in Fig. 6.1(b). Thus, the dependence of the polariton laser thresholds, for both helicities, has been subsequently examined as a function of the pump current spin polarization. Throughout this chapter, the condensation threshold has been defined as the value of the injected current density at which the total ground-state polariton occupation ($k_{||} \sim 0$) becomes unity. The exact same definition is used for each of the individual spin-polarized components of the ground state. As seen in Fig. 6.2(a), with increasing value of the pump current spin polarization, the polariton laser thresholds for the two polarizations are further separated. This is a direct evidence of spin-induced gain anisotropy in a polariton laser operated with electrical spin injection. The threshold reduction is defined as the reduction in the threshold of the preferred polarization mode with respect to the threshold of an exactly equivalent polariton laser operated with no net spin injection. A maximum reduction of 10.2 A/cm^2 (~ 10 %) is predicted for operation with 100 % pump current spin polarization, assuming all other device parameters remain unchanged. It should be noted that for operation with ~ 60 % pump current spin polarization, a difference of ~ 5 A/cm^2 between the thresholds for the two helicities has been calculated, which is not clearly observable in the measured data. This can be attributed to the uncertainties in the magnitudes of the LP electroluminescence intensities at or near threshold due to measurement error, which lead to difficulties in the assignment of threshold exactly from light (output)-current characteristics. Further, it has been reported by other groups that in GaN-based microcavities there can be several factors, which contribute to errors in the process of estimation of the $k_{||} \sim 0$ occupancies, directly from the data for zero emission angle [13]. The above-mentioned phenomenon of threshold reduction for the two different circular polarizations has been previously experimentally observed in optically excited polariton lasers

[97, 98]. However, an external magnetic field in the Faraday geometry, instead of injection of spin-polarized electrons, was used to induce spin anisotropy by inducing LP condensation in the lower of the two Zeeman-split spin states.

Because of spin-induced gain anisotropy and the resulting threshold reduction, a spin polariton laser is expected to exhibit an increase in the total optical power for a given bias current under spin-polarized pumping. Here, the emission intensity enhancement is defined as $\Delta S = (S-S_0)/S_0$, where S (S_0) is the total light intensity output for a polariton laser operated with spin-polarized (conventional) electrical injection. Figure 6.2 (b) shows the non-linear increase of the emission intensity enhancement, ΔS, above the polariton laser threshold when operated with 100 % pump current spin polarization. A maximum enhancement of ~ 8.5 % is theoretically predicted above threshold. The inset shows the calculated total light (output)-current characteristics for operation with 100 % and 0 % injected electron spin polarizations respectively, from which the percentage of enhancement of the total electroluminescence on switching from 0 % to 100 % electron spin polarization, as a function of the injected current density, has been determined.

6.4 Temporal Behavior of Polarization

Finally, the temporal evolution of the circular polarization in the output emission is studied. In Fig. 6.3(a), the occupation numbers of the two spin components under the influence of a unit step response, are resolved in the time domain. All the parameters in the calculations are kept identical to those used to analyze the data in Fig. 6.1(a). A suitable excitation level is chosen above the polariton laser threshold (~ 2 kA/cm^2), where the strong-coupling characteristics are still maintained, and at which relaxation oscillations in the output circular polarization become evident. The oscillations in the polariton occupations are a result of the interplay of the various scattering processes, which populate and depopulate the ground state, and the polariton spin relaxation mechanisms, which bring about an exchange of polaritons between the two opposite circular polarizations. The fact that the oscillations are out of phase is a direct consequence of seeding the ground-state with an initial spin imbalance originating from the electron spin injection process, which eventually leads to a higher steady-state oscillation amplitude for the preferred polarization component. The large amplitude of the relaxation oscillation of the degree of circular polarization (~ 85 %) seen in the inset is promising in that it can be efficiently measured with a periodic biasing scheme. To that end, the laser is electrically excited with a high-frequency periodic square wave pulse train. The period of the excitation is chosen to be 2 ns, from the calculated temporal decay in Fig. 6.3(a). A duty cycle of ~ 10 % is found to give the best results, preventing any appreciable undershoot of the degree of circular polarization during the time-period when the pulse is active, thus giving rise to a large positive magnitude of the circular polarization. As shown in Fig. 6.3(b), a large value for the degree of output circular polarization (~ 82.5 %) is observed, even when operating with an injected electron spin polarization of ~ 8 %, a ten-fold enhancement in the process of transduction of the injected electron spin angular momentum to the circular spin polarization of the coherently emitted photon. A detector, operated synchronously with the excitation source, will be able to sample the strongly polarized output generated after the initiation of every pulse, with the sampling carried out for a period of ~ 250 ps after the commencement of every new cycle. The inset shows the temporal variation of the two LP components, under these excitation conditions.

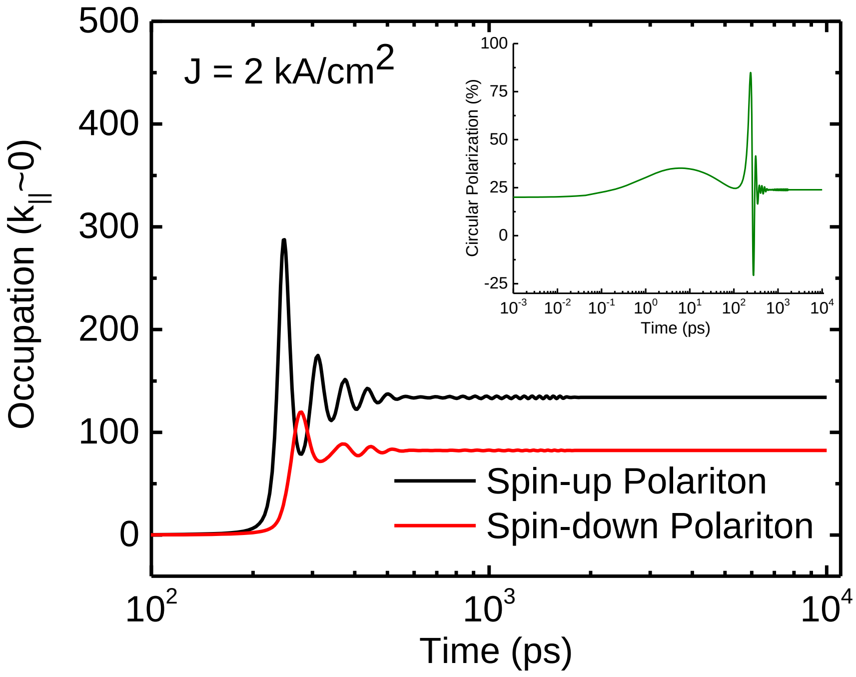

(a)

Figure 6.3 (a) Calculated temporal evolution of the spin-up and spin-down lower-polariton (LP) occupation numbers for the case of electrical excitation with a 2 kA/cm^2 step function. The inset shows the corresponding evolution of the degree of the output circular polarization under identical conditions;

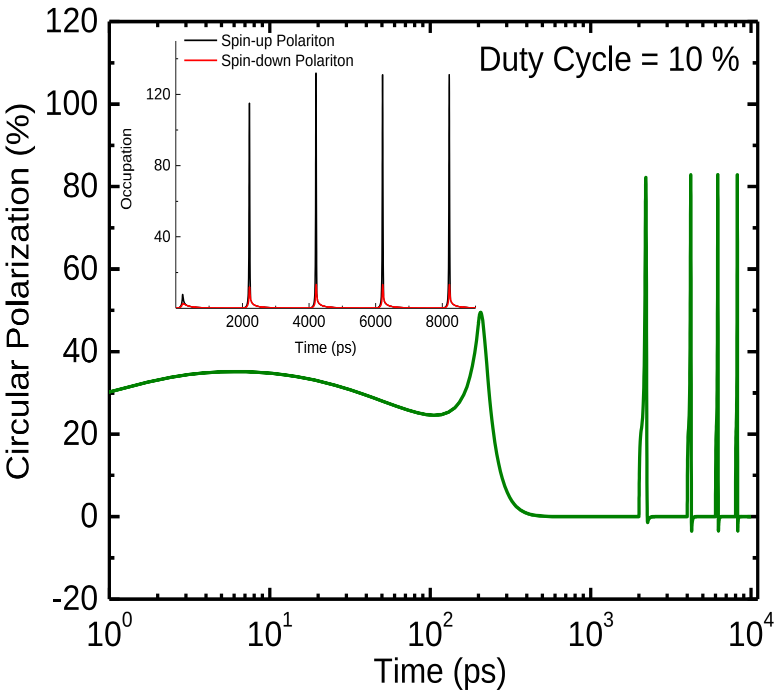

(b)

Figure 6.3 (b) Calculated variation of the degree of the output circular polarization, as a function of time, for the case of excitation with a periodic square pulse having a peak amplitude of 2 kA/cm^2. The biasing pulse has a period of 2 ns and a duty cycle of 10 %. The inset shows the corresponding variation of the two LP components with time.

6.5 Summary

In summary, the output intensity and polarization characteristics of a GaN-based microcavity spin-polarized polariton diode laser in which spin-polarized electrons are injected, have been investigated. Measured data on these devices have been analyzed and theoretical calculations based on a spin-dependent rate equation model have been made. Threshold reduction and enhancement of the output emission as a function of spin injection are demonstrated for the first time. More importantly, the temporal characteristics of the output intensity and circular polarization have been determined and a novel biasing scheme of measuring ~ 100 % output polarization with less than 10 % spin injection is presented. Such a compact low-power coherent light source with a controllable highly circularly polarized output would be useful for many applications.

Chapter VII

Non-Linear Photocurrent Response to Bosonic Final State Stimulation in Microcavity Diodes

7.1 Introduction

The phenomenon of polariton lasing, which is essentially a second-order phase transition from a classical thermal distribution (mixed state) to a macroscopic, degenerate and coherent pure state of exciton-polaritons, originates from the action of bosonic final-state stimulation [4]. This inversionless laser action can also be considered as a highly non-equilibrium and kinetically driven condensation process. The phenomenon of bosonic final-state stimulation, as described in Chapter II, enhances the rates of optical processes, such as emission, scattering or energy relaxation, which can potentially magnify the population of bosons distributed over a certain set of states, once the bosonic occupation number per mode, usually centered at $k_{||} \sim 0$ in case of lower polaritons, exceeds unity. This was first convincingly shown in the case of a strongly coupled GaAs-based microcavity, by performing continuous-wave pump-probe measurements. In results reported by Savvidis et al. [96], it was shown that final-state occupation of the ground state can initiate a stimulated energy relaxation process, which brings about amplification of the ground-state polaritons. This bosonic amplification process was efficiently utilized to implement an angle-resonant stimulated polariton amplifier. Measurements revealed that this parametric amplification process could generate single-pass optical gains as large as 100 [96]. Similar experiments were later performed in CdTe-based microcavities, and this bosonic amplification process was again observed [99].

In experiments performed on electrically injected polariton lasers, high-energy electron-hole pairs are initially created by the electrical excitation process. These subsequently thermalize, mainly by acoustic phonon emission, and form exciton-like polaritons, usually with relatively large values of transverse momentum. They then scatter downhill the lower-polariton dispersion curve mainly by polariton-polariton, polariton-phonon and polariton-electron scattering processes. These are all essentially spontaneous energy relaxation processes. However, above a certain value of the injected current density, when the absolute polariton occupation per mode centered around $k_{||} \sim 0$ approaches one, the elastic scattering of two polaritons, one into the ground state and the other into a higher energy state, is considerably augmented due to the above-mentioned bosonic final-state stimulation process [4, 5]. This is also schematically depicted in Fig. 7.1. This stimulated polariton-polariton scattering process is a phase coherent process and functions as the optical gain generation mechanism in these inversionless coherent light sources [4].

In this chapter, indirect evidence for this bosonic amplification process will be furnished by means of optical excitation-dependent photocurrent measurements. Photocurrent measurements on polariton devices have been previously reported [100-107]. Photocurrent spectra recorded from a reverse-biased microcavity diode can directly map the polariton dispersion characteristics [101, 104]. Optical nonlinearity in a similar device due to switching between strong and weak coupling has been reported by Bajoni et al. [102]. Non-linearity in the reverse biased photocurrent due to a blue shift of the lower-polariton (LP) branch into resonance with the optical pump energy and consequent increase in injection efficiency has been reported by Winkler et al. [105]. A change in the slope of the lateral photocurrent, measured in the in-plane direction, was reported by Brodbeck et al. and attributed to a transition from bosonic (polariton) to fermionic (photon) lasing [106]. All these measurements were performed at cryogenic temperatures. In this chapter, the observation of a non-linear dependence of the photocurrent on pumping intensity in a microcavity diode at room temperature is reported, as a new manifestation of bosonic final state stimulation in polariton lasers [9, 96, 108-111]. The excitation density measured at the onset of the non-linearity coincides with the threshold current density for polariton lasing in the same device. This observation also serves as a proof of principle of an optically-controlled low-energy switching device, where the output photocurrent of a reverse-biased GaN-based microcavity diode is controllably switched between a low output current value (or, nominally OFF state) and high output current value (or, nominally ON state), by pulsed optical excitation at normal incidence. A robust, ultra-fast and energy-efficient all-

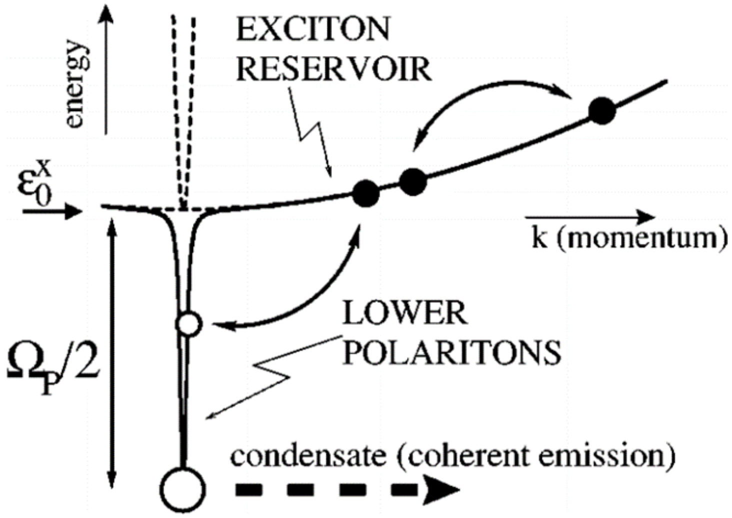

Figure 7.1 Phase space for the scattering of polaritons in a semiconductor microcavity. Upper and lower dashed lines represent the bare photon and bare exciton, respectively. The continuous line is the polariton dispersion that results from the strong exciton-photon coupling. (D. Porras and C. Tejedor, Phys. Rev. B **67**, 161310(R) (2003))

optical, all-electrical or an electro-optical switching device can potentially have a wide range of practical applications in information and signal processing including Application Specific Integrated Circuits (ASICs) and Systems-on-a-Chip (SOCs), on-chip communications and signal routing, control and sensing. The above-mentioned non-linear dependence of the photocurrent on the excitation intensity can be explained in the framework of an Auger-like process of excitonic dissociation into its constituent electron-hole pairs, which can be stimulated by the occupation of the polariton lasing states.

7.2 Summary of Characteristics of the Polariton Microcavity Diodes

The present devices are identical to the polariton diode lasers characterized and reported by in Chapter III, wherein the device processing and the measured characteristics of the lasers have been described in detail. All of these devices originate from the same epitaxial sample and have been processed identically and simultaneously. The defect density in the active region of the devices is $\sim 6.1 \times 10^8$ cm^{-2}. As has been highlighted in Chapters I and III, these devices employ a novel lateral injection architecture, wherein the directions of current flow and polariton emission are mutually orthogonal. This enables the realization of a relatively low series resistance microcavity diode along with a reasonably good quality factor cavity. This is particularly important in the context of the experiments reported in the present chapter, wherein the effects of polariton lasing on the diode current have been studied and are discussed later. Some of the previously discussed polariton lasing characteristics as summarized as follows. The devices are characterized by a cavity photon-to-exciton detuning δ ranging from − 4 to − 13 meV, and a strong coupling in the microcavity characterized by a Rabi splitting Ω of ~ 33.9 to ~ 35.5 meV. The microcavity quality factor Q and the cavity mode lifetime τ_C were found to vary from ~ 1700 to ~ 2100, and from ~ 0.3 ps to ~ 0.4 ps, respectively. The polariton laser thresholds varied from ~ 125 A/cm^2 to ~ 375 A/cm^2. In addition, the onset of non-linear emission was accompanied with the collapse of the LP emission linewidth and a small blueshift of the peak electroluminescence energy. The latter, which is primarily caused by the repulsive self-interaction of the lower-polaritons, is particularly important as it signifies the particulate nature of the radiative species. In contrast, photon lasers do not show any blueshift in their peak emission energy, unless they are injected at very high densities wherein band-filling effects become important. The redistribution of the lower-polaritons in momentum space as a function of injection was also studied. A random and non-thermal LP occupation below threshold was found to transform into a peaked occupancy at $k_{||} \sim 0$ above threshold. In addition, there was no evidence of a polariton relaxation bottleneck at any injection. At threshold, the occupancy was analyzed by a Maxwell-Boltzmann distribution to yield $T_{LP} \sim 270$ K. It was also observed that the emission is unpolarized below the nonlinear threshold and is linearly polarized above it with a maximum polarization of ~ 22%. Conventional cavity mode-mediated photon lasing was also observed in one of the polariton laser devices at an injected current density of ~ 36.8 kA/cm^2. All measurements had been made at room temperature.

Measurements in the present study have been made on two structurally identical microcavity diodes, which we have labeled as Device 1 and 2. The light (output)-current characteristics of the two devices, in the normal direction ($k_{||} \sim 0$), determined by recording the output LP electroluminescence intensities by a photomultiplier tube after spectral filtering through an imaging monochromator, as a function of continuous wave injection current are shown in Fig. 7.2. The peak emission wavelength is $\lambda \sim 367$ nm. The polariton lasing threshold current densities of Device 1 and 2 are ~ 1993 A/cm^2 and ~ 2899 A/cm^2, respectively. The sub-threshold slopes of these characteristics, when plotted in a double logarithmic scale, are ~ 0.45

and ~ 0.48 respectively. These rather small values are indicative of device degradation. Nevertheless, the non-linear slopes above the threshold are ~ 2.95 and ~ 3.68, respectively, which are in reasonably good agreement with the values we have previously observed and reported, for the slopes in the polariton lasing regimes. Device 2 shows slightly stronger non-linearity as compared to Device 1. The observation of a larger polariton laser threshold as compared to what has been previously reported in Chapter III for identical GaN-based devices (~

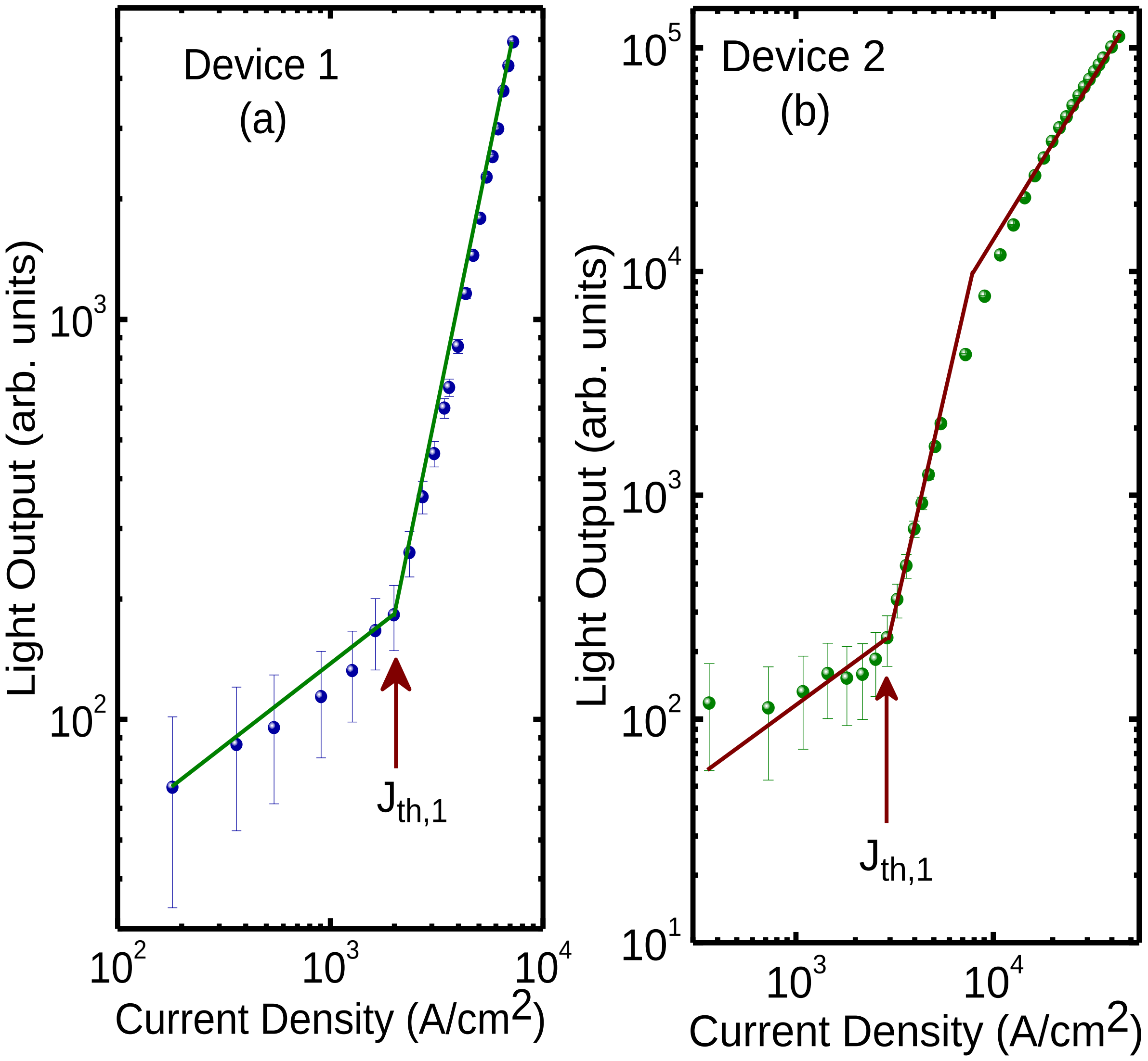

Figure 7.2 LP electroluminescence intensities recorded at zero emission angle (k|| ~ 0), as a function of injected current density, for (a) Device 1 and (b) Device 2, respectively. The solid lines are guides to the eye. The solid vertical arrows indicate the onset of non-linearity.

125 A/cm^2 to ~ 375 A/cm^2) is also indicative of deterioration in the electrical injection process. The increase in the thresholds is, in all probability, a complex interplay of increased density of non-radiative recombination and trapping centers, increased carrier leakage from the active region, and reduction in the carrier injection efficiency at the contacts. This has been taken into account in our theoretical calculations. Nevertheless, as discussed later, the injected carrier density corresponding to the threshold in both of the devices is below the excitonic Mott transition as well as the transparency carrier density in the medium.

7.3 Excitation-Dependent Photocurrent Measurements

Optical excitation-dependent photocurrent measurements are made at room temperature on the polariton lasers under reverse bias. A schematic diagram of the experimental set-up is shown in Fig. 7.3. Measurements have not been made under forward bias, as the diode diffusion current would overwhelm the relatively weaker photocurrent response. The diodes are illuminated at approximately near normal incidence. The excitation is provided by focusing the frequency-doubled output of a pulsed Ti: sapphire laser mode-locked at 80 MHz to a spot size of ~ 10 µm in diameter (by using an UV objective lens) upon one of the device facets. The diode reverse current is recorded with a high-precision digital pico-ammeter having a resolution of ~ 100 fA. The frequency of the excitation laser source was spectrally tuned to coincide with the LP mode energy of ~ 3.378 eV (~ 367 nm) observed at the threshold. This has been done to avoid directly exciting the electron-hole plasma reservoir, which could potentially mask the non-linearity in the photocurrent response from the stimulated excitonic dissociation process, as subsequently discussed. Nevertheless, we do believe that the strong laser background does also bring about true band-to-band excitations in the fermionic reservoir. The blue-shift of the LP mode is not taken into account to spectrally tune the excitation wavelength as a function of incident optical pumping intensity. However, since the spectral linewidth (full-width at half maximum) of the excitation laser is ~ 2.5 nm (or equivalently ~ 23 meV), appreciable excitation of the ground-state lower-polariton (LP) states, which are slightly red-shifted below threshold and very slightly blue-shifted above threshold, takes place. The emission spectrum of the excitation source is shown in Fig. 7.4. The rather broad linewidth of the excitation is a consequence of its pulsed nature. This particular configuration, i.e., of using normal incidence pulsed excitation has been motivated by the desire to examine the device in the context of a more realistic practical situation; it is more convenient to excite a diode at normal incidence to its facets as opposed to any other particular fixed angle of incidence. Further, the combination of the ~ 9 meV (half-width at half maximum) laser tail, along with the angular divergence of the incident beam, should also excite some of the higher energy lower-polariton states. It is certainly

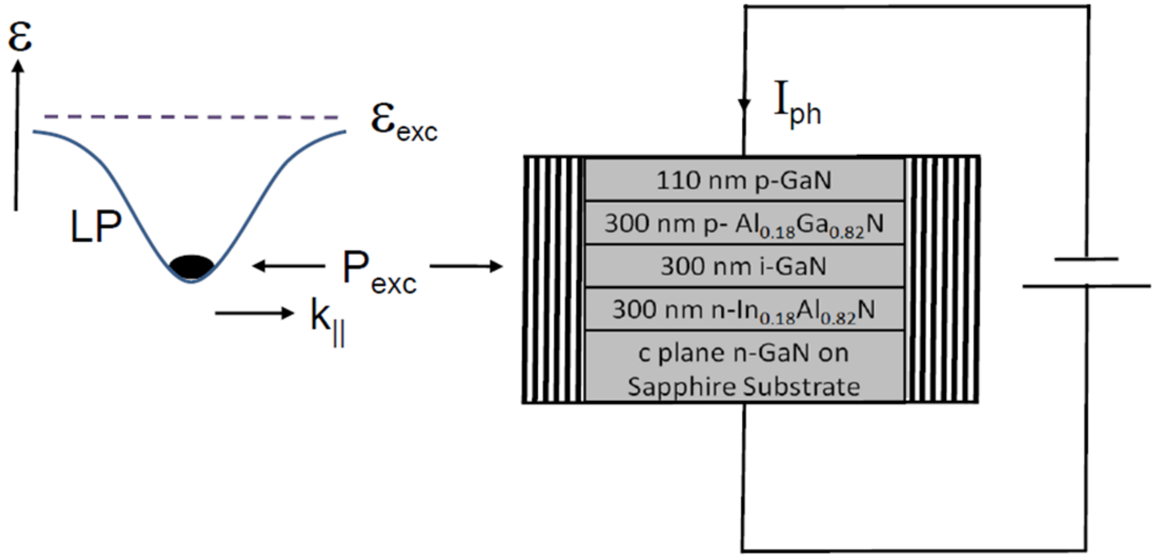

Figure 7.3 A simplified schematic diagram of the experimental set-up for measuring the excitation-dependent photocurrent characteristics.

probable that stimulated scattering from higher energy states along the lower-polariton dispersion to the ground state should be possible in the present configuration, assuming that the

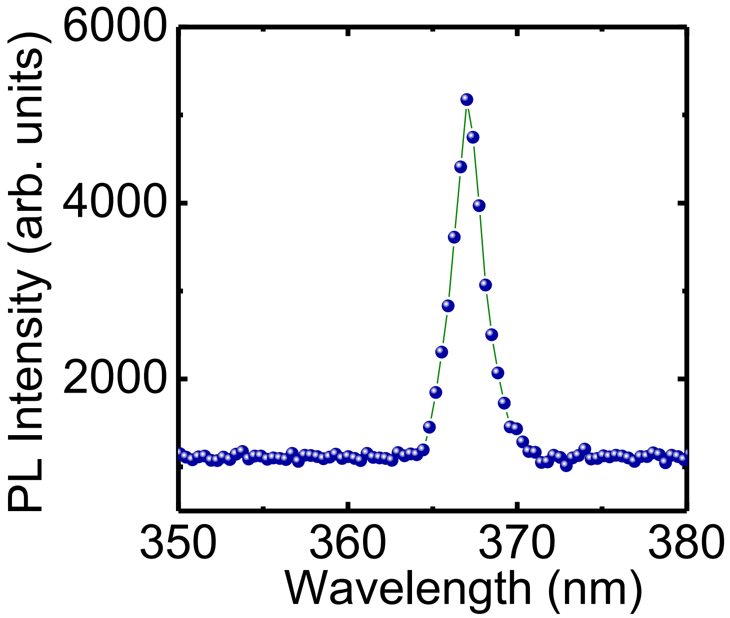

Figure 7.4 Spectrum of the doubled output of the Ti: Sapphire laser used to excite the microcavity diode at near normal incidence.

ground state occupation number is greater than unity, above a certain excitation value. The excitation-dependent output photocurrent characteristics of Device 2 are shown in Figs. 7.5 (a) and (b) for different values of the applied reverse bias. It can be observed that there is a non-linear enhancement of the absolute magnitude of the photocurrent at incident optical pump powers I_p ~ 1.6 mW. This effect is most clearly manifested at values of reverse biases of ~ 0.1 and 0.2 V. At higher values, the non-linearity starts getting obscured by the increased magnitude of the dark current of the diode. The photocurrents plotted in Figs. 7.5 (a) and (b), are the as-measured values. It should be emphasized that these currents are the true reverse currents flowing through the diodes, originating from photo-generated carriers which diffuse to the depletion region, wherein they are accelerated and are finally collected at the ohmic contacts of the device. Thus, these measurements are different from those reported by Brodbeck et al. [106], wherein a lateral photocurrent, proportional to the in-plane quantum-well carrier density, is

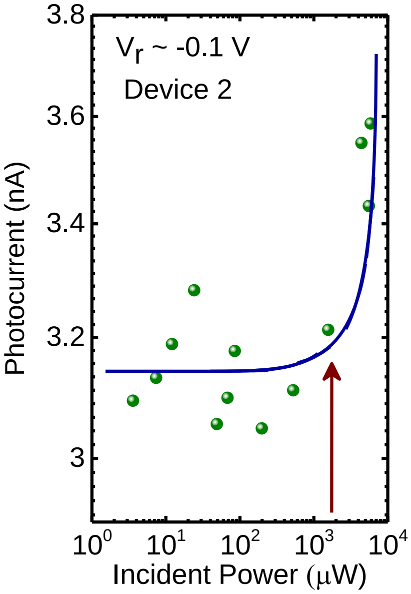

(a)

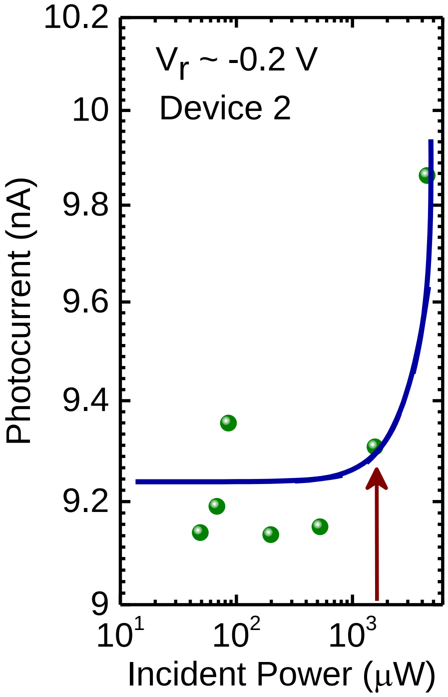

(b)

Figure 7.5 Measured photocurrent response as a function of incident optical pump power for (a) Device 2 at a reverse bias of ~ 0.1 V and (b) Device 2 at a reverse bias of ~ 0.2 V. The solid lines are guides to the eye. The solid vertical arrows indicate the onset of non-linearity.

collected by Schottky contacts formed across the device active region. The pump powers at the onset of photocurrent non-linearity correspond to a LP density N_{3D} ~ 3 X 10^{16} cm^{-3} , estimated with the relationship: $N_{3D} = (1-R_{NI})A_{NI}I_p/(f_p\hbar\omega\pi r^2 L)$ [13] where R_{NI} is the cavity reflectance at normal-incidence of the strongly coupled microcavity estimated to be ~ 0.9, A_{NI} is the overall conversion efficiency of the incident photons to intra-cavity polaritons at normal incidence estimated to be ~ 0.46 as discussed later, I_p is the incident pump power, f_p is the incident optical excitation repetition rate of the mode-locked laser ~ 80 MHz, $\hbar\omega$ is the energy of the pump photons ~ 3.378 eV at the LP ground-state energy, r is the radius of the pump spot size ~ 5 µm and L is the device cavity length ~ 690 nm. This value of N_{LP} is lower than the transparency density of ~ 10^{18} m^{-3} [112] and the exciton Mott density of ~ 10^{19} cm^{-3} in GaN [113] by two and three orders of magnitude, respectively. Excitation-dependent photocurrent measurements were also performed on Device 1, in the same manner as has been described earlier for Device 2. The data are shown in Fig. 7.6. The onset of the non-linearity in the photocurrent response is at an incident optical power I_p ~ 1 mW. The non-linearity in the output photocurrent response is relatively weaker as compared to that observed in Device 2. This is probably due to the fact that the non-linearity in this particular device is inherently weaker, as compared to that in Device 2.

7.4 Interpretation of the Results

In all probability, the observed non-linearity in the photocurrent is related to the onset of stimulated scattering and polariton lasing triggered by the optical excitation. Preliminary calculations, in progress at the time of composition of this dissertation, show that the non-linear thresholds in the light-current and excitation-dependent photocurrent characteristics are essentially identical. To obtain this correspondence between the two thresholds, one has to only tune the values of two parameters to obtain R_{NI} ~ 0.9 and A_{NI} ~ 0.435. Both of these values are quite reasonable. The former corresponds to the averaged reflectance as seen by the incident wideband pump, while the latter is the overall absorbance inside the cavity. This gives an averaged effect because of absorption in the LP band and also probably some residual absorption in the free carrier reservoir.

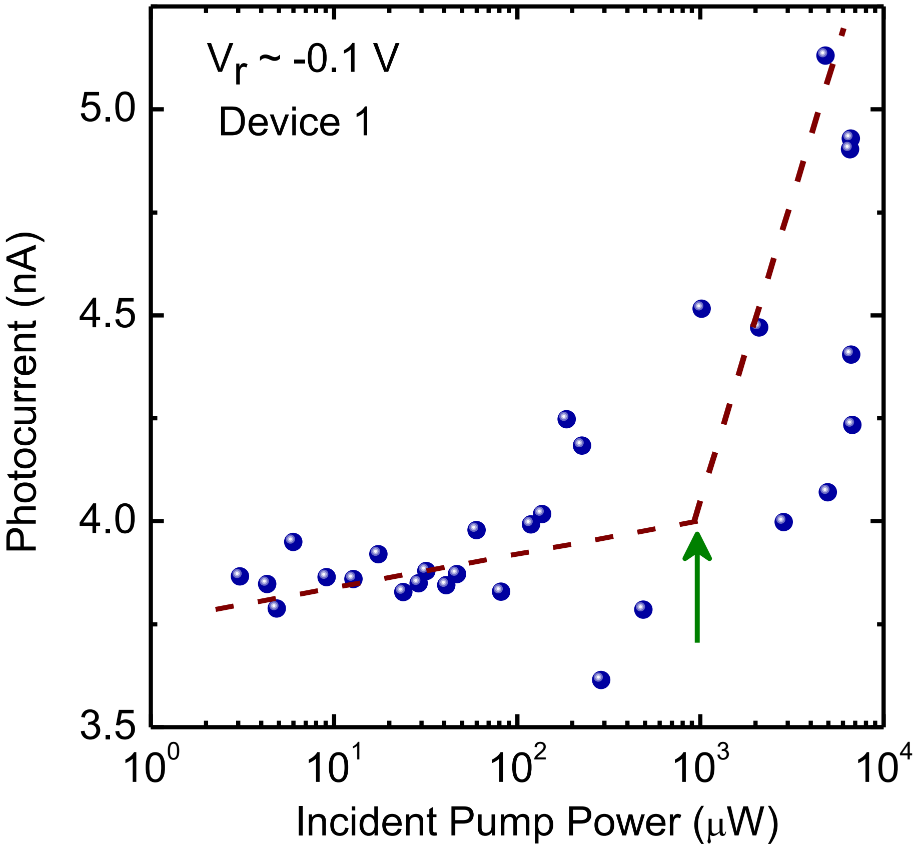

Figure 7.6 Measured photocurrent response as a function of incident optical pump power for Device 1 at a reverse bias of ~ 0.1 V. The dashed lines are guides to the eye. The solid vertical arrow indicates the onset of the non-linear photocurrent response at ~ 1 mW.

In what follows, a viable approach for theoretically modeling these observed phenomena and analyzing the excitation-dependent photocurrent characteristics is discussed. A set of coupled rate equations for the free electron-hole plasma reservoir, excitonic reservoir and the polaritons lasing states has to be devised which should include two relevant stimulated scattering terms. These terms would physically correspond to the non-linear growth of the ground-state polaritons as well as that of a fraction of the electron-hole plasma reservoir, originating from the dissociation of the high-momentum exciton-like polaritons (Fig. 7.7). The latter originates from the stimulated polariton-polariton scattering process, and corresponds to the polaritons which are scattered to the higher energy states to conserve energy and momentum. This picture would

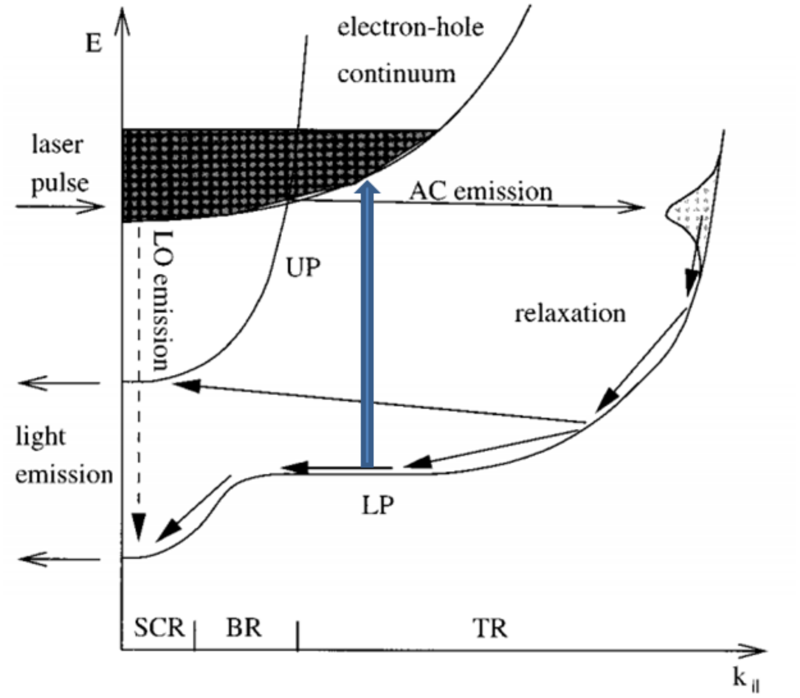

Figure 7.7 A schematic diagram of the dispersions valid in the strong-coupling picture, showing one dissociative pathway which can populate the conduction and valence bands at the expense of high-momentum exciton-like polaritons. The solid blue vertical arrow indicates the dissociation process. This diagram is adapted from F. Tassone et al., Phys. Rev. B **56**, 7554 (1997).

explain the measured data discussed in Section 7.3 of this chapter. It must be emphasized that the non-linear increase in the photocurrent flowing through the diode, originates from a non-linear increase in the free carrier occupation numbers. Excitons and exciton-polaritons are charge-neutral quasiparticles and cannot directly contribute to the flow of a current. This behavior should not be observed at the photon lasing threshold, as the total carrier density becomes clamped at the onset of threshold. It is probable that the appreciable background free carrier concentrations (~ 10^{16} cm^{-3} - ~ 10^{17} cm^{-3}) in these GaN-based microcavities, along with the fact that the excitonic binding energy (~ 28 meV) is relatively close to k_BT, aids in the dissociation process of the high-momentum excitons.

7.5 Conclusions

In conclusion, the present chapter reports on the optical excitation-dependent output photocurrent characteristics of GaN-based polariton diode lasers operated under reverse-bias at room temperature. The photocurrent demonstrates a non-linear enhancement at an incident optical power of ~ 1.6 mW, which is approximately equivalent to the value of polariton lasing threshold observed when the diodes are operated under forward bias conditions. This is explained in the framework of an Auger-like (non-radiative) process of excitonic dissociation into its constituent electron-hole pairs, which can be stimulated by the occupation of the polariton lasing states and the observed effect is therefore a unique manifestation of the bosonic final state stimulation in polariton lasers. A model based on the coupled kinetic equations for the free carriers, the excitonic reservoir and the polariton lasing state shows the same overall trend as observed in the experimental data, is being devised presently at the time of composition of this dissertation.

Chapter VIII

Conclusions and Future Works

8.1 Summary of The Present Work

The present dissertation was chiefly concerned with the elucidation of the output optoelectronic and spin-optronic characteristics of GaN-based microcavity polariton laser diodes operated with and without spin-polarized electrical injection. A microcavity polariton laser diode designed in the form of a conventional in-plane Fabry-Perot semiconductor laser diode, enables room-temperature operation of electrically injected GaN-based double heterostructures. This is because of the feasibility of efficient current injection orthogonal to the axis of cavity resonance, thus enabling a relatively low series resistance pathway for the injected electrons. Electrical injection through thick III-nitride-based materials, as would be necessary in surface-emitting geometries, is highly inefficient because of problems of adequate doping of the mirror layers and residual strain and defects in these mirrors. Thus, the overall diode series resistance is increased which exacerbates Joule heating and increases the GaN lattice temperature. In contrast, the side-emitting geometry also allows for the n-type contacts of the electroluminescent devices to be replaced by in-plane magnetized ferromagnetic tunnel contacts, enabling the operation of spintronic optoelectronic devices in the absence of any external ambient magnetic field. A spin polariton laser diode, driven by spin-polarized electrical excitation, emits controlled circularly polarized light. Previous experiments and theoretical work on the nature of the output polarization from polariton lasers, have established the variable, highly unstable and essentially uncontrolled nature of circular polarization emitted by these devices. The previous methods of obtaining highly circularly polarized light in these structures, have included applying a large magnetic field in the Faraday geometry (Zeeman splitting) as well as exciting with a highly circularly polarized light source.

The present work has shown an elegant mechanism of generating relatively large degrees of output circular polarization (~ 25 %), by using in-plane ferromagnetic tunnel contacts. The value and direction of magnetizing field used to magnetize the contacts prior to operation, directly control the helicity and magnitude of the degree of circular polarization of the emitted light, above the laser threshold. It is also theoretically shown how this value of the degree of the circular polarization can be made almost unity, with the present device configuration. However, successful operation of these spintronic polariton lasers is contingent on successful injection of spin-polarized electrons. Thus, the present dissertation also contains work on the study of spin injectors directly deposited on bulk n-type GaN, which acts as the cathode-type contact layer of the device heterostructures. This is critical to the successful operation of these devices as the controlled circular polarization in the output coherent emission originates entirely from the injected spin polarization at the interface of the n-type GaN contact layer and the ferromagnetic contact. Successful electrical spin injection in bulk GaN, which is also the active layer of the polariton diode laser, has been independently confirmed from room-temperature four-terminal

Hanlè spin precession measurements made on GaN-based spin valves, and observation of hysteretic circular polarization in edge-emitting III-nitride light-emitting diodes. The optical selection rules governing the operation of the latter have also been elucidated. Electrical injection of spin polarized electrons is accomplished in all the above-mentioned devices via a n-type FeCo/MgO spin injector contact. All of the above-mentioned experiments pertaining to electron spin injection in GaN-based devices, have been made at room temperature.

The primary focus of the first two chapters of the dissertation has been an introduction to strong-coupling characteristics in semiconductors, in general and in GaN, in particular. The nature of polariton lasing and its salient differences from conventional photon lasing was also discussed. Chapter III concentrated on an experimental and theoretical analysis of the steady-state output linear polarization characteristics of GaN-based polariton lasers operated with conventional electrical injection. Measurements of sub-threshold angle-resolved electroluminescence spectra have been carried out to ascertain the strong-coupling regime of operation of these devices. Polariton lasing has been verified from measurements of output-light characteristics, zero-angle spectral characteristics and from the redistribution of the polaritons in the momentum ($k_{||}$) space, as a function of injection. The steady state output polarization characteristics of GaN-based microcavity polariton lasers operated with electrical injection at room temperature, was also reported. The output is essentially unpolarized below the non-linear threshold injection current and is linearly polarized above it with a maximum degree of polarization of ~ 22 %. The results have been analyzed theoretically and the calculated results are in agreement with the measured data. The linear polarization resolved output light-current characteristics have also been measured, wherein a distinct lowering of the non-linear threshold is observed in one device. This is interpreted in terms of spatially inhomogeneous lifting of degeneracy and polarization splitting in the microcavity.

The focus of chapter IV was the study of the feasability of electron spin injection in bulk n-type GaN. Measurements of electron spin injection, coherent transport and detection were made at room temperature by purely non-local electrical measurements. The measurements of diffusive electronic spin transport characteristics in epitaxial bulk wurtzite GaN lateral spin valve at room temperature, have been reported at room temperature. Hanle spin precession and non-local spin accumulation (magnetoresistance) measurements have been performed with the spin valves fabricated with FeCo/MgO spin contacts. Electron spin relaxation length and spin-flip lifetime of ~ 176 nm and ~ 37 ps, respectively, are derived from analysis of results obtained from four-terminal Hanle spin precession measurements at 300 K. To further ascertain the feasibility of transduction of injected electron spin polarization to output circular polarization, a spin-polarized light-emitting diode was designed and processed. Room temperature circularly polarized electroluminescence is observed from these bulk GaN-based double-heterostructure edge-emitting light emitting diodes operated with continuous-wave spin-polarized electrical injection. The measured in-plane magnetizing field-dependent output circular polarization in the quasi-Voigt geometry is coincident with the hysteresis characteristics of the spin-injector confirming electron spin injection in remanence from the n-type FeCo/MgO tunnel spin contacts. A peak output circular polarization of ~ 6 ± 1 % is measured at 300 K. After the discussion of the above-mentioned demonstration of appreciable spintronic and spin-optronic effects in GaN, the next chapter then details the study of the room-temperature operation of a spin polariton diode laser. Chapter V discussed the demonstration of a room temperature spin polariton diode laser. The principal advantage of a spin-polarized laser, over conventional lasers, is that the former offers inherent control of the output circular polarization. Thus, the output polarization characteristics of a bulk GaN-based microcavity polariton diode laser were investigated at room temperature with electrical injection of spin polarized electrons via a FeCo/MgO spin injector. Polariton laser operation with a spin polarized current is characterized by a threshold of ~ 69 A/cm^2 in the light-current characteristics, a significant reduction of the electroluminescence linewidth and blueshift of the emission peak. A degree of output circular polarization of ~ 25 % is recorded under remanent magnetization. A second threshold, due to conventional photon lasing, is observed at an injection of ~ 7.2 kA/cm^2. The variation of output circular and linear polarization with spin-polarized injection current has been analyzed with the carrier and exciton rate equations and the Gross-Pitaevskii equations for the condensate and there is good agreement between measured and calculated data.

Chapter VI detailed further theoretical analysis of the spin polariton diode laser discussed in the previous chapter. Optical effects arising from spin-induced gain anisotropy such as threshold reduction and emission intensity enhancement, hitherto unobserved in electrically injected polariton lasers, are theoretically predicted for a bulk GaN-based exciton-polariton diode laser operated with electrical injection of spin-polarized electrons. These phenomena are deduced from a simplified spin-dependent rate equation model. An electrical excitation scheme, which can amplify the degree of a deterministic circular polarization of the output emission by an order of magnitude, compared to the injected electron spin polarization, above threshold, is also discussed. The spin-dependent rate equation model discussed in the present chapter, is different from that presented in the previous chapter. In this chapter, directly the absolute occupation numbers or particle concentrations have been used in the equations rather than employing the coupled stochastic differential equations of the previous chapter. An advantage of the same is the fact that no additive white Gaussian noise term has to be explicitly added to the equations, resulting in a smooth evolution of the calculated polariton occupation numbers with injection. This enables the observation of any small changes in the polariton laser thresholds with differences in the injected electron spin polarization, which could have been potentially masked if the theoretical approach of the previous chapter had been employed.

Chapter VII described the optical excitation-dependent output photocurrent characteristics of GaN-based polariton diode lasers operated under reverse-bias at room temperature. The photocurrent demonstrates a non-linear enhancement at an incident optical power of ~ 1.6 mW, which is approximately equivalent to the value of polariton lasing threshold observed when the diodes are operated under forward bias conditions. This is explained in the framework of an Auger-like (non-radiative) process of excitonic dissociation into its constituent electron-hole pairs, which can be stimulated by the occupation of the polariton lasing states and the observed effect is therefore a unique manifestation of the bosonic final state stimulation in polariton lasers. A model based on the coupled kinetic equations for the free carriers, the excitonic reservoir and the polariton lasing state shows the same overall trend as observed in the experimental data, is being devised presently at the time of composition of this dissertation.

8.2 Future Work

8.2.1 Non-Linear Output Characteristics in Between Polariton and Photon Lasing Regimes.

8.2.1.1 Introduction

The work presented in this dissertation has mainly focused on III-nitride based polariton laser diodes. One of the major drawbacks of these coherent light sources is the relatively low output optical power levels. The emitted optical power per facet for the Device 1, characterized in Chapter III and also shown in Fig. 8.1 on next page, at an injected current density of ~ 500 A/cm^2 is ~ 1µW. This corresponds to an emitted optical power density is ~ 8.3 W/cm^2. Further, an injected current density of ~ 500 A/cm^2 corresponds to an equivalent diode current of ~ 200 µA. Taking into account the fact that the corresponding diode voltage is ~ 3.0 V, an optical power conversion efficiency is ~ 0.17 % is estimated, which corresponds to a wall-plug efficiency of ~ 0.55%. A plot of the differential slope efficiency as a function of injection, along with the corresponding light-current characteristics from which the data are derived, are shown in Fig. 8.1. In contrast, the best reported optically triggered GaN polariton lasers have output powers of ~ 80 µW at 4 mW incident pump power (~ $4I_{th}$). Thus these polariton laser diodes would potentially have limited applications. Although, they would be extremely useful in niche applications requiring low-power coherent light sources such as some biomedical applications, nevertheless for widespread applicability and real-world commercial applications, high-power lasers are required.

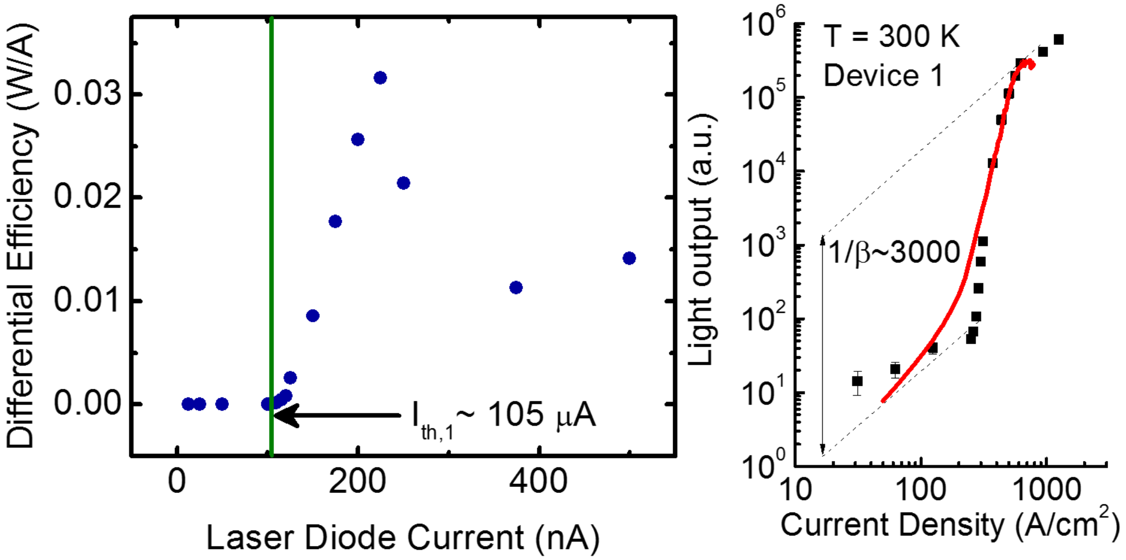

(a) (b)

Figure 8.1. (a) Differential slope efficiency and (b) spectrally resolved output electroluminescence as a function of excitation for a polariton laser diode operated with conventional unpolarized electrical injection.

These problems also plague the spin polariton laser diodes. Although they have relatively small threshold current densities (~ 69 A/cm^2 ─ ~ 181 A/cm^2), their output power levels are also quite low. A room temperature spintronic photon laser would combine the advantages of these spin polariton lasers along with relatively large output power levels. Also, a second non-linearity has been observed in the weak coupling regime of operation of these spin polariton devices, most possibly due to population inversion and photon lasing, is observed at J ~ 7.2 kA/cm^2, as shown in Chapter 5. With this motivation, the output emission characteristics of these spin polariton devices has been studied under conditions of high excitation, in order to potentially observe photon lasing and study its characteristics in great detail. The output emission and spectral characteristics in the photon lasing regime could not be studied in detail in Chapter V, even under pulsed excitation conditions, because of the irreversible damage to the contacts beyond an injection of ~ 7.5 kA/cm^2, which open-circuited the diode. Spin polariton devices which are essentially identical to those reported in Chapter V and processed under identical conditions were chosen for the measurements. Thus, these diodes have a GaN-based double heterostructure epitaxially grown on a p-type GaN-on-sapphire epitaxial substrate. The n-type contacts are the CoFe/MgO ferromagnetic tunnel contacts. They also originate from the same epitaxial wafer as those reported in Chapter V. However, there is one fundamental difference between those devices and the ones reported in this Chapter. Several devices, whose cavity lengths were ~ 1 µm, were chosen for these measurements. These are devices, wherein the focused ion beam milling process employed to define the cavity length was prematurely terminated to obtain a length of ~ 1 µm instead of ~ 690 nm as in the usual devices. Thus, these should be more promising for demonstration of conventional photon lasing because of their lower mirror losses by virtue of their longer cavity lengths. It may be noted that neither any strong-coupling nor polariton emission characteristics were observed in these devices. This may be due to the longer cavity length which translates to a larger active mode volume or because of a degradation in the active regions of these devices, as result of which the free excitonic resonance(s) becomes broadened and quenched. In contrast to the devices characterized in Chapter V, the diodes studied in the present chapter showed signs of degradation because of migration of Mg atoms from the p-type doped layers to the nominally intrinsic active regions. The latter may be due to degradation due to aging or because of accelerated migration of Mg acceptors because they have been operated under high excitation conditions.

This particular section shall discuss observations of a significant nonlinearity in the output emission characteristics without any accompanying observations of coherence in the electroluminescence spectra or the excitation-dependent steady-state circular polarization characteristics. This is observed at an injected current density of ~ 5 kA/cm^2, which corresponds to a regime in between strong coupling and transparency. Two possible reasons which could explain the observations have been furnished and the most probable one is discussed. It is probable that the excitation regime of large nonlinearity is commensurate with the abrupt activation of a resonant tunneling pathway which enhances the electron injection efficiency into the device heterostructure. The tunneling process takes place, most probably through the MgO tunnel barrier of the solid-state electron spin injector. Detailed theoretical and numerical investigations are underway at the time of composition of the present dissertation and any such mathematically advanced explanations is presently beyond the scope of the present chapter.

8.2.1.2 Current-Voltage Characteristics

Steady-state continuous-wave (cw) measurements were made to ascertain the electrical characteristics of the devices under consideration. Although clear rectifying characteristics were observed, the diodes were highly resistive. The typical value of threshold (turn-on) voltage of the devices is ~ 5 V, whereas the differential resistance dV/dI is ~ 306 kΩ (for example, for Device 4) at 10 V bias. The differential resistance, as ascertained from the slope of the I-V curves, falls with increasing injection. A value of differential resistance of ~ 5.5 kΩ (for Device 3) and ~ 7 kΩ (for Device 4) at 40 V is estimated, which is the highest value of cw bias which has been applied to these devices. Thus to avoid detrimental effects of Joule heating, the devices have been characterized under pulsed bias conditions. Further, the device mounts were actively cooled using a thermoelectric cooler. The temperature of the base upon which the devices were mounted using double-sided copper tapes, was maintained at 0 ^{0}C. Nevertheless, during the actual device operation, the lattice temperature of the device active region as well as the facet temperature was most certainly above 300 ^{0}C. All the measurements are made at remanence, after the ferromagnetic tunnel contacts have been magnetized with an in-plane H ~ + 1.6 kOe.

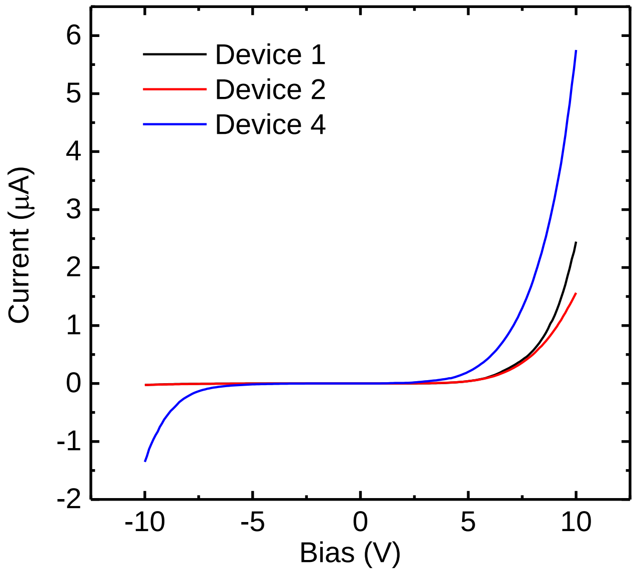

(a)

Figure 8.2. Room temperature current-voltage characteristics recorded under the biasing regime (a) encompassing from -10 V to +10 V,

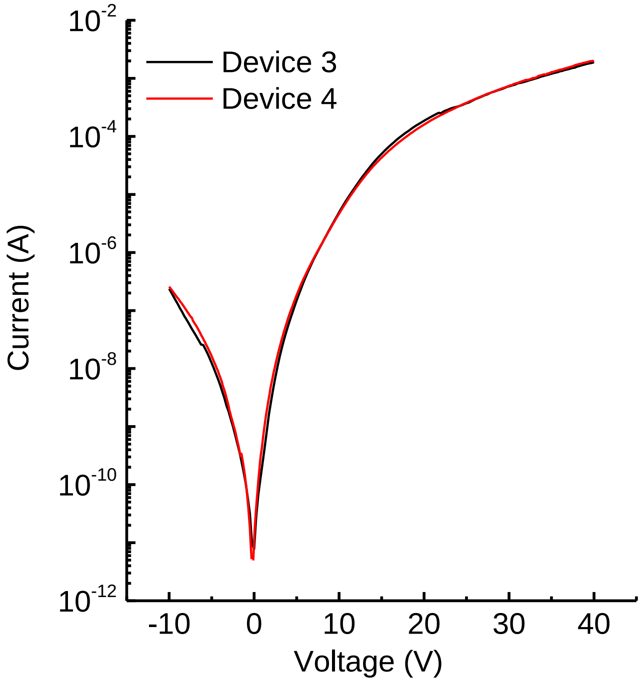

(b)

Figure 8.2. Room temperature current-voltage characteristics recorded under the biasing regime (b) ranging from -10 V to + 40 V.

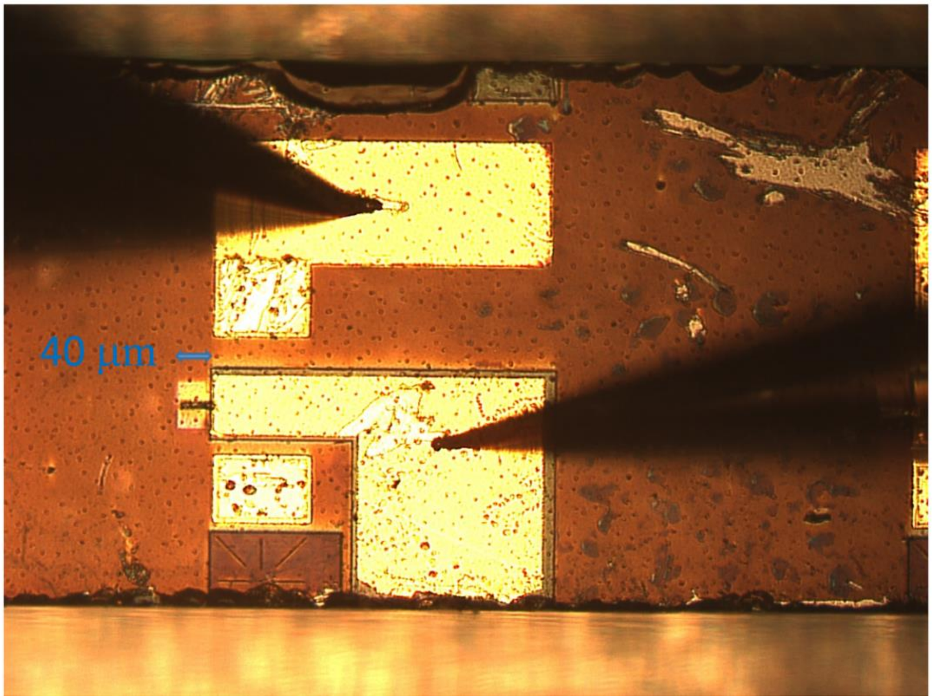

Figure 8.3. Photomicrograph of one of the devices from which the nonlinearity in the output characteristics was observed. The blue scale bar which accompanies this figure indicates the width of the device (~ 40 μm).

8.2.1.3 Light (Output)-Current Characteristics

The results discussed below in this section are obtained from conventional light-current measurements made on one single device, which shall be referred to as Device 1, subsequently. Because of the rather extreme measurement conditions (high diode voltage and current) to which these devices are subjected, all of the measurements could not be made on the same device. Usually, the reason for the termination of measurements on one particular device is the irreversible destruction of the n-type ferromagnetic contacts. The output electroluminescence intensities, spectrally resolved at ~ 380 nm, are plotted as a function of the diode current. The light output emitted in a direction normal to the plane of the dielectric Bragg reflector (DBR) mirrors was collected and transmitted by a 600 µm core diameter Ocean Optics laboratory-grade optical fiber patch cord to a 0.75m Czerny-Turner imaging monochromator. All the measurements have been made at room temperature. All the measurements were made under pulsed biasing conditions. The best and most consistent results are obtained by employing an excitation repetition rate of 100 kHz and a duty cycle of 5 % (pulse ON time of ~ 500 ns). This ensured that the devices did not get appreciably heated and the recorded intensities were at least 1000 times greater than the ambient noise floor of the photomultiplier tube. Results from two independent sets of measurements made on the same device are shown in Fig. 8.4.

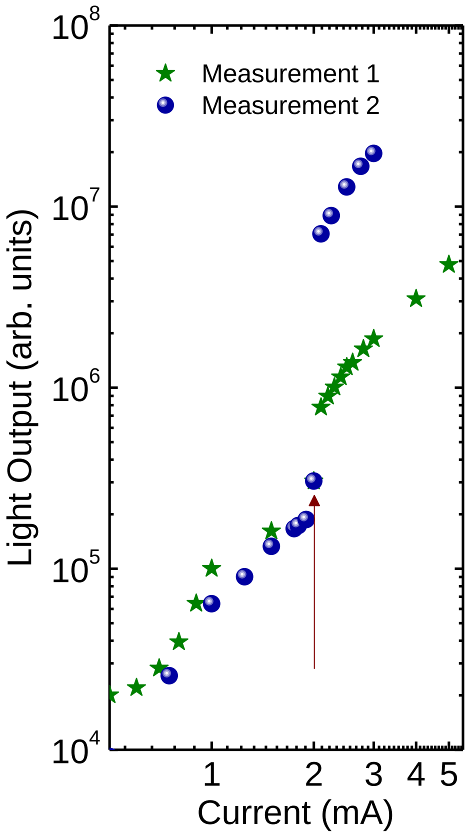

Figure 8.4. Light (output)-current characteristics of the same diode recorded on two different days. The electroluminescence intensities have been renormalized to make them coincident at the onset of non-linearity (indicated by the vertical arrow). Measurement 2 employed adequate measures to cool the devices in between recording subsequent data points and also used better data averaging measures.

This non-linearity is observed not only in the same device under independent measurements as shown in Fig. 8.4, but also in multiple essentially structurally identical devices. This is observed independent of the detector settings, the monochromator settings and it also have been verified that it is not caused by the electrical excitation scheme. The light-current characteristics of a light-emitting diode, emitting at ~ 420 nm, have also been recorded using the same pulsed current source (Keithley 6221A DC and AC Current Source) and no such non-linear behavior at ~ 2 mA, is observed. The corresponding data are shown in Fig. 8.5. This rules out any possible artifacts in our pulsed biasing circuitry.

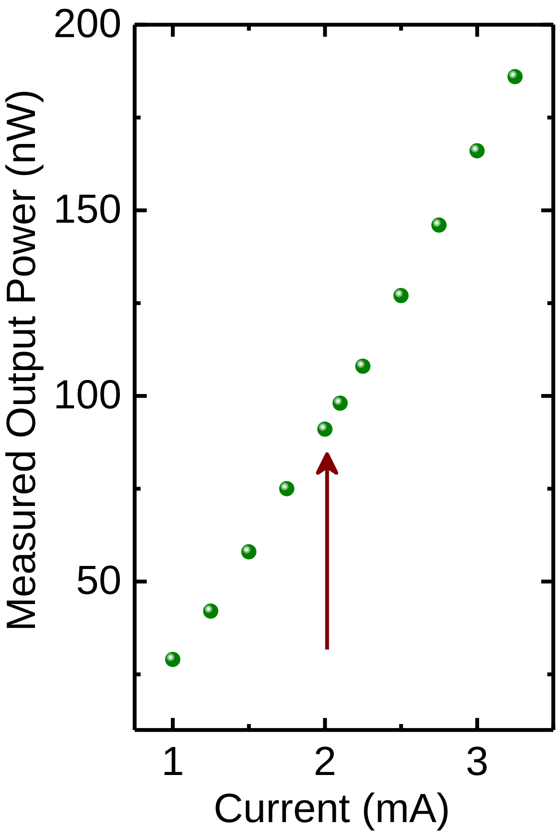

Figure 8.5. Light-current characteristics of a different light-emitting diode, emitting at ~ 420 nm, characterized using the same pulsed current source. The excitation repetition rate was kept fixed at 100 kHz, however the duty cycle had to be increased to 50 % to obtain appreciable amounts of output power at the detector.

8.2.1.4 Steady-State Circular Polarization Measurements

Circular polarization-resolved light (output)-current characteristics were recorded to ascertain the injection dependence of the degree of the output circular polarization. This was performed to ascertain whether the large degree of enhancement of the output electroluminescence at ~ 2 mA originates from some effect which brings about a sudden enhancement of the spin-polarized tunneling process through the ferromagnetic tunnel contact. Any abrupt change in the value of the injected electron spin polarization should be reflected in the output circular polarization value. The measurements are made using the conventional Stokes polarimetry arrangement, which has been discussed in Chapters IV and V. Figure 8.6 shows the left-hand circularly polarization (LHCP)-resolved output of Device 1 and the two circular polarization-resolved outputs of Device 2. As can be observed from the measured data, all the three independent curves show a characteristic jump at ~ 2 mA. The injection dependence of the degree of the output circular polarization, as derived from the data for Device 2, does not show any clear trend with increasing injection. Independent control measurements have been made which reveal a background circular polarization of ~ + 4.3 % (RHCP) in the measurement set-up. These measurements have made with a laser source emitting at ~ 365 nm. Since all the values of the degree of the output circular polarization are smaller than ± 4.6 %, in all probability the output emission is essentially unpolarized. This is in agreement with independent observations in spin-polarized incoherent light sources, wherein a reduction in the output circular polarization has been observed with increasing tunnel junction bias. Thus, there is probably negligible efficient spin-polarized or spin selective tunneling at such high biases. Further, it is also certainly possible that the magnitude of the injected electron spin polarization is insufficient to overwhelm the various spin relaxation processes which the spin-polarized electrons undergo during their diffusive transport to the device active region.

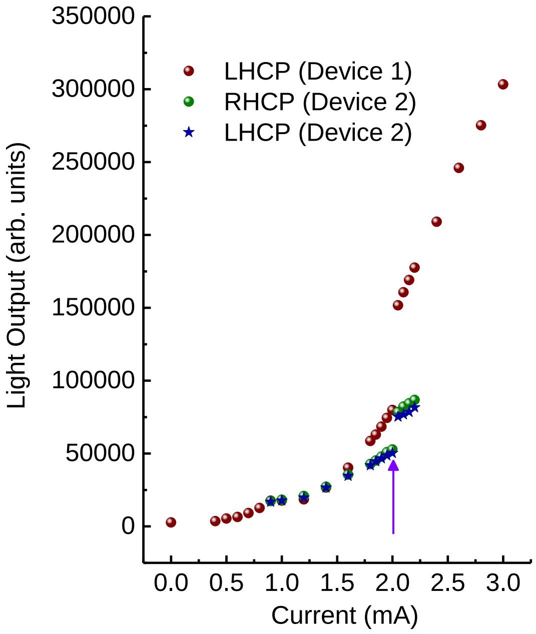

Figure 8.6. Circular polarization-resolved light (output)-current characteristics of Device 1 and Device 2. The metallic contacts of Device 1 underwent irreversible destruction after the conclusion of the LHCP measurements, and thus the other measurements had to be made on a different device (Device 2).

Some drawbacks of the methodology by which the circular polarization data have been measured will be provided as follows. The device electroluminescence was collected and transmitted by a multimode optical fiber. A 5-meter long laboratory-grade optical fiber patch cord has been used to transmit the luminescence to the entrance slits of the monochromator. Since, the measurement employs a fiber to collect the emitted electroluminescence, it is probable that the determination of the value of the circular polarization is not very accurate, since multimode fibers are birefringent and thus will possibly affect the polarization state. Further, no polarization compensator (triple-coil or Babinet-Soleil) have been used as well. To understand the role of the same, control experiments were performed using a 0.5-meter optical fiber and the same monochromator. The excitation source was a highly linearly-polarized laser source emitting at ~ 365 nm. From these experiments, an overall background circular polarization of ~ + 4.3 % (RHCP) has been observed, which takes into account birefringence and circular dichroism effects in various parts of the measurement set-up, such as the fiber and the gratings of the monochromator, wherein such effects are probably the most pronounced.

8.2.1.5 Spectral Characteristics of Device 3

The output spectral characteristics of one particular diode, Device 3, shall be investigated for consistency. Device 1 was destroyed before its output spectral characteristics were recorded. Figure 8.7 shows the electroluminescence spectra recorded as a function of injection. The spectral resolution was ~ 3.16 nm, corresponding to fully open entrance and exit slit widths. A supply voltage of 1250 V (anode to cathode) was applied to the photomultiplier tube (Hamamatsu Photonics R928) and an integration time of 300 ms was used. All the data plotted in Fig. 7.7 were recorded under 5 % duty cycle excitation conditions. It is striking that there is no appreciable change in the peak emission wavelength with increasing injection. This has been said to be characteristic of DAP-type recombination emissions. All of the spectra, independent of excitation, show a strong low-wavelength tail. The rather curious and unusual nature of the spectral output entails further detailed examination. Before the present chapter moves onto more detailed examination of spectra, the relatively low-resolution spectra (corresponding to ~ 100 µA of injection), shown in Fig. 8.7, which could be recorded with a satisfactory signal-to-noise ratio are first studied. Measurements made with the devices turned off, also confirm that there are no strong electroluminescence artifacts or spuriously coupled emissions which are distorting the lineshapes.

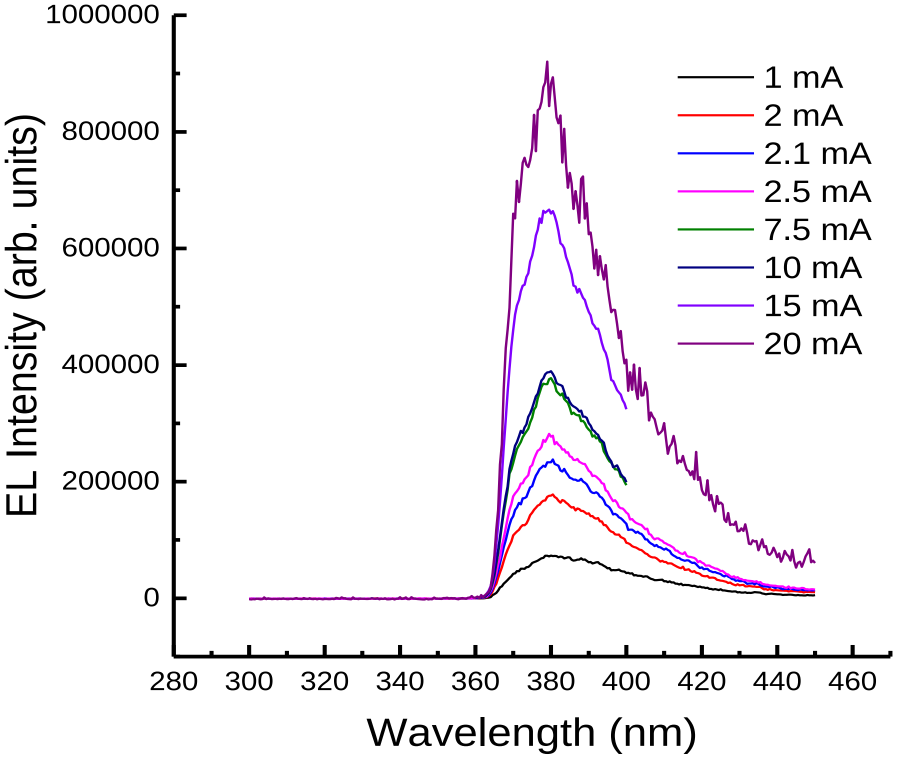

Figure 8.7. Electroluminescence spectra recorded as a function of injection. All of the data, except for the 20 mA spectra, were recorded with 300 ms integration time. The 20 mA data were acquired with 10 ms integration time.

An analysis of the ~ 100 µA spectra, for example, as a convolution of Gaussian resonances shows 4 distinct peaks. The overall spectrum is centered at ~ 381.5 nm and has a full width-at-half-maximum (FWHM) of ~ 34 nm. It should be kept in mind that the spectral resolution of the acquisition itself has a resolution of ~ 3.16 nm. The strongest constituent Gaussian resonances are centered at ~ 377.5 nm and ~ 388.5 nm, with linewidths (FWHM) of ~ 12.4 nm and ~ 22.7 nm, respectively, of which the latter is broader and has a larger integrated area of the two. This is certainly intriguing, given the fact that strong non-linearity has been observed in L-I measurements in which the light output at ~ 380 nm was spectrally resolved. To resolve the issue, all of the spectra which have been acquired over the same spectral range, have been analyzed. It is seen that all of the data admit of 4 Gaussian resonances. An example of the deconvolution process, performed for the 20 mA data, is shown in Fig. 8.8.

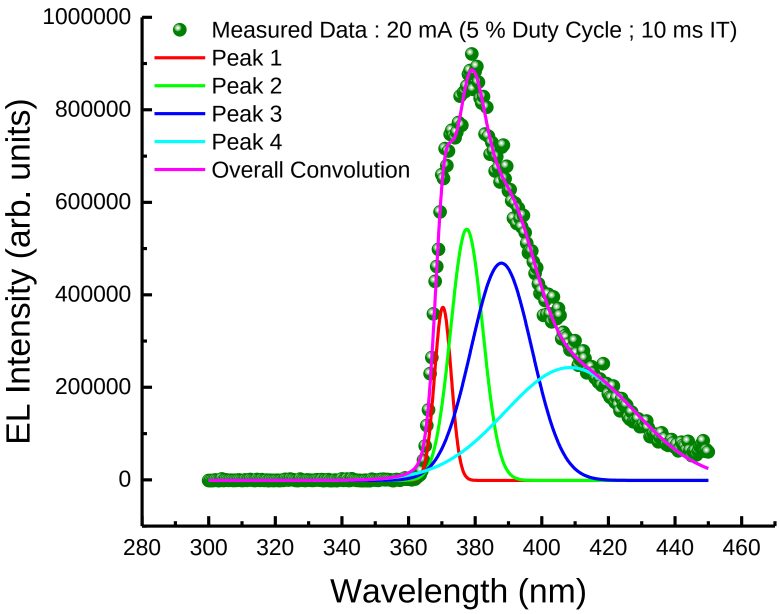

Figure 8.8. Analysis of the 20 mA electroluminescence spectrum as a convolution of constituent Gaussian resonances.

The linewidths and the central emission wavelengths of the four individual peaks have been studied as a function of injection. The excitation-dependence of the emission linewidths and the peak emission wavelengths is shown in Fig. 8.9 and Fig. 8.10, respectively. There is no observation of linewidth narrowing at any injection. None of the peaks shows any appreciable change in the central emission wavelengths as a function of excitation. This behavior, particularly in the context of Peaks 2 and 3, is consistent with our assumption that the main radiative transitions, which generate the emission lines 2 and 3, probably originate from a donor-to-acceptor pair (DAP) radiative transition. Thus, our detailed studies show that there is almost no change in the nature of the output spectral characteristics even though a threshold-like

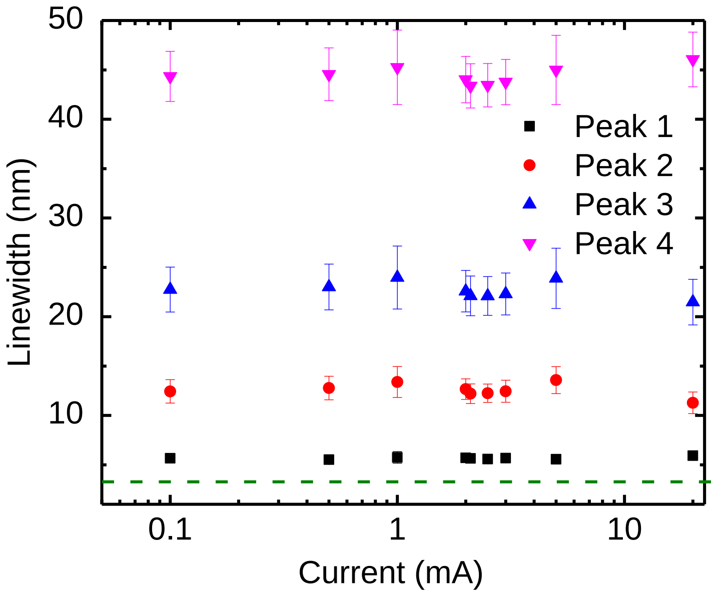

Figure 8.9. Injection-dependence of the emission linewidths of the four peaks identified in Fig. 8.8.

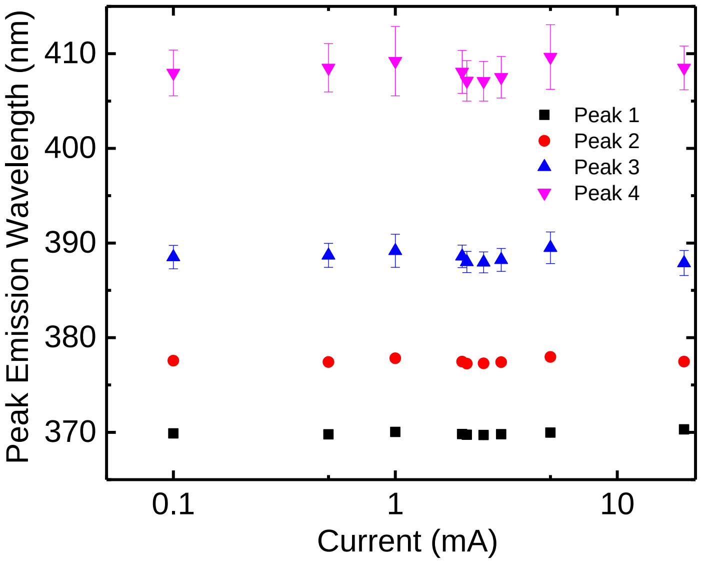

Figure 8.10. Injection-dependence of the peak emission wavelengths of the four peaks identified in Fig. 8.8.

transition is observed. However, it must be emphasized that the non-linear enhancement effect is still present at the injection of ~ 2 mA. This can be seen from the injection dependence of the integrated electroluminescence intensities of the peaks as shown in Fig. 8.11. In Fig. 8.11, only the four injections wherein the duty cycle is the same are studied, as the total light output depends on the excitation conditions, unlike spectral characteristics such as linewidths and peak emission wavelengths which should not vary appreciably with changes in duty cycles or integration times. It can be observed from Fig. 8.11 that all the four peaks increase non-linearly with increasing

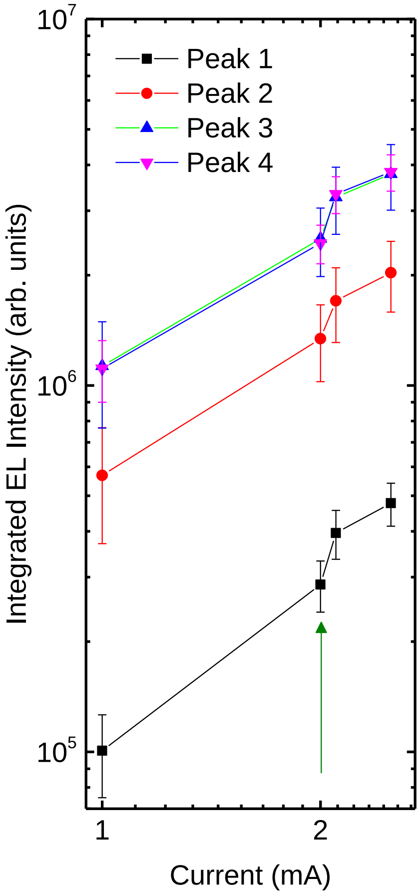

Figure 8.11. Injection-dependence of the integrated electroluminescence intensities of the four peaks identified in Fig. 8.8. The vertical arrow indicates the onset of nonlinearity.

excitation. This shows that the strong enhancement observed in the output characteristics with increasing injection is not a particular characteristic of one of the identified transitions. Instead, it suggests that at 2 mA, there is a sudden increase in the electron injection efficiency due to some tunneling mechanism as a result of which suddenly the total light output increases. This section concludes with a few remarks on similar electroluminescence spectra recorded with higher spectral acquisition. Figure 8.12 shows the lineshape of the spectral output, recorded at ~ 0.1 mA as an illustrative example, remains essentially identical to that shown in Fig. 8.7, where higher spectral resolutions have been achieved in the measurements by reducing the entrance and exit slit widths. Figure 8.12 also shows that by performing a multi-peak Gaussian analysis on the spectra, essentially identical results are obtained. From the analysis of Fig. 8.12, it is seen that peaks 2 and 3 are centered at ~ 379.5 ± 0.4 nm and ~ 390.5 ± 4 nm. These are reasonably close to the values observed in Fig. 8.7. Further as evidenced from the linewidth data of Fig. 8.9, since the resonances are so highly in-homogeneously broadened, a reduction in the resolution from ~ 3.16 nm to ~ 0.2 nm should not introduce any appreciable errors in the analyses. It is also seen that there are no narrow hidden resonances which might not have been detected in the ~ 3 nm resolution data. Thus, it is reasonable to stick to the results summarized in Figs. 8.9, 8.10 and 8.11, with regards to the nature of the spectral output.

Finally, the output spectral characteristics measured under conditions of rather high excitations are studied. It may be remembered that such a strong non-linearity was observed in the output of devices, which have highly reflective DBR mirrors. The peak wavelength of the reflectance data is at ~ 367 ± 3 nm. Nevertheless, the reflectance is also sufficiently strong at ~ 380 nm as well. However, conventional photon lasing characteristics have not been observed in these devices even under very high excitation conditions. This is probably because of the large

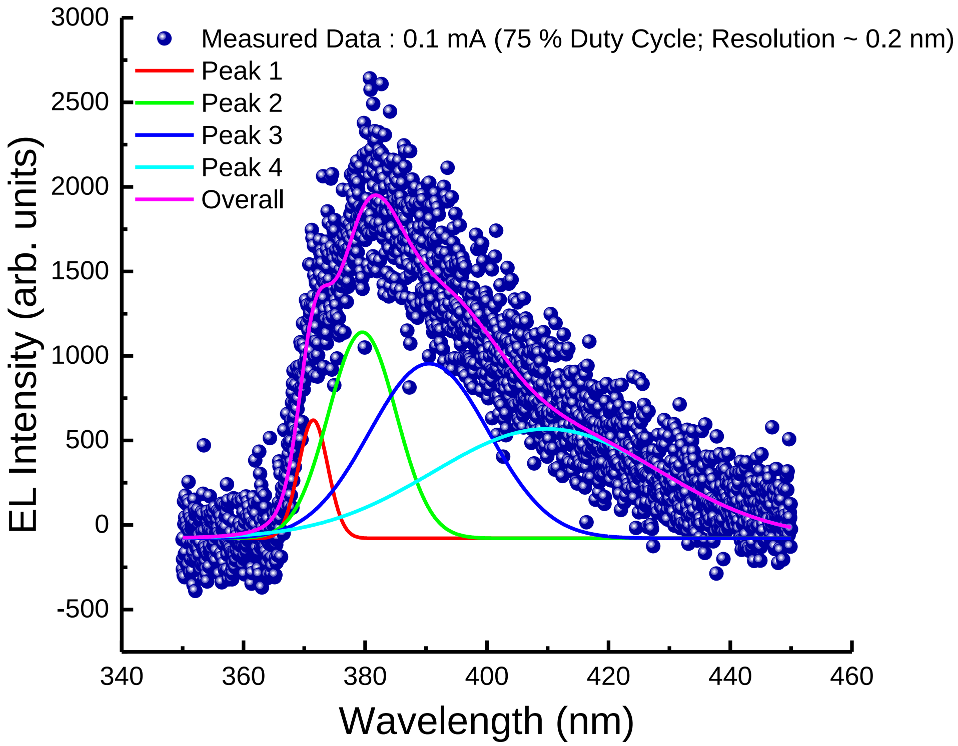

Figure 8.12 Multi-peak Gaussian analysis of the ~ 0.1 mA EL data, showing there are four constituent Gaussian resonances in agreement with the analysis shown in Fig. 7.8.

losses in the cavity because of defects and degradation, as well as the rather broad starting linewidth of the spontaneous emission spectrum. The device emission remains incoherent throughout at all values of excitation. Although some narrow spectral features do appear under high excitation conditions (~ 50 kA/cm^2), as shown in Fig. 8.13, there is no clear trend of linewidth narrowing or spectral collapse. Figure 8.14 shows the results of the analysis. Analysis of the data yields a power-law dependence of the form: L ~ I$^{0.67}$ without any threshold-like transitions. Measurements have been made up to an injection of ~ 75 kA/cm^2, beyond which the contacts of the device suffer irreversible damage.

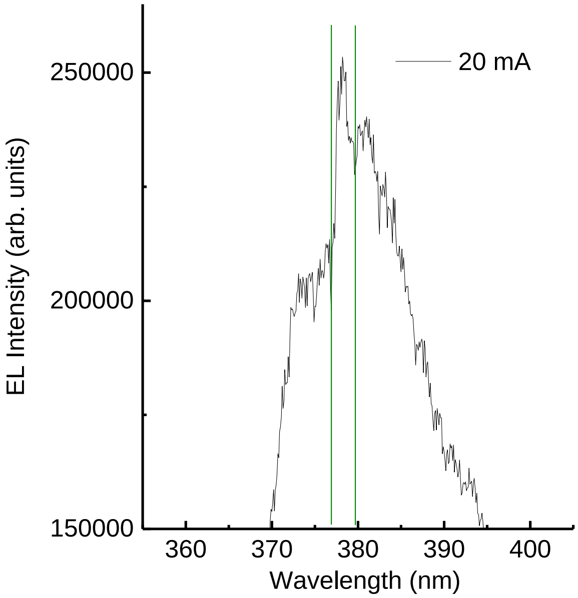

Figure 8.13. Spectral output at ~ 20 mA injection.

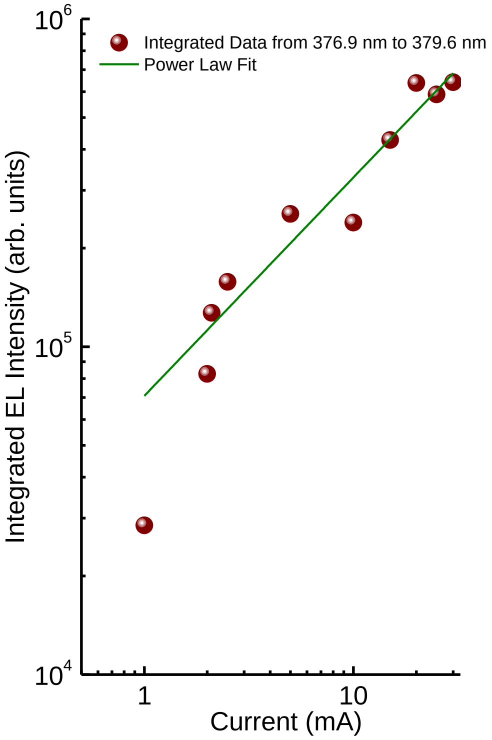

Figure 8.14. Plot of the integrated electroluminescence intensities as a function of the excitation. The solid line shows a power-law fit.

8.2.1.6 Summary

This chapter has furnished experimental evidence for super-linear output characteristics in micron-scale GaN-based electroluminescent devices having n-type ferromagnetic tunnel contacts, in between the strong coupling and weak coupling regimes of operation. In this context, weak coupling regime of operation implies transparency in the cavity. Theoretical investigations of the measured data are presently underway and are beyond the scope of the present dissertation. The non-linear effect probably originates from the sudden activation of some resonant tunneling pathway over a particular excitation regime. The resonant tunneling takes place, in all probability, through the MgO tunnel barrier. The latter generally acts as a spin-dependent tunnel barrier at low excitation conditions and probably as a spin-independent resonant tunneling pathway over a certain excitation window. This tunneling phenomenon is probably spin-independent, as supported by the absence of any trends in our circular polarization data. The tunneling can also probably take place through the heterojunction band-offset. Thus an analysis of the energy band-diagrams under high biasing conditions (~ 40 V and larger) is presently underway. It is highly probable that field-assisted tunneling takes place under high excitation conditions through conduction band offset between the $In_{0.18}Al_{0.82}N$ layer and the GaN active region.

The degradation of the device characteristics, the red-shift of the main emission band from ~ 365 nm to ~ 380 nm, and the relative wavelength invariance of the ~ 380 nm band with injection all support our hypothesis that there has been some migration of Mg atoms with time and heating and high excitation, from the underlying p-type layers to the GaN active region. Donor-acceptor pair (DAP-type) emission, which does not shift with excitation, has been reported in n-type GaN samples lightly p-type doped with Mg atoms. Another intriguing explanation might be the sudden activation of a phonon-assisted tunneling mechanism directly into these donor states. Although at the time of composition, this dissertation cannot provide a resolution of these varying competing ideas, nevertheless this chapter has argued in sufficient length and detail, the reality and repeatability of the measured data. The nonlinearity is observed in the same device under multiple measurement conditions, and in multiple devices, and any artifacts originating from the measurement or the instruments employed, have been ruled out.

8.2.2 Applications and Future Prospects for Electrically Energized GaN-Based Excitonic-Polaritonic Devices

Exciton-photon strong coupling effects in general, and polariton lasing effects, have been extensively investigated in high quality GaAs and CdTe-based microcavities. However, these phenomena, especially those pertaining to parametric amplification and non-linear coherent emission, are destroyed by thermal broadening and various decohering effects for temperatures above 220 K. Thus, it is essential that these cavity electrodynamic phenomena have to be investigated in materials, wherein coherent polariton luminescence can be obtained at temperatures at and well above room temperature. Coherent polariton emission at room temperature was first observed from bulk GaN microcavities. The realization of strongly coupled III-nitride-based microcavities has been an important motivation for the photonics and polaritonics communities over the last three decades. GaN is more advantageous as compared to GaAs and CdTe-based materials for strong coupling studies, because of its larger effective electron mass, which translates to reduced values for the free excitonic mass as well as the effective spatial extent of the excitonic wavefunctions (the Bohr radius). This leads to larger oscillator strengths as well as large exciton-binding energies in these materials. In particular, excitonic phenomena in GaN are observable at room temperature and these free excitons are also stable. Thus, the present dissertation has exclusively focused on polaritonic devices processed from III-nitride-based materials. Real world implementation of polaritonic devices require electrically energized devices operating at room temperature. The output characteristics of the devices should be relatively stable, and further the devices should also have significant lifetimes. Practical applications of polariton lasers would be in systems which require a low-energy, low-power and highly coherent light sources such as biomedical applications. Further, the coherent output of polariton lasers operated with conventional unpolarized electrical excitation is linearly polarized. A stable linearly polarized coherent ultraviolet (UV) or deep UV light source is required for biochemical analysis, photo-alignment of nematic liquid crystals, eye surgery, and other industrial applications [52-56]. Although the optical output power levels in these lasers are rather modest as discussed in Section 8.2.1, a single source or an array, to get higher powers, would be adequate for such applications.

The present dissertation also discussed the design, implementation and output characteristics of a room temperature spin-polarized polariton laser diode. The device represents a bias-tunable low energy coherent circularly-polarized light source operating at room temperature. Such a polariton diode laser where spin-polarized electrons are injected by a ferromagnetic tunnel injection contact acts as a device with controllable output circular polarization. Thus, it is useful for the study of fibrous proteins, collagens, and asymmetric photochemical reactions that are sensitive to circularly polarized light. Information can be encoded onto both the intensity as well as the polarization of light in an optical communication system, thus effectively doubling the bandwidth of communication channels [114]. A spin polariton diode laser combines the advantages of a conventional spin photon laser and a polariton laser. Further, the operation of spin photon lasers has remained limited to a temperature of 230 K. Also, previously demonstrated spin photon lasers were designed in the form of vertical cavity surface-emitting lasers (VCSELs) and consequently required large magnetic fields in the Faraday geometry for operation. This was because the magnetic contacts had to be magnetized along their hard axes of magnetization (coincident with the direction of optical emission in the Faraday geometry). In contrast, the present devices have an edge-emitting geometry and thus they have to be only magnetized along one of the easy axes, which lie in the plane of the ferromagnet (coincident with the direction of optical emission in the quasi-Voigt geometry). The in-plane magnetization of CoFe (the ferromagnetic component of the ferromagnetic tunnel contact) enables the use of an edge-emitting geometry, which utilizes the important advantages of ferromagnetic metals such as small coercive fields and high remanent magnetization [114]. These are the characteristics that allow nonvolatile spin manipulation using modest magnetic fields and is thus a very practical consideration for device applications. This also allows for the operation of these devices in the absence of any ambient magnetic field, once the spin injectors have been magnetized.

Future work on these III-nitride-based polariton laser diodes may include improvised device heterostructure designs, which would include replacing bulk GaN with multiple quantum wells (QW) in the device active region. Introduction of QWs as the emitters, generally improves the strong-coupling characteristics in the microcavities, mainly because of the increased free exciton-binding energy and enhanced overlap of the excitonic wavefunction with the intra-cavity optical standing wave. All of these lead to larger values for the Rabi splitting. The latter can be easily accomplished by placing the QWs at the antinodes of the cavity field. Another very important step would be the design and implementation of better microcavities having higher Q-factors which would lead to longer polariton lifetimes. These long lifetimes would help in reducing the polariton laser threshold current densities, increase the degree of non-linearity in the output characteristics and also enable the observation of polariton lasing over a longer excitation regime. The longer lifetimes should also enable the observation of polariton condensates which are better equilibrated with the lattice. Such high-Q strongly coupled microcavities should lead to very low-threshold coherent emitters in the UV spectral range, as well as serve as platforms for studies of new exotic phenomena, such as deep and ultra-strong coupling in these material systems.

8.2.3 Room Temperature Electrically Injected Edge-Emitting Spin Laser

A room temperature spin photon laser would combine the advantages of the spin polariton laser discussed in the present dissertation; besides have larger output optical power levels, stability and longer lifetimes. The maximum operating temperature of electrically injected spin-polarized lasers has remained limited to 230 K [33]. Further, edge-emitting spin laser diodes have not yet been demonstrated. The single most important advantage of edge-emitting laser diodes over their surface-emitting counterparts is that they can be operated at remanence, in the absence of any ambient magnetic field.

The essentially requirements for the successful operation of spin lasers include a laser diode having a wide active region (preferably, double heterostructure configurations or multiple quantum-well-based active region wherein the well widths are rather large, almost approaching the unconfined regime) and a low value of the threshold current. To obtain a low threshold, double heterostructure devices should be processed into long cavity length samples. For GaN-based devices, the heterostructure should be grown on high quality free-standing GaN substrates and the p-type doping of the various layers should be highly optimized. The intrinsic region should have low cavity losses and low free carrier absorption losses. Thus, the device heterostructure presented in Chapter V, reproduced below in Fig. 8.15, should be sufficient, assuming that the following considerations are kept in mind:

1. The heterostructure is preferably grown on high quality free-standing GaN substrates to accomplish better diode characteristics and lower cavity losses.
2. The p-type layers are highly optimized to ensure the series resistance is rather low and thus the threshold is achieved at a reasonably small value of diode voltage. Higher diode voltages, which lead to higher tunnel junction biases, lead to a reduction in the injected electron spin polarization. There is also more electron scattering at higher injections, which lead to more dephasing.
3. The device is processed into long cavity length devices.

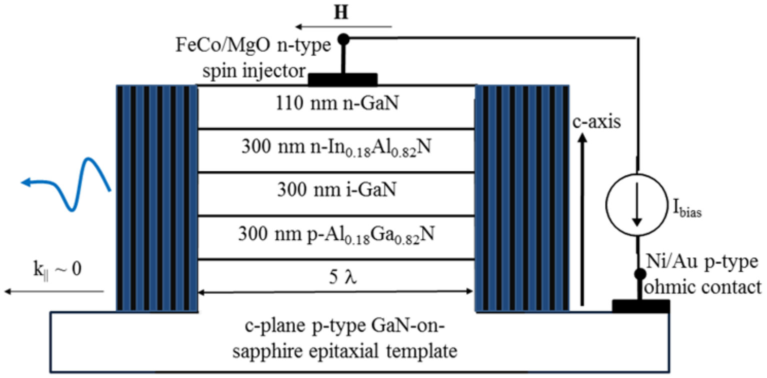

Figure 8.15. Suitable double heterostructure for successful implementation of a room temperature edge-emitting spin laser diode.

BIBLIOGRAPHY

BIBLIOGRAPHY

[1] B. Ellis, M. A. Mayer, G. Shambat, T. Sarmiento, J. Harris, E. E. Haller, and Jelena Vučković, Nat. Photon. **5**, 297 (2011).

[2] H. Deng, H. Haug, and Y. Yamamoto, Rev. Mod. Phys **82**, 1489 (2010).

[3] C. Weisbuch, M. Nishioka, A. Ishikawa, and Y. Arakawa, Phys. Rev. Lett. **69**, 3314 (1992)

[4] H. Deng, G. Weihs, C. Santori, J. Bloch, and Y. Yamamoto, Science **298**, 199 (2002).

[5] H. Deng, G. Weihs, D. Snoke, J. Bloch, and Y. Yamamoto, Proc. Natl. Acad. Sci. U. S. A. **100**, 15318 (2003).

[6] G. Malpuech, Y. G. Rubo, F. P. Laussy, P. Bigenwald, and A. V. Kavokin, Semicond. Sci. Technol. 18, S395 (2003).

[7] J. Kasprzak, D. D. Solnyshkov, R. Andre´, L. S. Dang, and G. Malpuech, Phys. Rev. Lett. 101, 146404 (2008).

[8] A. Imamoḡlu and R. J. Ram, Phys. Lett. A **214**, 193 (1996)

[9] A. Imamoglu, R. J. Ram, S. Pau, and Y. Yamamoto, Phys. Rev. A **53**, 4250 (1996).

[10] Le Si Dang, D. Heger, R. André, F. Bœuf, and R. Romestain, Phys. Rev. Lett. **81**, 3920 (1998).

[11] R. M. Stevenson et al., Phys. Rev. Lett. **85**, 3680 (2000).

[12] D. Bajoni, P. Senellart, E. Wertz, I. Sagnes, A. Miard, A. Lemaitre, and J. Bloch, Phys. Rev. Lett. **100**, 047401 (2008).

[13] S. Christopoulos, G. B. H. von Hogersthal, A. J. D. Grundy, P. G. Lagoudakis, A. V. Kavokin, J. J. Baumberg, G. Christmann, R. Butte, E. Feltin, J.-F. Carlin, and N. Grandjean, Phys. Rev. Lett. **98**, 126405 (2007).

[14] P. Bhattacharya, B. Xiao, A. Das, S. Bhowmick, and J. Heo, Phys. Rev. Lett. **110**, 206403 (2013).

[15] C. Schneider et al., Nature (London) **497**, 348 (2013).

[16] P. Bhattacharya, T. Frost, S. Deshpande, M. Z. Baten, A. Hazari, and A. Das, Phys. Rev. Lett. **112**, 236802 (2014).

[17] A. Bhattacharya, M. Z. Baten, I. Iorsh, T. Frost, A. Kavokin, and P. Bhattacharya, Phys. Rev. B **94**, 035203 (2016).

[18] J. Levrat, R. Butté, T. Christian, M. Glauser, E. Feltin, J.-F. Carlin, N. Grandjean, D. Read, A. V. Kavokin, and Y. G. Rubo, Phys. Rev. Lett. **104**, 166402 (2010).

[19] M. Holub, J. Shin, D. Saha, and P. Bhattacharya, Phys. Rev. Lett. **98**, 146603 (2007).

[20] A. Bhattacharya, M. Z. Baten, T. Frost, and P. Bhattacharya, IEEE Photonics Technol. Lett. **29**, 338 (2017).

[21] T. Frost, A. Banerjee, K. Sun, S. L. Chuang, and P. Bhattacharya, IEEE J. Quantum Electron. **49** (11), 923 (2013).

[22] S. Nakamura, Rev. Mod. Phys. **87**, 1139 (2015).

[23] J. H. Bub, J. Rudolph, F. Natali, and F. S. D. Hagele, Appl. Phys. Lett. **95**, 192107 (2009).

[24] A. Banerjee, F. Doğan, J. Heo, A. Manchon, W. Guo, and P. Bhattacharya, Nano Lett. **11**, 5396 (2011).

[25] B. Beschoten, E. Johnston-Halperin, D. K. Young, M. Poggio, J. E. Grimaldi, S. Keller, S. P. DenBaars, U. K. Mishra, E. L. Hu, and D. D. Awschalom, Phys. Rev. B **63**, 121202(R) (2001).

[26] J. H. Bub, J. Rudolph, F. Natali, F. Semond, and D. Hagele, Phys. Rev. B **81**, 155216 (2010).

[27] H. Kum, J. Heo, S. Jahangir, A. Banerjee, W. Guo, and P. Bhattacharya, Appl. Phys. Lett. **100**, 182407 (2012).

[28] X. Jiang, R. Wang, R. M. Shelby, R. M. Macfarlane, S. R. Bank, J. S. Harris, and S. S. P. Parkin, Phys. Rev. Lett. **94**, 056601 (2005).

[29] H. Ando, T. Sogawa, and H. Gotoh, Appl. Phys. Lett. **73**, 566 (1998).

[30] F. Meier and B. P. Zakharchenya, Editors, Optical Orientation (Elsevier Science, Amsterdam, 1984).

[31] J. Rudolph et al., Appl. Phys. Lett. **82**, 4516 (2003).

[32] J. Rudolph et al., Appl. Phys. Lett. **87**, 241117 (2005).

[33] D. Saha, D. Basu, and P. Bhattacharya, Phys. Rev. B **82**, 205309 (2010).

[34] M. H. Szymańska, J. Keeling, and P. B. Littlewood, Phys. Rev. Lett. **96**, 230602 (2006).

[35] L. V. Butov, A. L. Ivanov, A. Imamoglu, P. B. Littlewood, A. A. Shashkin, V. T. Dolgopolov, K. L. Campman, and A. C. Gossard, Phys. Rev. Lett. **86**, 5608 (2001).

[36] D. Solnyshkov, E. Petrolati, A. Di Carlo, and G. Malpuech, Appl. Phys. Lett. **94**, 011110 (2009).

[37] J. Kasprzak, M. Richard, S. Kundermann, A. Baas, P. Jeambrun, J. M. J. Keeling, F. M. Marchetti, M. H. Szyman´ska, R. Andre´, J. L. Staehli, V. Savona, P. B. Littlewood, B. Deveaud, and Le Si Dang, Nature **443**, 409 (2006).

[38] R. Balili, V. Hartwell, D. Snoke, L. Pfeiffer, and K. West, Science **316**, 1007 (2007).

[39] D. Sanvitto and S. Kéna-Cohen, Nat. Mater. **15**, 1061 (2016).

[40] A. Das, J. Heo, M. Jankowski, W. Guo, L. Zhang, H. Deng, and P. Bhattacharya, Phys. Rev. Lett. **107**, 066405 (2011).

[41] A. P. D. Love, D. N. Krizhanovskii, D. M. Whittaker, R. Bouchekioua, D. Sanvitto, S. Al Rizeiqi, R. Bradley, M. S. Skolnick, P. R. Eastham, R. André, and Le Si Dang, Phys. Rev. Lett. **101**, 067404 (2008).

[42] Y. G. Rubo, Phys. Rev. Lett. **99**, 106401 (2007).

[43] A. Kavokin, G. Malpuech, and M. Glazov, Phys. Rev. Lett. **95**, 136601 (2005).

[44] E. S. Sedov and A. V. Kavokin, Scientific Reports **7**, 9797 (2017).

[45] I. A. Shelykh, Y. G. Rubo, G. Malpuech, D. D. Solnyshkov, and A. Kavokin, Phys. Rev. Lett. **97**, 066402 (2006).

[46] H. Ohadi, A. Dreismann, Y. G. Rubo, F. Pinsker, Y. del Valle-Inclan Redondo, S. I. Tsintzos, Z. Hatzopoulos, P. G. Savvidis, and J. J. Baumberg, Phys. Rev. X **5**, 031002 (2015).

[47] J. J. Baumberg, A. V. Kavokin, S. Christopoulos, A. J. D. Grundy, R. Butté, G. Christmann, D. D. Solnyshkov, G. Malpuech, G. Baldassarri Höger von Högersthal, E. Feltin, J.-F. Carlin, and N. Grandjean, Phys. Rev. Lett. **101**, 136409 (2008).

[48] Yu. G. Rubo, Phys. Status Solidi A **201**, 641 (2004).

[49] H. Ohadi, E. Kammann, T. C. H. Liew, K. G. Lagoudakis, A. V. Kavokin, and P. G. Lagoudakis, Phys. Rev. Lett. **109**, 016404 (2012).

[50] K. G. Lagoudakis, M. Wouters, M. Richard, A. Baas, I. Carusotto, R. André, Le Si Dang, and B. Deveaud-Plédran, Nat. Physics **4**, 706 (2008).

[51] I. Iorsh, M. Glauser, G. Rossbach, J. Levrat, M. Cobet, R. Butte, N. Grandjean, M. A. Kaliteevski, R. A. Abram, and A. V. Kavokin, Phys. Rev. B **86**, 125308 (2012).

[52] Q. Ren, R. P. Gailitis, K. P. Thomson, and J. T. Lin, IEEE J. Quant. Electron. **26**, 2284 (1990).

[53] M. Schadt, K. Schmitt, V. Kozinkov, and V. Chigrinov, Jpn. J. Appl. Phys. **31**, 2155 (1992).

[54] M. Hasegawa and Y. Taira, J. Photopolym. Sci. Technol. **8**, 241 (1995).

[55] N. Kawatsuki, H. Ono, H. Takatsuka, T. Yamamoto, and O. Sangen, Macromolecules **30**, 6680 (1997).

[56] B. W. Chwirot, S. Chwirot, W. Jedrzejczyk, M. Jackowski, A. M. Raczyńska, J. Winczakiewicz, and J. Dobber, Lasers Surg. Med. **21**, 149 (1997).

[57] Ł. Kłopotowski, M. D. Martin, A. Amo, L. Vina, I. A. Shelykh, ˜ M. M. Glazov, G. Malpuech, A. V. Kavokin, and R. Andre, Solid State Commun. **139**, 511 (2006).

[58] D. Read, T. C. H. Liew, Yuri G. Rubo, and A. V. Kavokin, Phys. Rev. B **80**, 195309 (2009).

[59] K. G. Lagoudakis, T. Ostatnický, A. V. Kavokin, Y. G. Rubo, R. André, and B. Deveaud-Plédran, Science **326**, 974 (2009).

[60] D. Ballarini, A. Amo, L. Viña, D. Sanvitto, M. S. Skolnick, and J. S. Roberts, Appl. Phys. Lett. **90**, 201905 (2007).

[61] D. Ballarini, A. Amo, D. Sanvitto, L. Viña, M. S. Skolnick, and J. S. Roberts, Physica E **40**, 2049 (2008).

[62] X. Lou, C. Adelmann, S. A. Crooker, E. S. Garlid, J. Zhang, K. S. M. Reddy, S. D. Flexner, C. J. Palmstrom, and P. A. Crowell, Nat. Phys. **3**, 197–202 (2007).

[63] L. Qing, J. Li, I. Appelbaum, and H. Dery, Phys. Rev. B **91**, 241405(R) (2015).

[64] R. Fiederling et al., "Injection and detection of a spin-polarized current in a light-emitting diode", Nature, vol. **402**, pp. 787-790, Dec. 1999.

[65] Y. Ohno, D. K. Young, B. Beschoten, F. Matsukura, H. Ohno, D. D. Awschalom, "Electrical spin injection in a ferromagnetic semiconductor heterostructure", Nature, vol. **402**, pp. 790-792, Dec. 1999.

[66] B. T. Jonker, Y. D. Park, B. R. Bennett, H. D. Cheong, G. Kioseoglou, A. Petrou, "Robust electrical spin injection into a semiconductor heterostructure", Phys. Rev. B, vol. **62**, no. 12, pp. 8180-8183, Sep. 2000.

[67] H. J. Zhu, M. Ramsteiner, H. Kostial, M. Wassermeier, H.-P. Schönherr, K. H. Ploog, "Room-temperature spin injection from fe into GaAs", Phys. Rev. Lett., vol. **87**, no. 1, pp. 016601-1-016601-4, Jul. 2001.

[68] S. Ghosh, P. Bhattacharya, "Surface-emitting spin-polarized In0.4Ga0.6As/GaAs quantum-dot light-emitting diode", Appl. Phys. Lett., vol. **80**, no. 4, pp. 658-660, Jan. 2002.

[69] X. Jiang et al., "Highly spin-polarized room-temperature tunnel injector for semiconductor spintronics using MgO (100)", Phys. Rev. Lett., vol. **94**, no. 5, pp. 056601-1-056601-4, Feb. 2005.

[70] O. M. J. van’t Erve, G. Kioseoglou, A. T. Hanbicki, C. H. Li, B. T. Jonker, "Remanent electrical spin injection from Fe into AlGaAs/GaAs light emitting diodes", Appl. Phys. Lett., vol. **89**, no. 7, pp. 072505-1-072505-2, Aug. 2006.

[71] B. S. Tao et al., "Electrical spin injection into GaAs based light emitting diodes using perpendicular magnetic tunnel junction-type spin injector", Appl. Phys. Lett., vol. **108**, no. 15, pp. 152404-1-152404-5, Apr. 2016.

[72] I. A. Buyanova et al., "Spin injection and spin loss in GaMnN/InGaN light-emitting diodes", Proc. AIP Conf., vol. **772**, pp. 1399-1400, Jun. 2005.

[73] M.-H. Ham, S. Yoon, Y. Park, L. Bian, M. Ramsteiner, J. Myoung, "Electrical spin injection from room-temperature ferromagnetic (Ga Mn)N in nitride-based spin-polarized light-emitting diodes", J. Phys. Condens. Matter, vol. **18**, no. 32, pp. 7703-7708, Jul. 2006.

[74] D. Banerjee et al., "Electrical spin injection using GaCrN in a GaN based spin light emitting diode", Appl. Phys. Lett., vol. **103**, no. 24, pp. 242408-1-242408-4, Dec. 2013.

[75] J. Y. Chen et al., "Efficient spin-light emitting diodes based on InGaN/GaN quantum disks at room temperature: A new self-polarized paradigm", Nano Lett., vol. **14**, no. 6, pp. 3130-3137, May 2014.

[76] M. Hashimoto, Y. K. Zhou, M. Kanamura, H. Katayama-Yoshida, H. Asahi, "MBE growth and properties of GaCrN", J. Cryst. Growth, vol. **251**, no. 1, pp. 327-330, Apr. 2003.

[77] P. Suggisetti et al., "Room temperature ferromagnetism in thermally diffused Cr in GaN", AIP Adv., vol. **3**, no. 3, pp. 032143-1-032143-6, Mar. 2013.

[78] B. Gil, P. Bigenwald, P. P. Paskov, B. Monemar, "Internal structure of acceptor-bound excitons in wide-band-gap wurtzite semiconductors", Phys. Rev. B Condens. Matter, vol. **81**, no. 8, pp. 085211-1-085211-14, Feb. 2010.

[79] B. Gil, F. Hamdani, H. Morkoç, "Oscillator strengths for optical band-to-band processes in GaN epilayers", Phys. Rev. B Condens. Matter, vol. **54**, no. 11, pp. 7678-7681, Sep. 1996.

[80] P. Van Dorpe et al., "Very high spin polarization in GaAs by injection from a (Ga Mn) As Zener diode", Appl. Phys. Lett., vol. **84**, no. 18, pp. 3495-3497, May 2004.

[81] H. Sanada et al., Appl. Phys. Lett. **81**, 2788 (2002).

[82] E. A. Barry, A. A. Kiselev, and K. W. Kim, Appl. Phys. Lett. **82**, 3686 (2003).

[83] J. H. Park, G. Lin, D. Y. Kim, J. W. Lee, J. Cho, J. Kim, J. Lee, Y. Kim, Y. Park, E. F. Schubert, and J. K. Kim, Opt. Express **23**, 15398 (2015).

[84] J. Kim, Y. Leem, J. Kang, J. Kwon, B. Cho, S. Yim, J. H. Baek, and S. Park, ACS Photonics **2**, 1519 (2015).

[85] F. P. Laussy, I. A. Shelykh, G. Malpuech, and A. Kavokin, Phys. Rev. B **73**, 035315 (2006).

[86] G. Malpuech, M. M. Glazov, I. A. Shelykh, P. Bigenwald, and K. V. Kavokin, Appl. Phys. Lett. **88**, 111118 (2006).

[87] M. D. Martín, G. Aichmayr, L. Viña, and R. André, Phys. Rev. Lett. 89, 077402 (2002).

[88] I. A. Shelykh, K. V. Kavokin, A. V. Kavokin, G. Malpuech, P. Bigenwald, H. Deng, G. Weihs, and Y. Yamamoto, Phys. Rev. B 70, 035320 (2004).

[89] K. V. Kavokin, I. A. Shelykh, A. V. Kavokin, G. Malpuech, and P. Bigenwald, Phys. Rev. Lett. 92, 017401 (2004).

[90] G. Panzarini, L. C. Andreani, A. Armitage, D. Baxter, M. S. Skolnick, V. N. Astratov, J. S. Roberts, A. V. Kavokin, M. R. Vladimirova, and M. A. Kaliteevski, Phys. Rev. B **59**, 5082 (1999).

[91] J. Levrat, R. Butté, E. Feltin, J. F. Carlin, N. Grandjean, D. Solnyshkov, and G. Malpuech, Phys. Rev. B **81**, 125305 (2010).

[92] A. Bhattacharya, M. Z. Baten, and P. Bhattacharya, Appl. Phys. Lett. **108**, 042406 (2016).

[93] T. Kuroda, T. Yabushita, T. Kosuge, A. Tackeuchi, K. Taniguchi, T. Chinone, and N. Horio, Appl. Phys. Lett. **85**, 3116 (2004).

[94] D. Basu, D. Saha, C. C. Wu, M. Holub, Z. Mi, and P. Bhattacharya, Appl. Phys. Lett. **92**, 091119 (2008).

[95] D. Basu, D. Saha, and P. Bhattacharya, Phys. Rev. Lett. **102**, 093904 (2009).

[96] P. G. Savvidis, J. J. Baumberg, R. M. Stevenson, M. S. Skolnick, D. M. Whittaker, and J. S. Roberts, Phys. Rev. Lett. **84**, 1547 (2000).

[97] C. Sturm, D. Solnyshkov, O. Krebs, A. Lemaître, I. Sagnes, E. Galopin, A. Amo, G. Malpuech, and J. Bloch, Phys. Rev. B **91**, 155130 (2015).

[98] J.-G. Rousset, B. Piętka, M. Król, R. Mirek, K. Lekenta, J. Szczytko, W. Pacuski, and M. Nawrocki, Phys. Rev. B **96**, 125403 (2017).

[99] M. Saba, C. Ciuti, J. Bloch, V. Thierry-Mieg, R. André, Le Si Dang, S. Kundermann, A. Mura, G. Bongiovanni, J. L. Staehli, and B. Deveaud, Nature **414**, 731 (2001).

[100] T. A. Fisher, A. M. Afshar, M. S. Skolnick, D. M. Whittaker, J. S. Roberts, G. Hill, M. A. Pate, Solid State Electron. **40**, 493 (1996).

[101] D. Bajoni, E. Semenova, A. Lemaître, S. Bouchoule, E. Wertz, P. Senellart, and J. Bloch, Phys. Rev. B **77**, 113303 (2008).

[102] D. Bajoni, E. Semenova, A. Lemaître, S. Bouchoule, E. Wertz, P. Senellart, S. Barbay, R. Kuszelewicz, and J. Bloch, Phys. Rev. Lett. **101**, 266402 (2008).

[103] C. Coulson, G. Christmann, P. Cristofolini, C. Grossmann, J. J. Baumberg, S. I. Tsintzos, G. Konstantinidis, Z. Hatzopoulos, and P. G. Savvidis, Phys. Rev. B **87**, 045311 (2013).

[104] P. Bhattacharya, A. Das, S. Bhowmick, M. Jankowski, and C. Lee, Appl. Phys. Lett. **100**, 171106 (2012).

[105] K. Winkler, P. Gold, B. Bradel, S. Reitzenstein, V. D. Kulakovskii, M. Kamp, C. Schneider, and S. Höfling, Phys. Rev. B **91**, 045127 (2015).

[106] S. Brodbeck, H. Suchomel, M. Amthor, T. Steinl, M. Kamp, C. Schneider, and S. Höfling Phys. Rev. Lett. **117**, 127401 (2016).

[107] H. Suchomel, S. Brodbeck, T. C. H. Liew, M. Amthor, M. Klaas, S. Klembt, M. Kamp, S. Höfling, and C. Schneider, Sci. Rep. **7**, 5114 (2017).

[108] F. Tassone and Y. Yamamoto, Phys. Rev. B **59**, 10830 (1999).

[109] R. M. Stevenson, V. N. Astratov, M. S. Skolnick, D. M. Whittaker, M. Emam-Ismail, A. I. Tartakovskii, P. G. Savvidis, J. J. Baumberg, and J. S. Roberts, Phys. Rev. Lett. **85**, 3680 (2000).

[110] R. Huang, F. Tassone, and Y. Yamamoto, Phys. Rev. B **61**, R7854(R) (2000).

[111] F. Boeuf, R. André, R. Romestain, Le Si Dang, E. Péronne, J. F. Lampin, D. Hulin, and A. Alexandrou, Phys. Rev. B **62**, R2279(R) (2000).

[112] W. Fang and S. L. Chuang, Appl. Phys. Lett. **67**, 751 (1995).

[113] F. Binet, J. Y. Duboz, J. Off, and F. Scholz, Phys. Rev. B **60**, 4715 (1999).

[114] A. Bhattacharya, M. Z. Baten, I. Iorsh, T. Frost, A. Kavokin, and P. Bhattacharya, Phys. Rev. Lett. **119**, 067701 (2017).